Exploring optically tunable metasurfaces with a time-resolved terahertz spectroscopy technique

Ahmed Jaber

Thesis submitted in partial fulfillment

of the requirements for the degree of

Master of Science

in Physics

Department of Physics

Faculty of Science

University of Ottawa

Abstract

This thesis will explore the ultrafast modulation and optical tunability of plasmonic filters in the terahertz (THz) spectral region. First, the principles and functional design of THz metasurfaces are explored through plasmonic surface lattice resonance interactions and lumped-element circuit models. We will then describe the methodology of generating and detecting THz radiation through the nonlinear processes of optical rectification and electro-optic sampling, respectively. Next, the implementation of a THz time-domain spectroscopy technique is discussed in the context of pump-probe measurements and time-domain resonance analysis. We then show how THz probed materials can be characterized in terms of a temporal and spectral analysis. We will demonstrate how this time-domain technique can allow us to characterize the interaction of plasmonic resonators with optically active substrates and 2D nanomaterials. A completely tunable THz plasmonic notch resonance is modulated utilizing a static and dynamic method of optical tunability in silicon. Active tunability is also demonstrated in a graphene-based plasmonic resonator through the hot-carrier multiplication effect. The significance of this work lies in the application of designing controllable devices for future THz communication technologies.

Acknowledgments

I would first like to express my utmost gratitude to my supervisor, Professor Jean-Michel Ménard. From when I was first welcomed into the ultrafast terahertz spectroscopy group, Professor Ménard provided me with the necessary resources, time-commitment, and strong leadership required for me to succeed in the field of experimental physics. He does not take for granted the impact of demonstrating an ever-present enthusiasm for scientific research and the benefit of providing the most positive of reinforcement.

I would also like to thank my colleagues in the group for always providing me with a pleasant and welcoming work environment. Specifically, I would like to thank Wei Cui for spending countless days in the lab with me and teaching me the ropes of working with ultrafast lasers, THz time-domain spectroscopy, the analysis of experimental data, and of course, troubleshooting. Thank you to Lauren Gingras for his impactful mentorship in the early and critical months of starting my experimental work and learning the scientific process. Thank you to Ali Maleki for tirelessly working alongside me on all of my projects throughout my masters program. I would not have succeeded without the support of all my colleagues.

Finally, I express my deepest thank you to my family, who have unwaveringly supported me throughout my graduate studies in physics, even though they wonder why I didn't just get a job as an engineer.

Contents

List of Figures

CV

Scientific article

1. L. Gingras, A. Jaber, A. Maleki, O. Reshef, K. Dolgaleva, R. W. Boyd, and J.-M. Ménard, "Ultrafast modulation of the spectral filtering properties of a THz metasurface," Opt. Express 28, 20296-20304 (2020).

Conference presentations and proceedings

1. A. Jaber, L. Gingras, A. Maleki, O. Reshef, K. Dolgaleva, R. W. Boyd, and J.-M. Ménard, "Ultrafast modulation of the properties of a metasurface for terahertz radiation," Canadian Association of Physicists (CAP) virtual congress (2021).

2. A. Jaber, L. Gingras, A. Maleki, O. Reshef, K. Dolgaleva, R. W. Boyd, and J.-M. Ménard, "Ultrafast Optical Control of a Terahertz Metasurface Filter," in OSA Advanced Photonics Congress, OSA Technical Digest, paper NoM4C.1 (2020).

3. A. Maleki, A. Jaber, A. Singh, Y. Xin, J.-M. Guay, O. Reshef, K. Dolgaleva, R. W. Boyd, B. Sullivan, and J.-M. Ménard, "Broadband bandpass THz filters with stacked metasurfaces," in OSA Advanced Photonics Congress, OSA Technical Digest, paper NoM4C.4 (2021).

4. A. Maleki, A. Jaber, L. Gingras, O. Reshef, K. Dolgaleva, R. W. Boyd, and J.-M.

Ménard, "FDTD analysis of a tunable THz plasmonic metasurface," in Frontiers in Optics / Laser Science, OSA Technical Digest, paper FM7E.4 (2020).

Posters

1. A. Jaber, L. Gingras, A. Maleki, O. Reshef, K. Dolgaleva, R. W. Boyd, and J.-M. Ménard, "Optically Active Tuning of a Terahertz Metasurface Filter," Poster session for the Photonics Online Meetup (2020).

2. A. Jaber, L. Gingras, A. Maleki, O. Reshef, Y. Xin, G. Carlow, T. Schoepp, B. Sullivan, K. Dolgaleva, R. W. Boyd, and J.-M. Ménard, "Optically switchable THz plasmonic filters," Poster session for the Schawlow-Townes Symposium on Photonics, University of Ottawa (2019).

Contributions to the thesis

The collection, analysis, and presentations of experimental results shown in Chapters 3 and 4 of this thesis are my own work with the exception of simulations shown in figure 4.15 that were taken from the scientific article written on the topic of this thesis [1]. Any other figures presented in this thesis that are not explicitly referenced or cited are created by myself.

Chapter 1

Introduction

1.1 THz region of the electromagnetic spectrum

The frontier of terahertz (THz) science deals with the research and development of technologies that operate within the THz region of the electromagnetic spectrum. This region is defined within the gap between the microwave and infrared spectra, typically between 30 µm to 3 mm, as depicted in figure 1.1 [2].

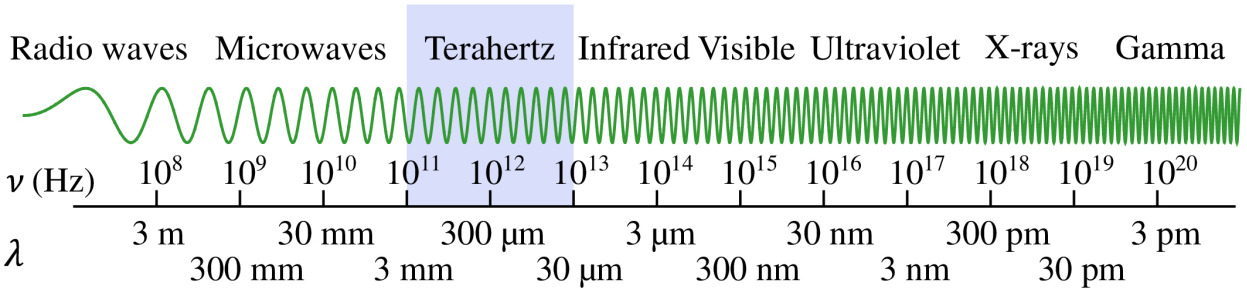

Figure 1.1: The terahertz (THz) region of the electromagnetic spectrum. Taken from [2].

The properties of THz radiation are interesting because they enable technologies that are derived from both microwave and infrared applications [3]. Historically, the THz region was relatively unexplored compared to other regions of the electromagnetic spectrum,

deeming there to be a so called "THz-gap". This was mainly because of a lack of viable THz sources and detectors. Semiconductor-based transistors, operating at and below the microwave region, and laser sources, operating at and above the infrared region, did not overlap in the THz region [4]. It was not until the advent of ultrafast high-intensity lasers and the quantum cascade laser that optics and techniques for the generation, manipulation, and detection of THz were explored [5, 6, 7]. In particular, the development of the THz time-domain spectroscopy (THz-TDS) technique [8, 9, 10] brought about a rapid expansion in the field of THz science. This is a spectroscopic technique in which the full time-domain electric field amplitude and phase of a material can be strongly resolved. The field of THz is now multidisciplinary with some notable applications and developments in chemical sensing and recognition [11, 12], cancer detection [13, 14], next generation (6G) communication technologies [15, 16, 17], and X-ray analogue (T-ray) security screening [18, 19].

1.2 Metasurfaces

One method of rectifying the issue of creating photonic components for the THz comes through the use of metasurfaces: engineered structures of very sub-wavelength thicknesses, typically periodic, in a plane atop a substrate. Metasurfaces modify and control incident light in ways that natural materials cannot [20]. This has led to some novel interactions such as negative refraction [21, 22], metalensing [23, 24, 25], enhanced nonlinearity [26, 27], and optical cloaking [28]. THz metasurfaces are particularly effective because THz wavelengths of operation conventionally require relatively thick optics and materials for sufficient interaction and phase accumulation. In particular, THz metasurfaces have found applications as spectral filters [29, 30], waveplates [31], and perfect absorbers [32]. While metasurfaces are clearly applicable for the design of passive THz components, active tunability is a desired feature for modern and commercially available photonic devices. Tunable THz metasurfaces have

been demonstrated as phase modulators [33], optically tunable spectral filters [34, 1], and gated split-ring resonators [35].

1.3 Outline

In this work, we are primarily interested in the active optical tunability of plasmonic THz metasurfaces on an ultrafast timescale. The performance and dynamics of these devices will be investigated with a THz-TDS technique. The remainder of this thesis will be structured as:

Chapter 2 will be an introduction into the nature of a plasmonic resonance. The types of surface plasmon resonances that can occur at a metal-dielectric interface will be discussed in the context of THz applicability. A methodology for the creation of metasurface spectral filters from plasmonic array resonances will be described in the context of dispersion matching, lumped-element circuit models, and finite-difference time-domain (FDTD) simulations. Finally, the properties of the materials experimentally explored for optical tunability, silicon and graphene, are defined in terms of Drude-like conductivity models.

Chapter 3 deals with defining the technique of time-resolved THz spectroscopy and the experimental implementation utilized in this work. The process of THz generation and detection through the use of nonlinear crystals will be described in detail, with an underlying background of the relevant nonlinear processes and effects. The implementation of an experimental THz-TDS setup is explained in a step-wise manner in how near-infrared ultrafast pulses can generate and probe single cycle THz electric fields. Finally, an example analysis of a resonant THz time-domain transient is shown.

Chapter 4 pertains to the experimental results and discussion of metasurface tunability. This will include the underlying substrate and material characterization of silicon, a THz transparent cyclo-olefin polymer, and graphene. A modification to the THz setup is

schematically depicted and explained to enable optical pump - THz probe measurements. Several THz plasmonic resonator designs are then experimentally characterized and compared to simulation. Static and dynamic schemes of ultrafast optical pump-probe tunability are defined and compared. Observations of the near-complete control of a THz resonance are shown, with simulations enabling and verifying explanations. Finally, a photoinduced negative THz photoconductivity in graphene is demonstrated in a metasurface design, with a corresponding characterization of the carrier dynamics of graphene.

Chapter 2

Theory

2.1 Plasmons

The field of plasmonics focuses on the behaviour of coherent free electron oscillations along metal-dielectric interfaces. These oscillations are coupled to an incident electromagnetic field and referred to as surface plasmon polariton (SPP) modes [36]. In the context of THz metasurfaces, we are concerned with the localization of plasmonic modes in periodic metal lattices on a surface.

2.1.1 Propagating surface plasmon resonances

There are two types of plasmonic resonances: propagating surface plasmon resonances (PSPR) and localized surface plasmon resonances (LSPR). In the case of a PSPR, a metallic structure is placed at a dielectric interface and has at least one dimension that is larger than the wavelength of incident light. Figure 2.1 is a schematic depiction of this type of plasmonic coupling. An electromagnetic field is incident onto the metal structure with a k wavevector, not parallel to the structure. The field then couples with and excites free electrons in the structure to create a PSPR that propagates along the metal-dielectric interface. Since this is

a resonant effect, the plasmon mode has an associated resonance length and the plasmonic mode can reflect back and forth at the ends of the structure. In the case of a nanowire, as depicted in the schematic of figure 2.1, the resonance condition is the Fabry-Perot condition given by [37],

$$L = n\lambda_{PSPR} \tag{2.1}$$

where L is the resonance length, λ_{PSPR} is the wavelength of the plasmonic mode, and n is a positive integer. The resonance length describes the plasmon propagation distance along the metal-dielectric interface at which the excitation intensity decays by $1/e$ as a result of absorption in the metal. Additionally, since the metallic structure is larger than the wavelength of the incident field, the excitation is not uniformly experienced.

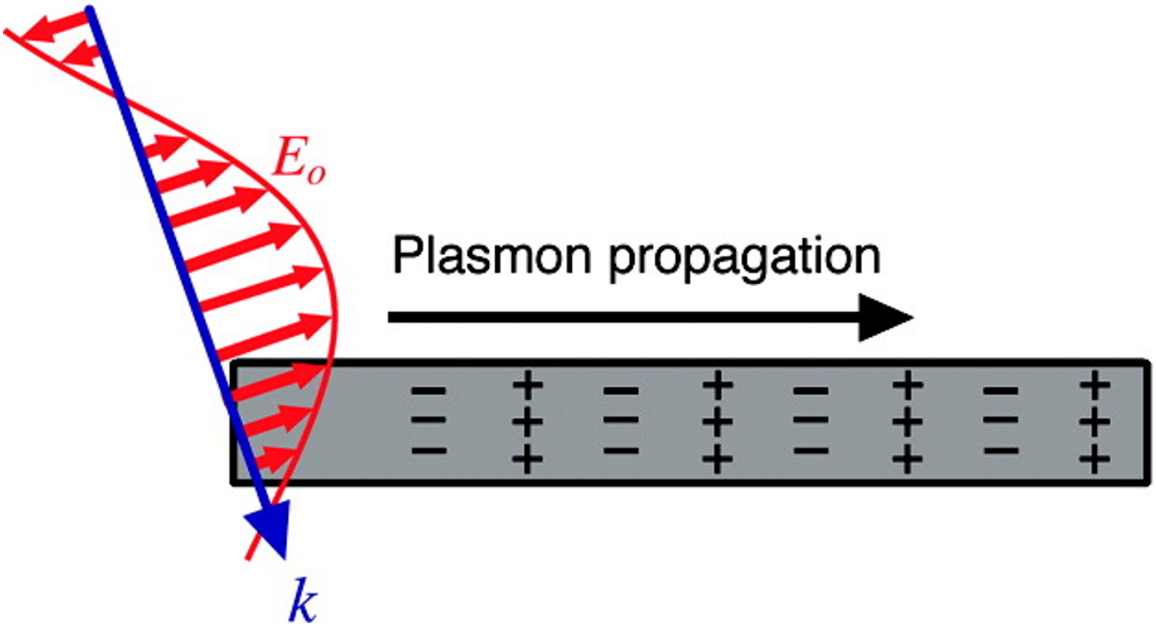

Figure 2.1: Schematic of a propagating surface plasmon resonance. An incident electromagnetic field couples to a metallic structure with a geometry that is larger than its wavelength. The field excites free electrons in the metal to create a propagating plasmonic mode that travels along the metal-dielectric interface. The plasmonic mode in the structure has an associated resonance frequency, resonance length, and reflects at the boundaries. Adapted from [36].

A surface plasmon resonance (SPR) obeys a well known dispersion relation [38, 39],

$$k_{SPR} = k_0 \sqrt{\frac{\varepsilon_d \varepsilon_m}{\varepsilon_d + \varepsilon_m}} \tag{2.2}$$

where ε_d is the dielectric constant of the medium, ε_m is the dielectric constant of the metallic structure, and k_0 is the wavevector of the excitation field. Throughout this chapter, the dielectric functions are implicitly understood to vary as a function of frequency. The associated resonance length of a SPR is given by [39],

$$L_{SPR} = \frac{1}{2\mathbf{Im}(k_{SPR})} \tag{2.3}$$

and determines the length of plasmon mode propagation on the metal-dielectric surface.

2.1.2 Localized surface plasmon resonances

In the case of an LSPR, metal particles are placed in a plane with a metal-dielectric interface as shown schematically in figure 2.2. The particle sizes are much smaller than the wavelength of an incident time-varying electromagnetic field with an in-plane wavevector k and they experience a uniform excitation. The time-variation of the excitation leads to the displacement and oscillation of electrons in the individual particles. At a certain excitation frequency which matches the electron oscillation frequency, a resonance can be achieved, creating the LSPR mode.

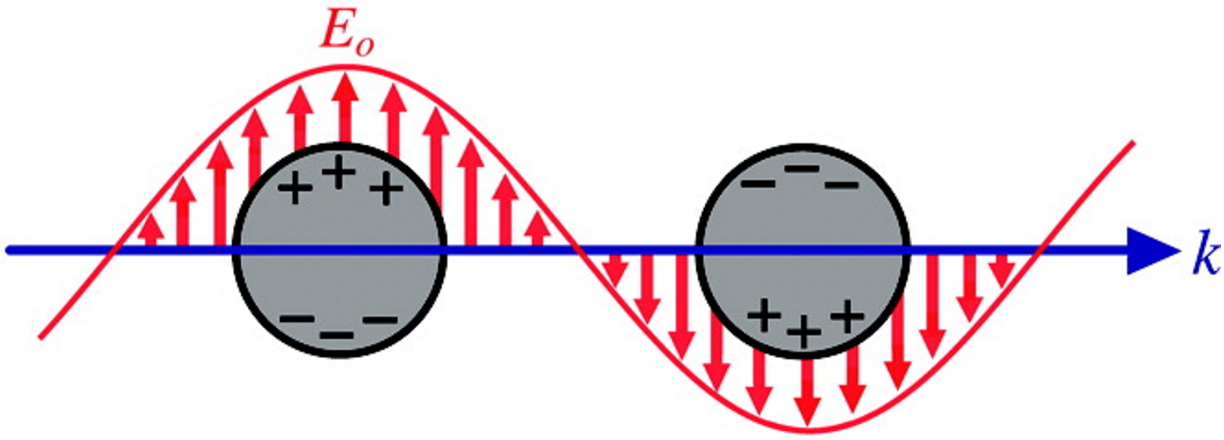

Figure 2.2: Schematic of a localized surface plasmon resonance. A time-varying electric field travels in the plane of metallic structures that are substantially smaller than its wavelength. The uniformly felt field displaces electrons in the structures in an oscillatory fashion. A localized surface plasmon mode is defined at the resonance condition of the field-electron oscillations. Adapted from [36].

The extinction cross section and quality factor of an LSPR in metallic spheres can be calculated from Mie theory under the assumption of a small particle size compared to the wavelength and are given by [40]. The extinction cross section accounts for optical absorption and scattering and is calculated from,

$$C_{ext} = \frac{24\pi^2 R^3 \varepsilon_d^{3/2}}{\lambda}[\frac{\varepsilon_i}{(\varepsilon_r + 2\varepsilon_d)^2 + \varepsilon_i^2}] \tag{2.4}$$

where R is the radius of the metal spheres, λ is the excitation wavelength, ε_r and ε_i are the real and imaginary dielectric permittivities of the metal spheres, and ε_d is the dielectric constant of the surrounding medium. The strongest resonance condition is achieved when the extinction cross section is maximum, requiring ε_r=$-2\varepsilon_d$ and ε_i approaching zero. The quality of the resonance is best quantified through the quality factor [40],

$$Q = \frac{\omega(d\varepsilon_r/d\omega)}{2(\varepsilon_i)^2} \tag{2.5}$$

where ω is the radial frequency. The quality factor can additionally be defined as the ratio between a resonator's center-frequency and its full width at half maximum bandwidth. It is clear that the properties of a LSPR are strongly controlled by the parameters of the metallic structure and medium. The plasma frequency of a material is typically given by [39],

$$\omega_p = \sqrt{\frac{Ne^2}{\varepsilon_0 m^*}} \tag{2.6}$$

where N is the carrier density, e is the electric charge, m^* is the effective mass of carriers, and ε_0 is the free space permittivity.

2.1.3 THz plasmonics

The properties of metals at THz spectral ranges result in some notable distinctions between optical and THz plasmons. The magnitude of metallic complex permittivities at THz wavelengths are very large relative to those at visible and near-infrared wavelengths [41]. In the Drude picture, this is because metals have a large free electron density and consequently a much larger plasma frequency than THz frequencies, increasing the relative permittivity magnitude. When looking at the dispersion relation of plasmon waves, given in equation 2.2, we can observe that having a large metallic dielectric constant relative to the medium results in the plasmon wavevector tending to the value of the free space wavevector multiplied by the dielectric permittivity [42]. This is seen from tending ε_m to infinity in the dispersion equation to yield the following approximation,

$$k_{SPR} = k_0 \sqrt{\frac{\varepsilon_d(\infty)}{\varepsilon_d + (\infty)}} \approx \varepsilon_d k_0 \tag{2.7}$$

The large magnitude of complex metal permittivity also implies a negligible field penetration into the metal. For the dispersion relationship of an infinite metal-dielectric interface at

THz wavelengths, the relatively smaller KSPR also implies a longer resonance propagation length along the interface [43]. For the case of an LSPR type configuration, where there is a lattice of subwavelength metallic elements under excitation, propagating surface plasmon waves cannot exist. Instead, a plasmonic dispersion relationship can be constructed from the lattice or grating parameters, treating the array as a quasicrystal [42].

2.2 Plasmonic spectral filters

In this work, we make use of THz spectral filters that consist of sub-THz wavelength plasmonic microstructures in an array that covers the entire spatial region of THz excitation. This array functions in the described LSPR plasmonic regime, in which standing plasmon waves are produced by an effectively uniform electromagnetic field.

2.2.1 Plasmonic array metasurfaces

Metasurfaces typically consist of periodic arrays of subwavelength plasmonic structures that are optically thin. In this configuration, the individual structures of the array are referred to as meta-atoms and the entire structure is effectively considered to be two-dimensional. This is a useful convention because a single, simple, subwavelength metallic structure, such as a dipole element, is usually described in terms of a polarizability change caused by an incident electromagnetic field [44], similar to an atom's linear lorentzian response. In terms of the plasmonic response, the modes supported by a single meta-atom are modified by the presence of its neighboring meta-atoms to alter its effective polarizability and also produce new collective plasmonic array modes. The collective modes of interest, known as surface lattice resonances arise when the periodicity of the metasurface is on the order of the resonance wavelength of the meta-atoms [44]. In this regime, the far-field interaction of meta-atoms in the array can constructively interfere to produce the collective resonance(s).

As an example, a metasurface consisting of a metal square array on a dielectric substrate is shown schematically in figure 2.3. As long as the thickness of the metal structures is optically thin, on the nanoscale for THz metasurfaces, a square array is soley characterized by its side widths (W) and lattice periodicity (P). Like the behaviour of plasmon modes at singular metal-dielectric interfaces, the plasmonic response of a metasurface can be defined by its dispersion relation. In the simple case of a square metasurface, the dispersion relation is given by [45],

$$K_{SPR} = k_x \pm nG_x \pm mG_y \tag{2.8}$$

where $k_x = (2\pi/\lambda)sin(\theta)$ is the wavevector of the incident field in the metasurface plane, $G_x = G_y = 2\pi/P$ are the grating momentum wavevectors for a square array [45], and n, m index the grating orders of the metasurface. This relation of course requires the periodicity of the array to be larger than the width of the square metal elements.

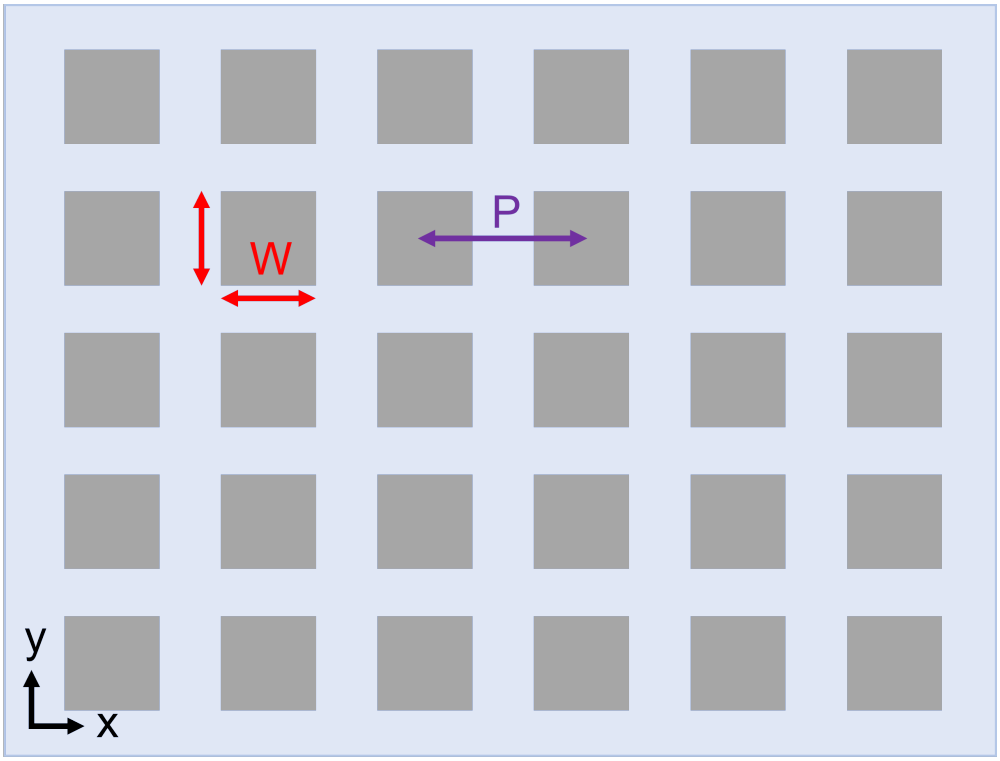

Figure 2.3: Schematic of a plasmonic array of sub-wavelength metallic squares on a dielectric substrate.

2.2.2 Lumped-element circuit model

Another method of understanding the resonance properties of a plasmonic array is with an equivalent lumped-element circuit treatment. Equivalent circuit models were first defined in [46] for metal mesh spectral filters. In such a model, the metal mesh is either modelled to be capacitive or inductive in nature, with the difference being whether the fill factor of the design is positive or negative. The distinction, still utilizing the square array model, is depicted schematically in figure 2.4.

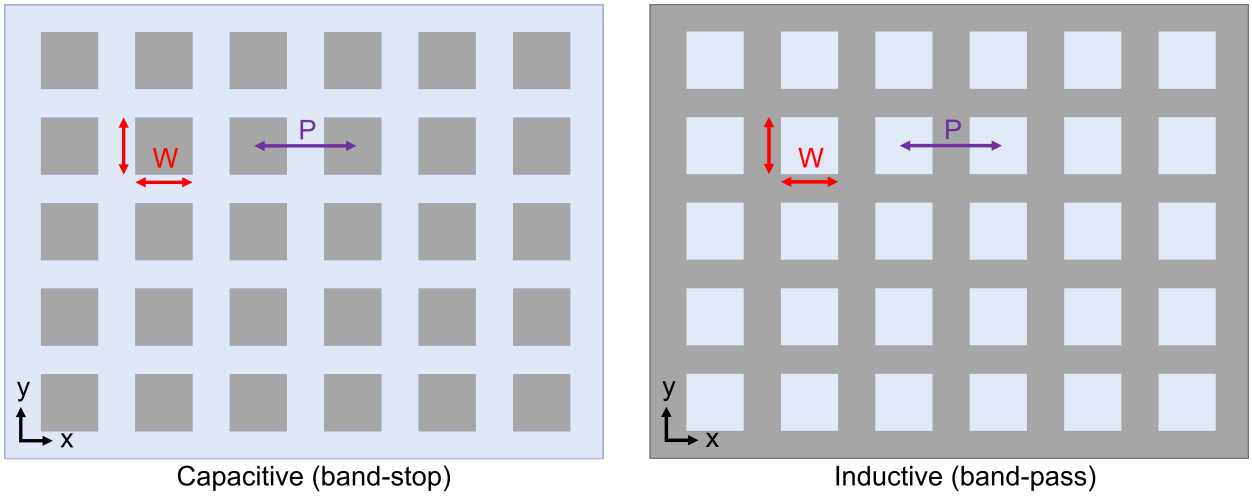

Figure 2.4: Schematics of capacitive and inductive square arrays. In an equivalent circuit model for a metal mesh filter, the difference between a capacitive and inductive mesh is determined by the metallic (grey) fill factor of the design, compared to the dielectric substrate (light blue).

The equivalent RLC circuit is defined within an impedance matched transmission line model in which the capacitive or inductive property is determined by the placement of the lumped-elements [29]. For the work presented in this thesis, we utilize plasmonic metasurfaces that consist of cross-shaped array elements [1]. These meta-atoms are ideal for characterizing the plasmonic array responses because they function as two orthogonal metallic dipoles. The array has a polarization independent dipole response in the form of a lorentzian lattice resonance. The design and fabrication of the inductive cross meshes is well documented [29, 30, 47], but in this work we utilize capactive designs to create notch (band-stop) filters. In a free-standing metal mesh design, Babinet's principle states that the metal region can be switched with the dielectric region to switch the transmission properties of a filter to reflection properties and vice-versa [46]. The nomenclature of inductance or capacitance derives from the fact that the electric susceptibility of an inductive design is inverted to produce its corresponding capacitive design. The equivalent circuit model for a capacitive cross mesh can be modelled utilizing the design procedure outlined in [46]. A transmission

line model is shown in figure 2.5.

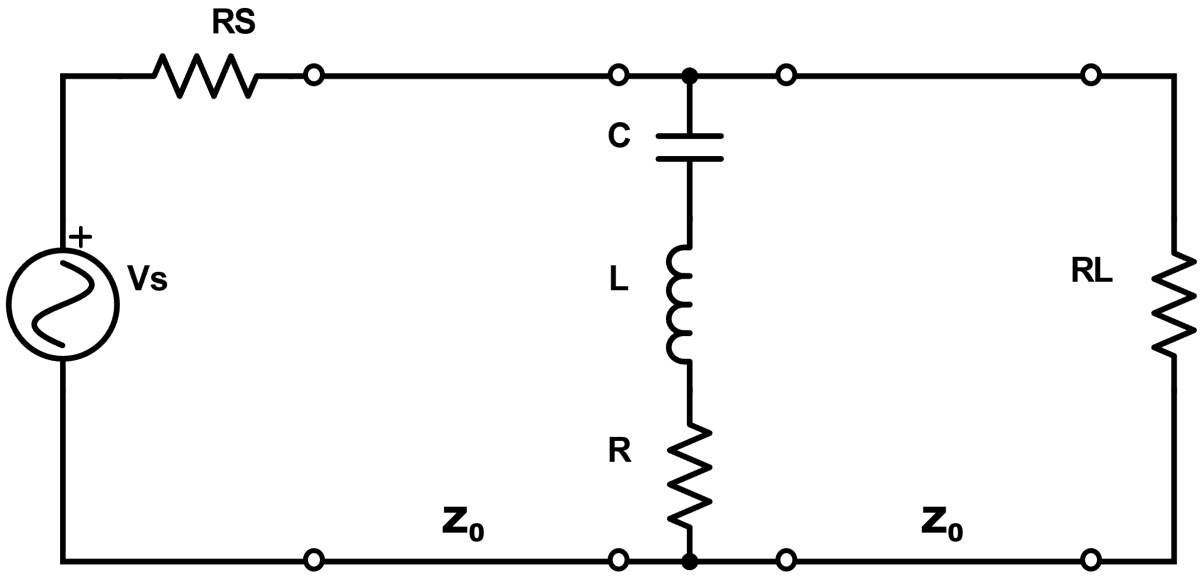

Figure 2.5: Transmission line equivalent circuit model of a capacitive cross mesh. The model enables the determination of the transmissivity and resonance frequency of the plasmonic filter array. Source and load resistances are matched to the characteristic impedance of the transmission lines, Z_0.

In this model, an equivalent RLC circuit representing the cross mesh filter is embedded in a transmission line model. The AC source represents the incident electromagnetic field onto the metasurface. Source and load resistors are utilized for impedance matching to the line ($Z_0 = RS = RL$). This is only useful to idealize the model, since if a transmission line is not impedance matched, standing waves will form due to in-plane reflections [29]. The capacitance and inductance values determine the resonance frequency by,

$$\omega_0 = \frac{1}{\sqrt{LC}} \tag{2.9}$$

which can be used to determine the transmissivity of the mesh filter [46],

$$T(\omega) = \frac{R^2 + Z_0^2\Omega^2}{(1 + R^2) + Z_0^2\Omega^2} \tag{2.10}$$

where ω is the radial frequency and $\Omega = (\omega/\omega_0) - (\omega_0/\omega)$. The relation of an equivalent electrical circuit with lumped elements (i.e. capacitor, inductor, resistor) to the parameters of a metallic mesh is as follows: In a simplified free-standing mesh, the periodicity (P) of the mesh elements is defined as the inverse of the resonance frequency of the RLC circuit. The inductor and capacitor values of the equivalent circuit are related to the distributed inductance and capacitance values of the metal mesh elements. These distributed values define the electrical susceptance and are directly related to the dimensions and geometry (W) of the mesh elements. The resistance in the RLC component models the loss of the metal mesh elements and depends on the conductivity of the metal used to create the mesh. Empirically, a metallic mesh can be accurately modelled by an equivalent circuit model when the grid ratio $W/P < 0.2$ [46]. This is because larger metal element dimensions contribute to the electrical susceptibility of the grid, altering the resonance frequency. At microwave frequencies, metal mesh design is typically accomplished with a microstrip transmission line analysis, facilitated by harmonic balance frequency-domain simulations [48].

2.2.3 FDTD simulations

In this thesis, plasmonic metasurfaces are designed and simulated utilizing a finite-difference time-domain (FDTD) technique. We use the FDTD software package of Lumerical Inc. [49] to simulate periodic filter array responses in terms of power transmission and electromagnetic field distributions. The basic technique of the FDTD technique involves solving Maxwell's curl equations in incremental fashion, given by [49] as,

$$\frac{\partial D}{\partial t} = \nabla \times H \tag{2.11}$$

and,

$$\frac{\partial H}{\partial t} = -\frac{1}{\mu_0} \nabla \times E \tag{2.12}$$

where E is the electric field, H is the magnetic field, $\mu = \mu_0$ is the magnetic permeability under a nonmagnetic assumption, and D is the displacement field given by,

$$D(\omega) = \varepsilon_0 \varepsilon_r(\omega) E(\omega) \tag{2.13}$$

where ε_0 is the electric free space permittivity and $\varepsilon_r(\omega)$ is the dielectric constant.

In the case of a three-dimensional simulation, the technique involves meshing the simulation region into finite grids, known as Yee cells [50]. To outline the basic solving procedure: At one instant in time, the electric field components of a Yee cell occupying one spatial region are solved. At the next instant of time, the magnetic field components in the same spatial region are solved. This process is repeated until the entire simulation region has been evaluated for a given simulation time. The simulation time is determined by the time it takes the electromagnetic field in the simulation region to decay to a specified minimum value.

2.3 Optically induced carriers

One goal of the work presented in this thesis is the demonstration of optically tunable THz metasurfaces. This is accomplished in one of two methods, either the substrate of the metasurface is made to be tunable, or the plane of the metasurface is made to be tunable. In the first case, we demonstrate the optical tunability of silicon in the THz region. In the second case, we demonstrate the optical tunability of graphene in the THz region. In both cases, the properties of these materials are understood in terms of a Drude or Drude-like model.

2.3.1 Properties of Silicon

Silicon is an indirect band-gap semiconductor which, in the THz region, can be very well accurately modelled by a Drude model [51, 52, 53]. It exhibits a THz transmission of around 60% and a real part of the refractive index of 3.4 [54]. In the use of silicon as a metasurface substrate, forming the metal-dielectric plasmonic interface, the real and imaginary part of the refractive index determines the effective array periodicity and modifies the plasmonic mode propagation length, respectively. Measured conductivity data that matches the bulk float-zone silicon substrates utilized in this work can be found in [55]. This data can be fit to a Drude model for FDTD simulation purposes and the interpretation of optical tunability in silicon. The complex conductivity given by the Drude model is written [56] as,

$$\sigma(\omega) = \frac{\sigma_0}{1+\omega^2\tau^2} + i\omega\tau\frac{\sigma_0}{1+\omega^2\tau^2} \tag{2.14}$$

where τ is the scattering rate, ω is the radial frequency, and σ_0 is the DC conductivity contribution given by,

$$\sigma_0 = \frac{ne^2\tau}{m} \tag{2.15}$$

where m is electron mass, e is the electron charge, and n is the carrier density.

Experimentally, we are interested in the optical interaction of silicon with 515 nm light. At this wavelength, silicon has an absorption length that lies within 1 μm [55]. This is useful because most photogenerated carriers in the silicon substrate will be generated near the plane of the metasurface. These generated carriers modify the Drude response of silicon by increasing the real part of the refractive index, which will be shown to affect the effective periodicity of a metasurface [1]. Furthermore, the free-carrier absorption near the metasurface increases the scattering rate and increases the plasmon loss. The Drude model is shown to be very effective in modelling optically induced changes in silicon [57, 1].

2.3.2 Properties of Graphene

Graphene is a well documented two-dimensional nanomaterial [58], consisting of periodic hexagonal honeycomb lattice of carbon in a two-dimensional plane. The most important characteristic of graphene is in its notably gapless band-structure, schematically depicted in figure 2.6, in terms of energy-momentum diagrams. The doping concentration of graphene is characterized in terms of its chemical potential, μ, defined by [59],

$$n = \frac{(\mu/\hbar f)^2}{\pi} \tag{2.16}$$

where n is the carrier density, f is the frequency and $\hbar$ is the reduced Planck's constant.

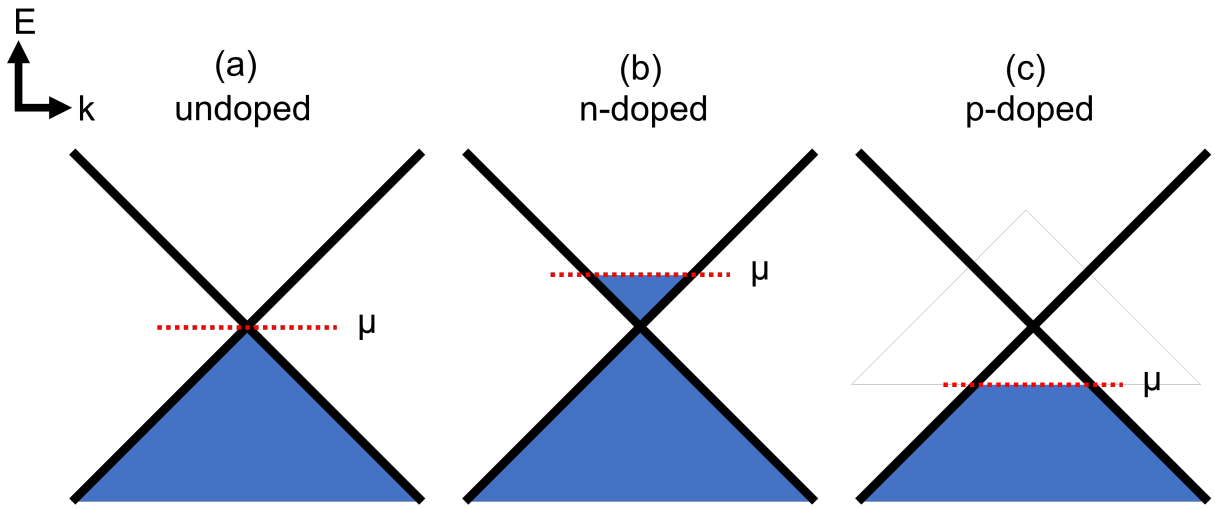

Figure 2.6: Schematic band-structure of doped and undoped graphene. (a) Depicts undoped graphene with a chemical potential at $E = 0$. (b) Depicts an n-doped graphene band-structure, in which E > 0 and (c) depicts a p-doped band-structure in which E < 0.

In figure 2.6 (a), the case of undoped graphene is depicted in which the chemical potential μ at the crossing point between the graphene valence and conduction bands, defined at $E = 0$. This is the configuration in which graphene is considered to be a semimetal. Figures 2.6 (b) and 2.6 (c) depict the chemical potential of n-doped ($E > 0$) and p-doped ($E < 0$) graphene,

respectively.

The optical conductivity of graphene can be written in terms of combined intraband and interband contributions as [59],

$$\sigma(\omega) = \frac{e^2\omega}{i\pi\hbar}\int_{-\infty}^{\infty}\frac{|E|}{\omega^2}\frac{df_0(E)}{dE}dE - \frac{e^2\omega}{i\pi\hbar}\int_{0}^{\infty}\frac{f_0(-E)-f_0(E)}{(\omega+i\delta)^2-4E^2}dE \tag{2.17}$$

where E is the energy, ω is the radial frequency, h is Planck's constant, e is the electron charge, δ is an infinitesimal quantity used to avoid the pole, and $f_0(E)$ is the Fermi function defined as,

$$f_0(E) = exp[(E-\mu)/T] + 1 \tag{2.18}$$

where T is the temperature. In the THz spectral region, intraband transitions dominate, allowing for us to only consider the first term in the expression [60, 61]. Once integrated, this term can be modified to take the same form as the Boltzmann-Drude model, with the addition of a scattering term, $i\tau^{-1}$ [59]. The final expression for the intraband graphene conductivity is given by,

$$\sigma^{intra}(\omega) = \frac{ie^2|\mu|}{\pi\hbar(\omega+i\tau^{-1})} \tag{2.19}$$

and is implemented as a surface conductivity with our FDTD solver to model the intrinsic doping concentration and scattering rates of experimentally produced graphene samples.

In semiconductors like silicon, optical doping increases THz photoconductivity and thus lowers THz transmission, with larger carrier densities contributing to a larger transmission attenuation. This follows through with the case of undoped graphene, which has been reported to have a typical phonon emission dominated carrier relaxation process [62]. An increase in photoconductivity similar to a semiconductive material is observed, but on a smaller scale, due to the single atomic layer nature of graphene. The response of relatively undoped graphene to increasing optical pump energies can be seen in figure 2.7 [63].

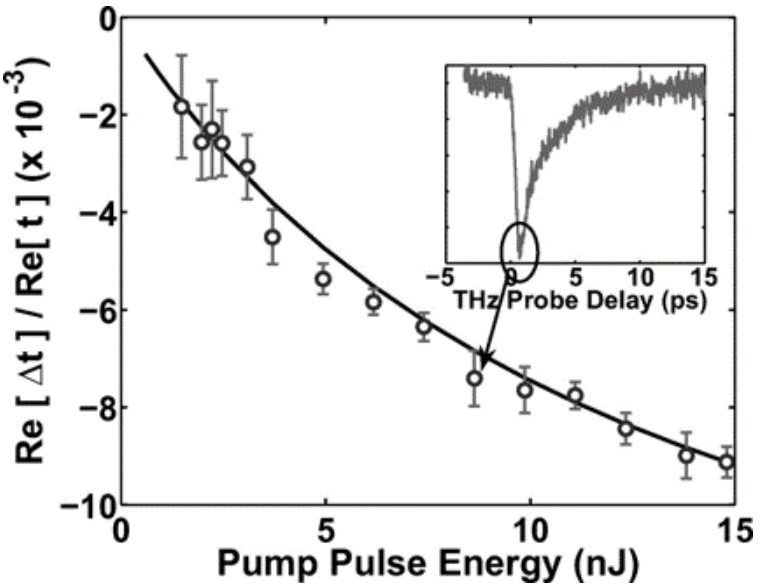

Figure 2.7: An experimental plot of peak differential THz transmission in graphene, around 0.3-3 THz, as a function of optical pump energy. Data points are taken at the peak magnitude response of an optical pump - THz probe measurement of undoped graphene, as seen in the inset. Adapted from [63].

Here, the peak differential THz transmission of graphene sample is plotted as a function of optical pump energy. The differential THz transmission is measured, in the inset, as a function of optical pump - THz probe time delay and visualizes the THz carrier dynamics of undoped graphene.

In contrast, photoexcited carriers in sufficiently doped graphene have been shown to dominantly relax through a carrier-carrier scattering pathway in which energy is transferred to secondary electrons in the conduction band [64, 65]. This creates a carrier multiplication effect in which a sea of hot carriers is formed in the conduction band after a photoexcitation. As a result, the higher carrier temperature lowers the THz photoconductivity of graphene, and thus increases THz transmission. This process only dominates when there are sufficient carriers in the conduction band to begin this carrier multiplication process, facilitated by intrinsically doped graphene of large concentrations. The differential THz transmission as a function of pump fluence is shown in figure 2.8 [64]. In this plot, figure 2.8 (a) shows the

differential THz transmission as a function of optical pump - THz probe delay at two different pump photon energies. (b) Shows that the the transmission change, while relatively small in scale, is demonstratively linear with respect to absorbed photon density (proportional to pump fluence) with a slope given by the photon energy.

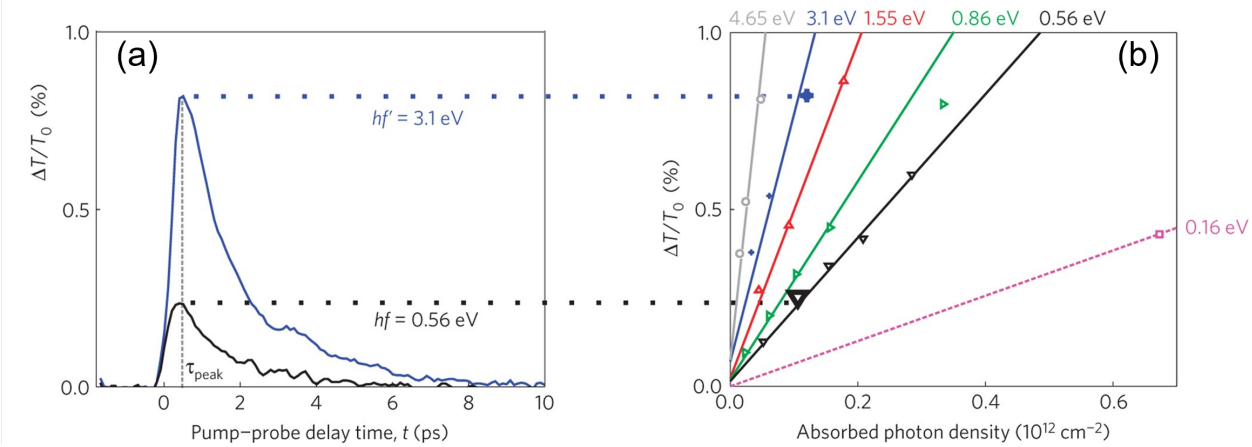

Figure 2.8: THz response of optically pumped doped graphene. (a) Experimental plots of differential THz transmission as a function of optical pump - THz probe time delay. (b) Plots of peak differential THz transmission as a function of absorbed photon density (proportional to pump fluence) and pump photon energy. Adapted from [64].

In this work we will utilize heavily p-doped graphene samples. This is both due to the fabrication process of the graphene we use experimentally and to explore the effect of a negative THz photoconductivity in addition to the positive photoconductivity of silicon, on a metasurface. The carrier dynamics of silicon and graphene are similarly explored in terms of optical pump - THz probe spectroscopy.

Chapter 3

Experiments

3.1 Time resolved spectroscopy

The experimental results that are discussed in this thesis are measured using a THz time-domain spectroscopy (THz-TDS) technique. This is a time-resolved measurement with the purpose of probing the electric field of THz pulse in the time-domain. We will discuss the framework and experimental setup by which THz pulses can be generated and detected using the nonlinear optical processes of optical rectification and electro-optic sampling. In the current state of THz detectors, there are no viable methods to measure the time-domain response of a THz pulse electronically. Unlike the microwave region of the electromagnetic spectrum, having a large enough circuit frequency response to detect broadband THz is not technologically feasible. Also, even in terms of intensity detection, there are only relatively few methods for detection, mostly utilizing thermal detectors or through carrier photogeneration in semiconductors [66, 67], and without comparable efficiency and responsitivity to shorter wavelength detectors. Essentially, the technique of THz-TDS is accomplished in detection by utilizing the generated THz to modulate the intensity of femtosecond near-infrared pulses, much shorter in time than the picosecond pulse duration of THz pulses, which are

then detected as a function of time utilizing silicon photodiodes. During this chapter, we will explain the process of THz generation and the method of detecting the time-domain response of a THz pulse utilizing near-infrared intensity detection.

3.1.1 THz generation

In the experimental setup, THz generation is accomplished through the second order process of optical rectification in a nonlinear crystal.

Basic nonlinear optics background

In the linear optical case, the polarization, $P(t)$, of a material depends on the linear susceptibility, $\chi^{(1)}$ of the medium and the electric field strength, $E(t)$ of an incident optical beam. In free space the relationship is given by,

$$P(t) = \varepsilon_0 \chi^{(1)} E(t) \tag{3.1}$$

where ε_0 is the permittivity of free space. In a nonlinear medium, the polarization is further generalized in a power series to account for nonlinear polarization responses and represented by,

$$P(t) = \varepsilon_0 [\chi^{(1)} E(t) + \chi^{(2)} E^2(t) + \chi^{(3)} E^3(t) + ...] \tag{3.2}$$

where we can further compartmentalize the components of the polarization as a sum of the linear and nonlinear contributions as,

$$P(t) = P^{(1)}(t) + P^{(2)}(t) + P^{(3)}(t) + ... \tag{3.3}$$

with the nonlinear component we are interested in, $P^{(2)}(t)$, being referred to as the second order polarization, and $\chi^{(2)}$ being the second order susceptibility. The polarization of the

nonlinear media is presented as having an instantaneous response at time t, the applied optical field, an assumption that only holds when the media is lossless and dispersionless [68].

As will be further described nonlinear crystals used for THz generation that have second order susceptibilities have non-centrosymmetric crystalline structures. In this work we utilize gallium phosphide (GaP) crystals as non-centrosymmetric nonlinear media. These crystals have the property of lacking an inversion symmetry in their structure. As a result, the time averaged response of an applied electric field to a non-centrosymmetric crystal will not be zero, since polarization response of such a media is directional. Figure 3.1 demonstrates the different polarization responses of linear and nonlinear media to an applied monotone electric field. It is clear when looking at figure 3.1 (d) that the time-averaged polarization response is nonzero. In fact, it is from this averaged offset in the response that the optical rectification effect used for THz generation arises from [69]. The presence or lack of inversion symmetry in a nonlinear media also determines the parity of the harmonics of the applied field that are included in the polarization response. In centrosymmetric media, only odd harmonics of the applied field are present in the response while non-centrosymmetric media have both even and odd harmonics. The inversion symmetry property of a nonlinear crystal therefore determines the presence or lack of higher order electric susceptibilities. Crystals with an inversion symmetry have no bulk $\chi^{(2)}$ and cannot be used for THz generation.

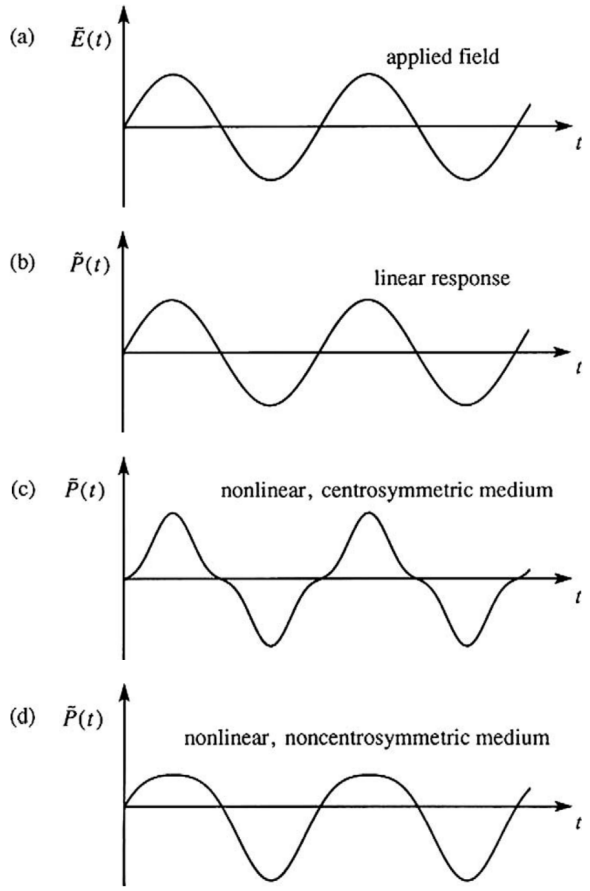

Figure 3.1: The difference between the nonlinear responses of centrosymmetric and non-centrosymmetric media. (a) and (b) show the an applied monotone electric field and a corresponding linear polarization response in a medium. (c) Shows the response of a nonlinear medium with an inversion symmetry and (d) shows the response of a medium without inversion symmetry. Adapted from [68].

Linear optical properties of materials are typically described using the Lorentz atomic model in terms of a classical harmonic oscillator. This model describes the driving force of an applied electric field on the position of electron which is bound to an atom. The bound electron behaves as though it is part of a spring-mass system with the atom. In the case of describing a solid material, one must take into account internal collisions between electrons and emitted radiation due to acceleration with a dampening factor [70]. The

electron displacement due to the presence of an applied optical field can be described by,

$$m\frac{d^2x}{dt^2} + m\gamma\frac{dx}{dt} + m\omega_0^2 x = -qE_x \tag{3.4}$$

where x is the position of the electron, m is the mass of the electron, γ is the dampening factor, and q is the charge of the electron. While the second term in the equation describes the dampening force on the electron, the restoring force is described by the third term.

$$F_{restoring} = -m\omega_0^2 x \tag{3.5}$$

The displacement of the electron from the equilibrium position as a result of an applied electric field is then easily understood from the corresponding potential energy function,

$$U(x) = -\int F_{restoring} dx = \frac{m\omega_0^2 x^2}{2} \tag{3.6}$$

which is expected from a spring-mass system. If now, the electron displacement to an applied field is nonlinear, we must modify equation 3.4 with a nonlinear term [68],

$$m\frac{d^2x}{dt^2} + m\gamma\frac{dx}{dt} + m\omega_0^2 x + max^2 = -qE_x \tag{3.7}$$

where the parameter a describes the strength of the nonlinear interaction. The additional term arises from assuming a nonlinear contribution to the restoring force on the electron, coming from the nonlinear medium. The potential energy function that represents the nonlinear displacement in x can be calculated from,

$$F_{restoring} = -m\omega_0^2 x - max^2 \tag{3.8}$$

leading to,

$$U(x) = -\int F_{restoring} dx = \frac{m\omega_0^2 x^2}{2} + \frac{max^3}{3} \tag{3.9}$$

Figure 3.2 compares the harmonic potential of a linear optical medium and the derived anharmonic potential of a nonlinear optical medium. Since nonlinear term included in the Lorentz displacement was second order, the anharmonic potential shown in this plot is for a non-centrosymmetric medium.

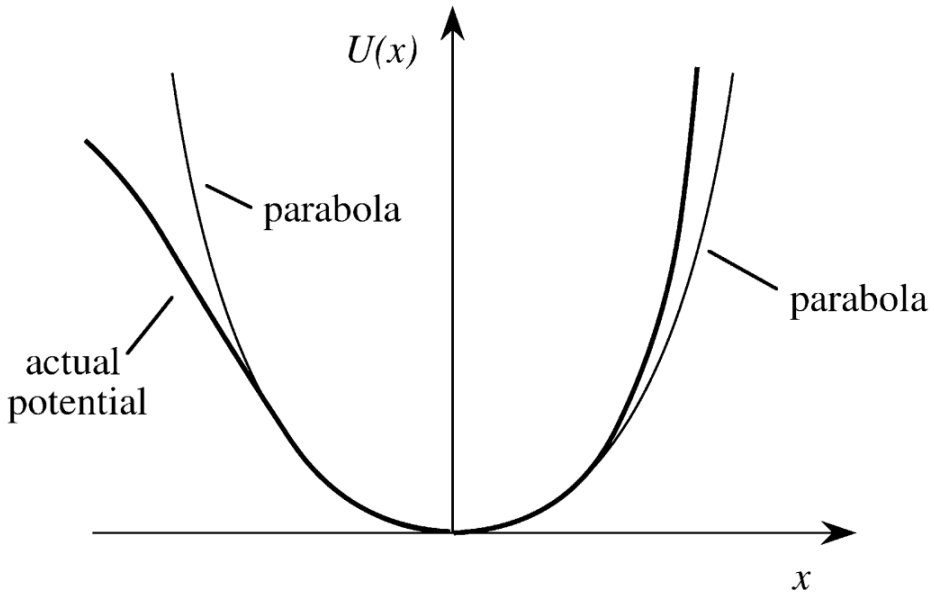

Figure 3.2: Potential energy function of a linear (non-bold) and nonlinear (bold) Lorentz electron displacement in a medium. Adapted from [68].

Finally, it is possible and useful for the analysis of the propagation of an electric field through a second order nonlinear medium to separate the linear and nonlinear polarization contributions in the electromagnetic wave equation. A modified, driven, nonlinear wave equation can be defined as,

$$\nabla^2 E - \frac{1}{c^2 \varepsilon_0} \frac{\partial^2 D^{(1)}}{\partial t^2} = \frac{1}{c^2 \varepsilon_0} \frac{\partial^2 P^{(2)}}{\partial t^2} \tag{3.10}$$

where t is time and,

$$D^{(1)} = \varepsilon_0 E + P^{(1)} \tag{3.11}$$

with c being the speed of light [68].

Optical rectification

In a basic analysis of driven nonlinear optical media, the incident electric fields are assumed to be monotone continuous waves represented by $E(t) = E_0 e^{-i\omega t}$+c.c where E_0 is a constant field amplitude, ω is the radial frequency of the field, and "c.c" is the complex conjugate of the expression. This approximation is valid in our case for the conceptual understanding of nonlinear dynamics because the generating electric field is the output of an ultrafast laser source centered at 1030 nm. The Gaussian wavelength distribution of a typical laser output is not spectrally broad enough to experience large changes in the optical properties of a medium. For THz generation we are interested in the effect of optical rectification from difference frequency mixing. So for a Gaussian laser source centered around 1030 nm, the broadest THz wavelengths that can be generated are fundamentally limited by the broadest wavelengths available from the source that impinges onto the nonlinear crystal. A schematic representation is shown in figure 3.3.

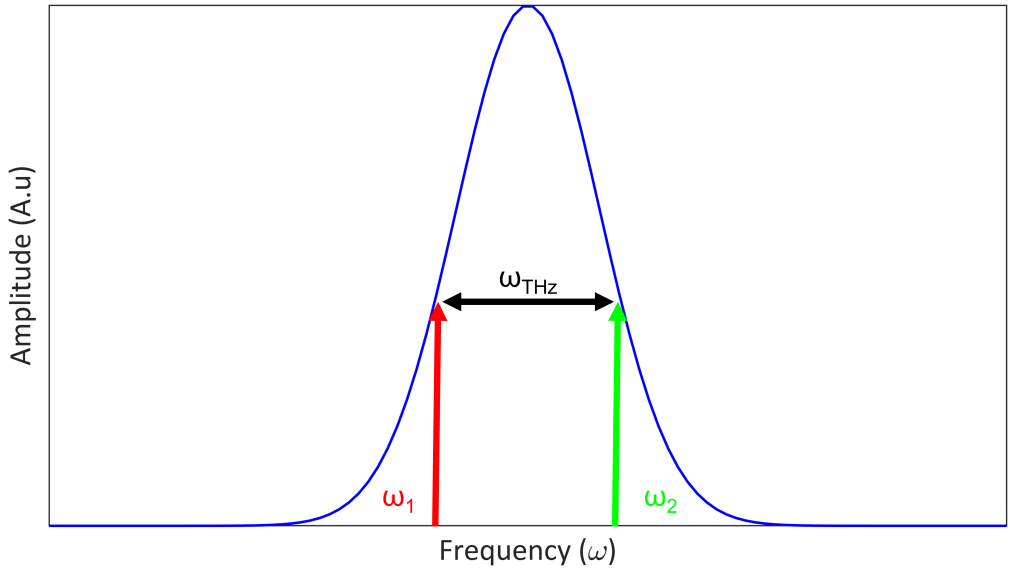

Figure 3.3: A schematic of difference frequency mixing to generate THz. The spectral distribution of an input laser field to a nonlinear crystal is depicted. The amount of THz frequencies that can be generated are fundamentally limited by the maximum difference of the frequencies available in the source.

Here, an example laser output, similar to what is used in our THz setup, with a Gaussian spectral distribution is depicted. For difference frequency generation, we care about the difference between the bounding frequency components available in the input laser field, as these components also bound the generated THz spectral distribution. It is for this reason that ultrafast laser sources with broad spectra are utilized for the generation of THz pulses. Thus, a basic analysis of sum and difference frequency generation can be done by assuming the bounding laser input frequency components are the only field components impinging on a second order nonlinear crystal. The incident field is represented as,

$$E(t) = E_1 e^{-i\omega_1 t} + E_2 e^{-i\omega_2 t} + c.c \tag{3.12}$$

and taken as the input into the second order polarization contribution of the crystal,

$$P^{(2)}(t) = \varepsilon_0 \chi^{(2)} E(t)^2 \tag{3.13}$$

where the terms are expanded to yield

$$\begin{aligned} P^{(2)}(t) = \varepsilon_0\chi^{(2)}[E_1^2 e^{-2i\omega_1 t} + E_2^2 e^{-2i\omega_2 t} + 2E_1E_2e^{-i(\omega_1+\omega_2)t} \\ +2E_1E_2^* e^{-i(\omega_1-\omega_2)t} + c.c] + 2\varepsilon_0\chi^{(2)}[E_1E_1^* + E_2E_2^*] \end{aligned} \tag{3.14}$$

The relevant polarizations for difference frequency mixing, $P_{DF}(t)$, and optical rectification, $P_{OR}(t)$, are extracted from the fourth and last terms of the above expansion and written standalone as,

$$P_{DF}(t) = 2\varepsilon_0\chi^{(2)}E_1E_2^* e^{-i(\omega_1-\omega_2)t} + c.c \tag{3.15}$$

and

$$P_{OR} = 2\varepsilon_0\chi^{(2)}(E_1E_1^* + E_2E_2^*) \tag{3.16}$$

Unlike the other second order polarization contributions, optical rectification does not have an associated frequency term. This means that a static polarization is being created within the nonlinear crystal. The amplitude of this polarization is proportional to the electric field intensity. The explains the discussed offset of figure 3.1 (d) in the anharmonic nonlinear polarization response of a medium.

Optical rectification in the context of THz generation

Now, in terms of a more complete picture, an incident pulse E(t) with a pulse duration of 180 fs and centered at 1030 nm, in our case, is focused onto a GaP generation crystal. The input pulse is Gaussian and can be represented as,

$$E_t = E_0 e^{-at^2} e^{i\omega t} \tag{3.17}$$

where E_0 is a scalar field amplitude, a scales the pulse duration, ω is a radial frequency, and t is time. GaP is a non-centrosymmetric crystal that does have a second order electric

susceptibility. Focusing the laser field onto the crystal and fine tuning its angular position maximizes the susceptibility, which is a tensor field, and input field strength, thereby maximizing the efficiency of second order nonlinear processes. Unlike the conceptual case of optical rectification facilitated by monotone frequency field components with static field amplitudes, we must consider the time-dependence of the Gaussian input pulse. Within the crystal, difference frequency mixing between the broad spectral components of the ultrafast pulse will generate frequency components in the far to mid infrared region. Since the frequency components of the input pulse are significantly higher than the generated frequency components, the difference frequency mixing effect in the context of THz can be well approximated by the optical rectification effect [71]. Consequently, since the temporal duration of the input pulse into the crystal is much longer than its optical period of oscillation, the nonlinear polarization generated by the optical rectification effect follows the pulse envelope and is proportional to the square of the input field [69]. This interaction is depicted in figure 3.4, where the polarization as a function of time due to optical rectification is shown. This time varying polarization acts as a driving source for the aforementioned nonlinear wave equation and results in a generation of THz radiation. The spectral distribution of the THz is bounded by all permutations of frequency mixing within the components of the laser input field.

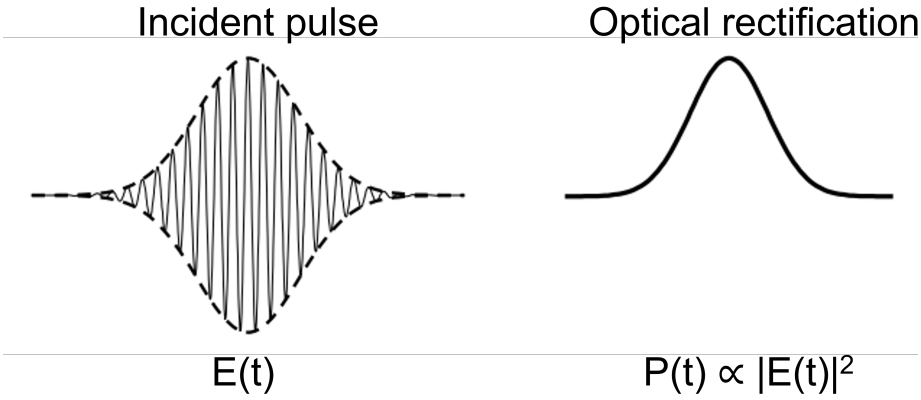

Figure 3.4: A schematic of optical rectification. An incident electric field onto a second order crystal is represented with a Gaussian envelope on the left. The effect of optical rectification in the crystal is proportional to the magnitude of the incident field intensity. On the right, optical rectification of the incident field is shown to produce a time varying polarization trace of its envelope. This time varying polarization drives the generation of THz radiation. Adapted from [69].

Phase matching condition in nonlinear crystals

As briefly mentioned before, maximizing the THz generation in a nonlinear crystal in terms of both field strength and bandwidth is highly dependent on orientation, thickness, diffraction, laser damage threshold, and what is known as the phase matching condition. For a zincblende crystal, like GaP, in the point class of $\bar{4}$3m, the nonlinear polarization field that generates THz depends on the orientation of the crystal [69]. Assuming an arbitrary electric field given by,

$$E = \begin{pmatrix} E_x \\ E_y \\ E_z \end{pmatrix} = E_0 \begin{pmatrix} sin(\theta)cos(\phi) \\ sin(\theta)sin(\phi) \\ cos(\theta) \end{pmatrix} \tag{3.18}$$

the polarization of a zincblende crystal can be calculated following [69] as,

$$P_{NL} = 2\varepsilon_0 \chi^{(2)} E_0^2 sin(\theta) \begin{pmatrix} cos(\theta)sin(\phi) \\ cos(\theta)cos(\phi) \\ sin(\theta)sin(\phi)cos(\phi) \end{pmatrix} \tag{3.19}$$

where the polar angle θ and azimuthal angle ϕ are defined relative to the electric field orientation and depicted schematically in figure 3.5. Remembering that the THz intensity is proportional to the square of the nonlinear polarization in the crystal, we can calculate

$$I_{THz}(\theta, \phi) \propto \varepsilon_0^2 (\chi^{(2)})^2 E_0^4 sin^2(\theta)[4cos^2(\theta) + sin^2(\theta)sin^2(2\phi)] \tag{3.20}$$

Finally, since the generated THz is parallel to the nonlinear polarization in the crystal, the THz intensity can be calculated to be maximized when the polarization field is in the [110] plane, with $\phi = \frac{\pi}{4}$ and $\theta = 0$ [69].

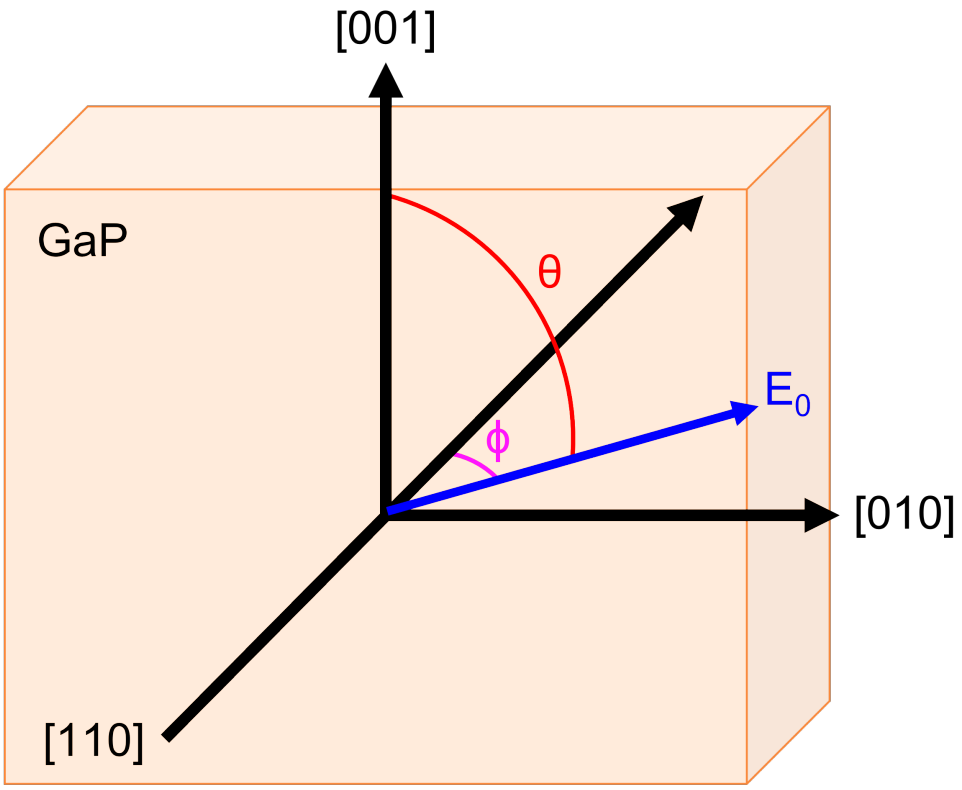

Figure 3.5: GaP crystal orientation relative to an incident electric field given in spherical coordinates. The crystal is shown relative to planes defined by the Miller indices of [001], [010], and [110].

Once the orientation of the incident laser field onto the generation crystal is optimized, the efficiency of generated THz will then mainly depend on a defined coherence length in the crystal. In the ideal case, the generated THz in the crystal propagates at the same velocity as the near-infrared (NIR) input laser field, $v_{THz} = v_{NIR}$. In this case, the generated THz will be gradually increased in amplitude as it travels the length of the nonlinear crystal, in a constructive manner. But this condition is very difficult to achieve in practice since the crystal requires a refractive index match as well, of $n_{THz} = n_{NIR}$, which is unlikely to be the case. Instead, it can be shown that when the NIR input is faster than the generated THz

wave, $v_{NIR} > v_{THz}$, an optical coherence length, L_{coh}, can be defined as [69, 68],

$$L_{coh} = \frac{c\tau_p}{n_{THz} - n_{NIR}} \tag{3.21}$$

where τ_p is the NIR pulse duration. As the thickness of a nonlinear crystal is increased past the coherence length, the generated THz will become out of phase with the driving second order polarization in the medium. Therefore, the THz radiation will continuously destructively interfere while travelling through the crystal and tend towards zero. This can also be understand as power from the THz wave reverse flowing into the frequency mixing waves [68]. Therefore, utilizing a nonlinear crystal with a long coherence length and ensuring that the crystal thickness is smaller than the coherence length is essential for optimal THz generation. This applies to the generated spectral bandwidth of THz as well. In general, while still below the coherence length, thicker crystals can achieve a larger intensity of generated THz but a smaller bandwidth and thinner crystals can generate a larger bandwidth but at a lower intensity.

Finally, it is important to note that nonlinear optical crystals have dispersion at both NIR and THz wavelengths. Since the refractive index in a dispersive medium varies with frequency, the group and phase velocity of a pulse also differ, respectively with

$$V_g(\omega) = \frac{\partial\omega}{\partial k} \tag{3.22}$$

and

$$V_p(\omega) = \frac{\omega}{k} \tag{3.23}$$

where $k(\omega) = n(\omega)\frac{\omega}{c}$. A well known phase matching condition for THz generation in a dispersive medium requires the NIR group velocity to travel at the phase velocity of THz [72]. In this case, the envelope of the NIR input field matches the phase of the generated

THz. For a broadband THz pulse generated in a dispersive medium, the phase matching condition requires the NIR group velocity to match the phase velocity of the central THz spectral component [69]. The coherence length in the dispersive regime is given by,

$$L_{coh} = \frac{c\tau_p}{(n_g - n_{THz})} \tag{3.24}$$

where n_g is the group index of the NIR input field.

3.1.2 THz detection through electro-optic sampling

Detection of the THz electric field in both amplitude and phase is not accomplished by directly detecting THz pulses. Rather, the THz pulse is convoluted with a NIR probe pulse in another nonlinear crystal and the THz-induced change on the crystal is monitored using a NIR detector. This convolution is done through an electro-optic sampling scheme utilizing the second order Pockels effect. This effect can be seen as the inverse of optical rectification when the nonlinear medium is dispersionless. The Pockels effect describes how a static electric field on a crystal can induce birefringence in the medium [68]. In comparison to NIR frequencies, THz frequencies are much smaller, relatively, and can be approximated as being DC. The generated birefringence of a NIR and THz pulse incident on a second order nonlinear crystal, GaP in our case, is given by

$$P(\omega) = 2\varepsilon_0 \chi^{(2)} E_{NIR}(w) E_{THz}(0) \tag{3.25}$$

Thus, electro-optic (EO) sampling is achieved as a detection scheme by focusing THz onto the detection crystal along with a NIR probe pulse. The probe pulse will experience a birefringence that is proportional to the THz electric field amplitude, which it experiences as static. The THz amplitude can be detected using a balanced detection scheme shown in

figure 3.6.

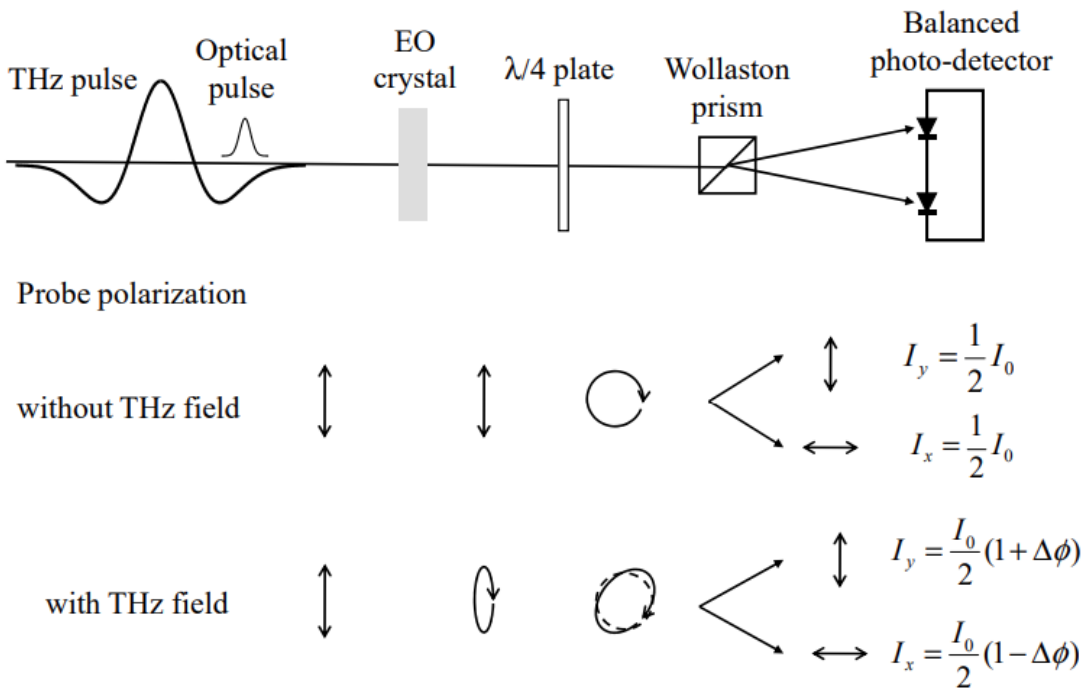

Figure 3.6: Schematic of EO sampling and the polarization optics utilized to detect the amplitude of a THz pulse. A NIR probe is spatially overlapped with THz in an EO crystal. THz is approximately experienced by a NIR pulse as a static electric field, which induces birefringence in the crystal. The linear input polarization of the NIR probe is then slightly modified and detected using balanced photodetectors to measure ellipticity in polarization. The polarization change is quantified by measuring the intensity difference of the detectors and is proportional to the THz amplitude. Adapted from [69].

Following the spatial overlap of the NIR probe and THz pulse in the EO crystal, the probe, which is initially linearly polarized, experiences a change in polarization due to the quasi-static THz amplitude. The probe is then passed through a quarter waveplate where the small polarization change induced by the THz results in a slightly elliptically polarized output. The elliptically polarized NIR field is then passed through a Wollaston prism and into two balanced photodetectors. The detection scheme measures the intensity difference between the orthogonal components of the probe pulse after the Wollaston prism. The

intensity difference is proportional to the THz field amplitude. In the case where there is no THz incident on the EO crystal, the NIR probe pulse maintains a linear polarization after passing through the crystal, becomes circularly polarized after the quarter waveplate, and the Wollaston prism splits its orthogonal components equally onto the balanced photodetectors. The intensity difference in this circumstance will be zero, corresponding to having no THz amplitude.

Finally, to extract the complete phase profile of the generated THz pulse, we make use of the temporal duration of the probe. The THz pulse does vary as a function of time, with a pulse duration in the picosecond range. The THz is described as quasi-static in amplitude because the NIR probe pulse duration lies in the femtosecond range. Therefore, when the THz and NIR probe are spatially overlapped in the EO crystal, the probe does not experience the amplitude variation of the THz, allowing the THz to effectively be treated as a static electric field in the crystal. Instead, to measure the amplitude variation of the THz pulse as a function of time, the temporal delay between the THz and NIR probe is scanned using an optical delay stage. The result of this scanning is depicted in figure 3.7. An experimental measurement of a THz transient is shown in black, with the individual datapoints shown as red dots. Each one of these points represents a measurement of the THz amplitude at a given NIR pulse temporal position. A NIR pulse train is schematically depicted above the plot to indicate the time of convolution in the EO crystal. Since the polarization change in the NIR probe is a function of THz field amplitude, it is straightforward that the peak intensity difference occurs when the NIR probe is temporally overlapped with the peak of the THz pulse at $t = 0$. The resolution of the THz time-domain scan is determined by the step-size of the delay stage utilized to temporally scan the NIR probe pulse.

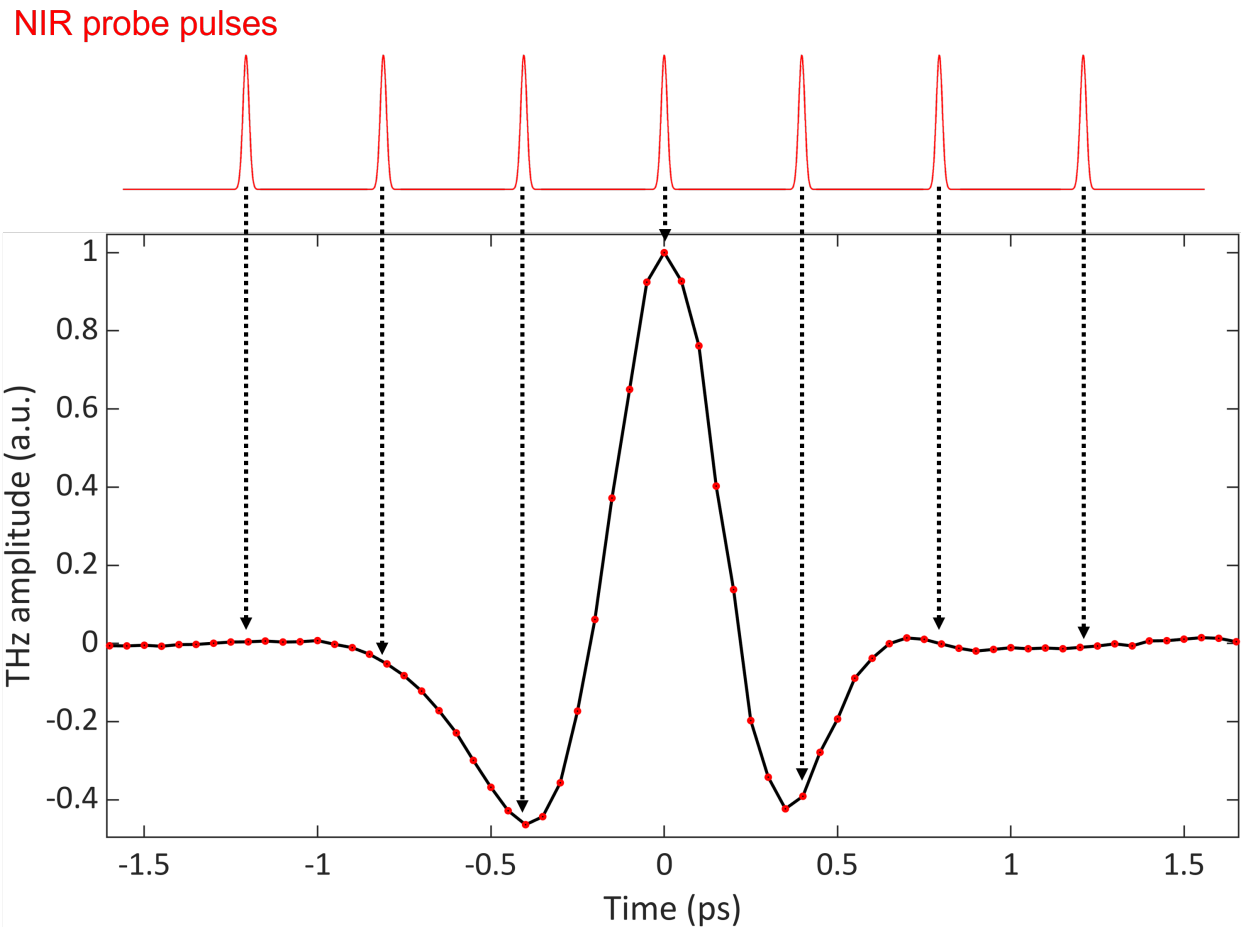

Figure 3.7: A THz transient (black) is plotted along with individual datapoints corresponding to the detected THz amplitudes (red dots). Each datapoint corresponds to a convolution between the NIR probe and THz amplitude in the EO crystal. Since the arrival time of the THz pulse onto the EO crystal remains constant, the temporal delay of the NIR probe can be temporally scanned to measure the THz amplitude as a function of time. A train of NIR pulses are schematically represented (red) interacting with the THz pulse at various temporal positions.

3.1.3 THz experimental setup

The methods of using optical rectification and EO sampling to generate and detect THz are implemented in practice using the experimental schematic depicted in figure 3.8.

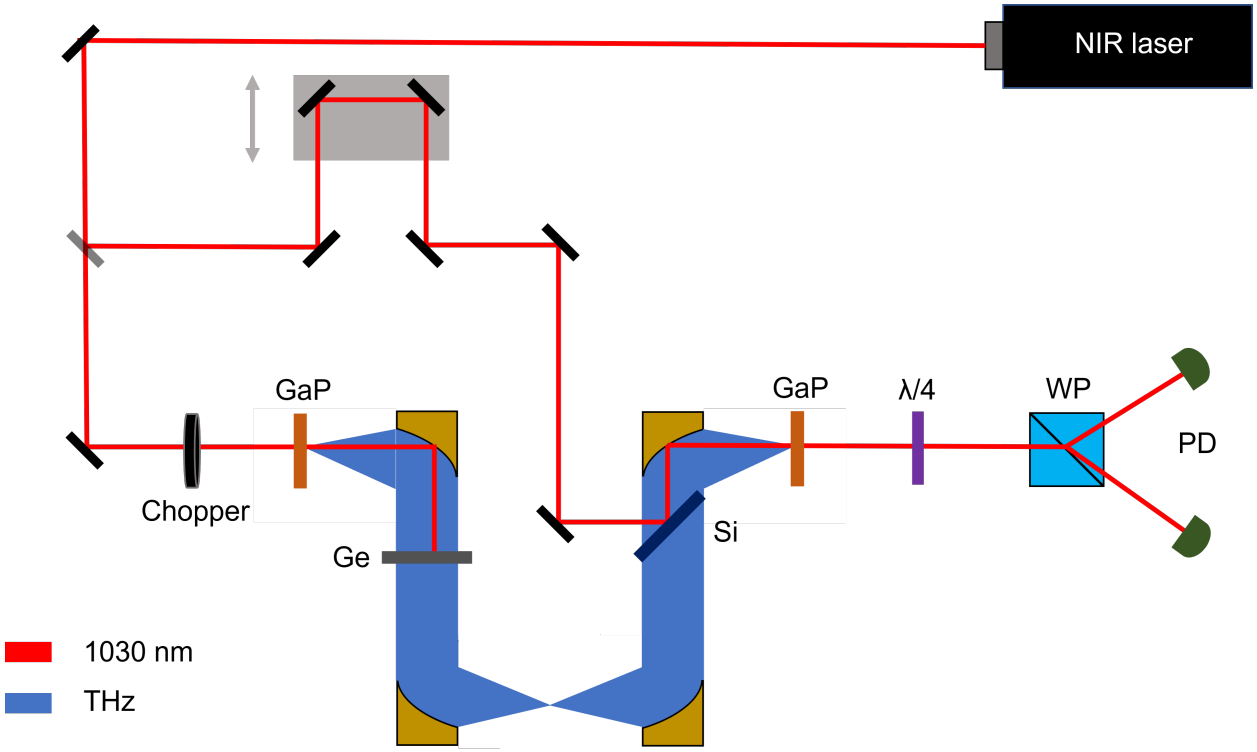

Figure 3.8: Schematic of our experimental THz-TDS setup. A 1030 nm ultrafast source is split into a THz generation path and a NIR probe gating path. The generation path produces THz based on optical rectification in GaP, focuses the THz for interaction with spectroscopy sample, and then focuses the resultant THz onto another GaP crystal for EO sampling. The gating pathway enables a temporally delayed NIR probe, using a two-mirror delay stage, to interact with the EO sampling crystal and the successive polarization optics for detection.

In this scheme, we utilize a Yb:KGW ultrafast laser source, "NIR laser", that produces 180 fs pulses centered at 1030 nm. The pulse energy of the laser is electronically tunable with repetition rates varying from 1 kHz to 1 MHz in frequency. The average power of the source is variable up to 6 W. For the metasurface optical tunability experiments discussed in this thesis, the laser source is operated at a 6-10 kHz repetition rate with an average power of 3-6 W.

The laser output into the THz setup is then split into a THz generation line and the NIR probe used for detection, designated as the gating line. The generation line is focused

into a GaP crystal to produce THz through optical rectification. As mentioned previously, the orientation of the crystal is optimized for maximum THz generation and the thickness is selected based on the desired spectral broadness of the THz, usually between 0-6 THz. Generated THz diverges outwards from the crystal and is collimated by a the first parabolic mirror after the crystal. A germanium (Ge) wafer is placed in the first collimated region to reflect the NIR pulses that transmit through the crystal while passing the generated THz pulses. The second parabolic mirror brings the THz to a 0.5-1 mm focus, at which samples for experiments are typically placed, and the third parabolic mirror recollimates the THz after the focus. Finally, the THz passes through a silicon (Si) wafer and is focused by the fourth parabolic mirror onto a second GaP crystal to generate a quasi-static field through the Pockels effect.

The gating line of the setup has the NIR probe pulses travelling along a two-mirror delay stage, depicted in gray. The NIR probe is then reflected off of the Si wafer and fourth parabolic mirror in the setup to spatially overlap with the THz in the second GaP crystal. The purpose of the delay stage is for the temporal control of the NIR probe relative to the generated THz pulse. As described in the EO sampling process, the NIR probe is temporally shifted over picosecond time durations in order to monitor the change in THz amplitude overtime and reconstruct the THz pulse field in detection. The time step size of the monitored THz field is determined by the positional step size of the delay stage. After the EO crystal, the NIR probe interacts with the aforementioned polarization detection optics and balanced photodetectors. The balanced photodetection scheme is aided by a lock-in amplifier detection process with an optical chopper placed in the generation line. Finally, the entire THz setup is enclosed by plexiglass box and purged with dry air. This is done because of the very high absorption of THz by humid air.

3.1.4 Time windowing and spectral analysis

As explained, the full electric field amplitude and phase of single cycle THz pulses are monitored through EO sampling; a process in which the position of a THz pulse is temporally static and a NIR probe is temporally scanned to gradually monitor the THz amplitude. The time duration of a THz scan is fundamentally limited by the positional step size and maximum displacement of the delay stage. The time window that bounds the scan duration is selected to ideally not include the first back reflection of the THz probe. This is a reflection occurring at the back surface of a crystal which is then reflected back again at the front surface of a sample, eventually being detected (time domain analogue of the Fabry-Perot). Most commonly, the first back reflection will be generated in a spectroscopy sample or from the THz generation crystal. Figure 3.9 shows a THz scan in air (no sample) long enough to capture the first back reflection produced by the generation crystal.

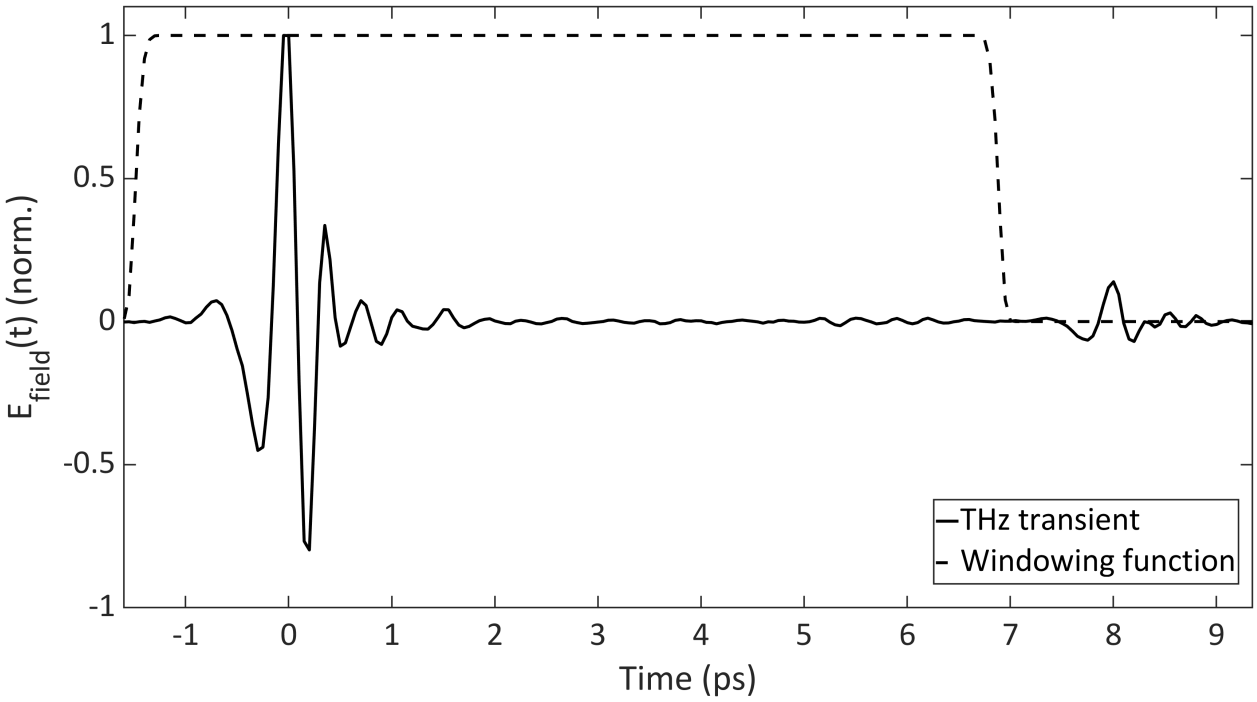

Figure 3.9: Example of a THz scan with a back reflection present (solid line). A windowing function to smoothly cut out the back reflection for the purpose of Fourier transformation is applied (dashed lines).

An important aspect of a spectroscopy technique is the analysis of the spectral response of a sample. In THz-TDS, this is achieved with a Fourier transformation of the time-domain transients. The presence of back reflections in a time-domain scan will result in Fabry-Perot interference features in the frequency-domain, which can hinder and obscure a sample analysis. In the experimental example shown in the plot, the first back reflection appears well after the main THz peak. In this case, we can remove this peak by either adjusting the scan duration of the delay stage to avoid scanning the back reflection or we can apply a windowing function in the data analysis. But, it is not ideal to remove the back reflections from the time-domain data by zeroing them because the resultant Fourier transform will contain false harmonics cause by the artificially introduced sharpness. Instead we apply exponentially decaying functions around the main THz transient to smoothly cut out back reflections from the data. In the plot, an example of a windowing function is depicted by the dashed lines. This particular function is given by,

$$f_{window}(t) = exp[-\frac{(t-t_{min})^6 - (t-t_{max})^6}{w^6}] \tag{3.26}$$

where t_{min} and t_{max} bound the windowing region and w determines the sharpness of the cut-offs. Additionally, in some cases, particularly in the spectroscopy of thin samples with low refractive indices, the first back reflection can appear within the pulse duration of the main THz pulse. In a case like this, we typically incorporate a thick THz transparent substrate on the sample to artificially increase the time before the first back reflection appears, allowing for a windowing function to be applied.

As mentioned, the transformation of the time-domain data into the frequency-domain is done utilizing a Fourier transform defined as

$$E(\omega) = \frac{1}{\sqrt{2\pi}} \int_{-\infty}^{\infty} E(t) e^{-i\omega t} dt \tag{3.27}$$

In practice, this is applied during data analysis utilizing a discrete fast Fourier transform (FFT) with added apodization. The Fourier transform of the windowed time-domain transient of figure 3.9 is shown in figure 3.10.

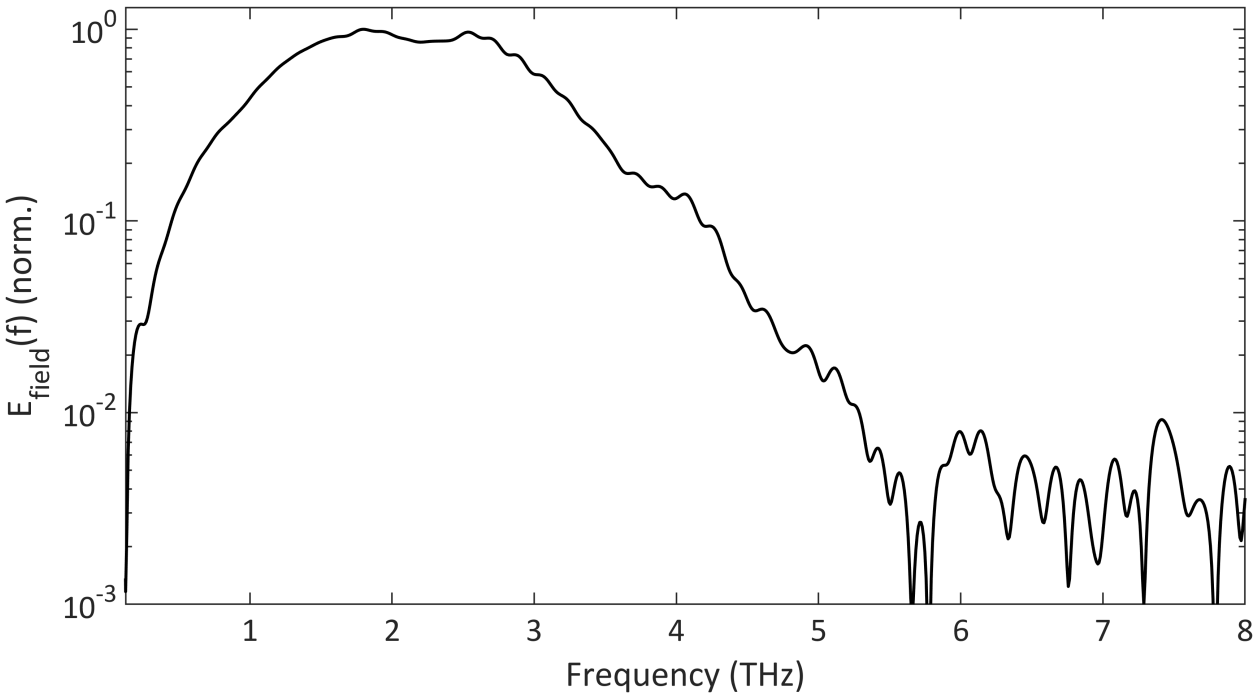

Figure 3.10: An example Fourier transform of an experimentally acquired THz scan. The plot is shown in the log scale to demonstrate the usable THz bandwidth before the noise floor.

In this frequency-domain plot, we show a THz spectrum in the log scale to highlight a typical bandwidth. The reliable bandwidth of a spectrum is selected based on the amplitude of the noise level, which appears after 5 THz in this spectrum. A broad THz bandwidth is experimentally achieved by utilizing thin generation and detection crystals, a 200 µm thickness in this case.

3.1.5 Analysis of resonances in the time-domain

While the analysis of resonators will be investigated in much more detail in Chapter 4, here we will introduce an example of THz-TDS on a resonating sample. We prepare two

samples for analysis: one sample of solid-state glucose in a powder form, enclosed by layers of a transparent polymer substrate, and one reference sample of layered polymer substrates without glucose. A time-domain, post windowing, plot of sample scans is presented in figure 3.11. The black curve represents the reference sample and the red curve represents the glucose sample. The presence of glucose is characterized by a resonance at 1.4 THz and a strong absorption at higher frequencies [73]. In the time-domain, this absorption can be seen by the low peak amplitude of the glucose scan compared to the reference. The resonance is identified by the ringing oscillations that proceed the peak amplitude and gradually decay over 6 ps. For the analysis of resonances, the frequency domain is essential for a complete picture, shown in figure 3.12.

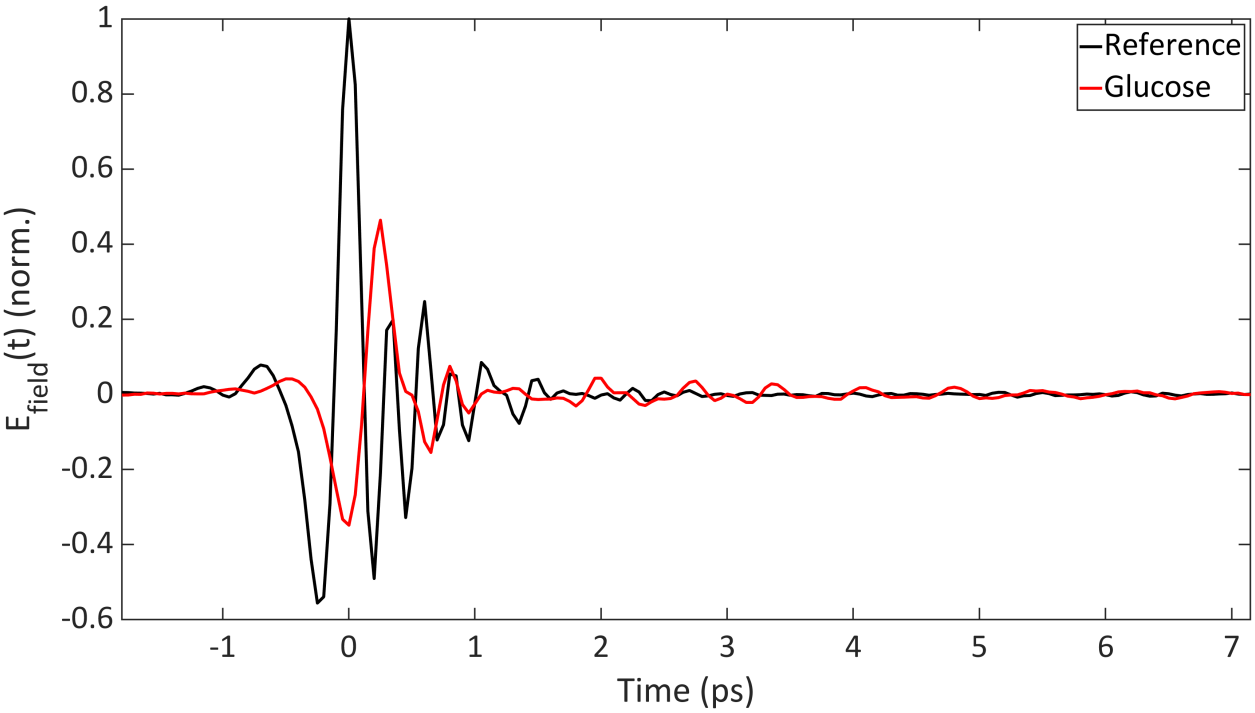

Figure 3.11: Plot of the THz time-domain response of glucose (red) compared to a reference empty sample holder (black). A windowing function has been applied to this data.

Looking at the Fourier transform directly reveals the distinct glucose resonance around 1.44 THz and the strong absorption loss that follows. Having a reference scan is useful in

THz-TDS to differentiate between spectral features that are present in the THz setup and features that are present because of the properties of the sample.

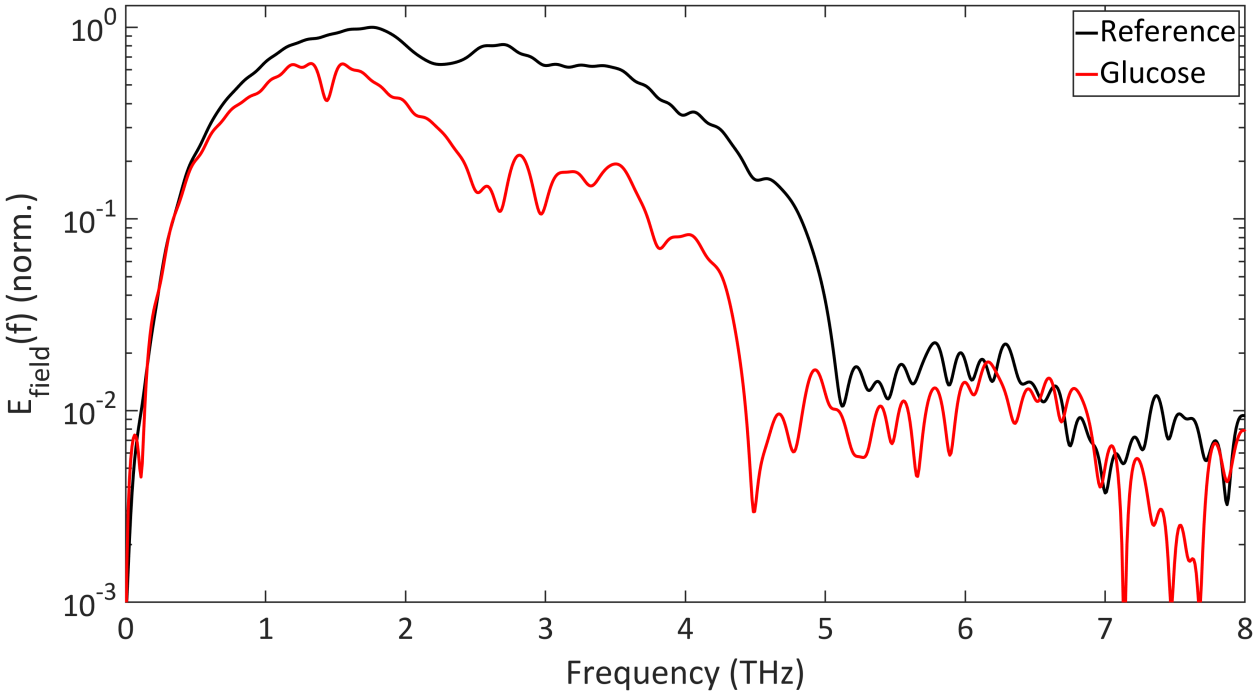

Figure 3.12: Plot of the THz spectral response of glucose (red) compared to a reference empty sample holder (black).

To make use of the reference in this thesis, we will directly show plots of the intensity transmission of THz scans proceeding time-domain plots. The intensity transmission is calculated after the Fourier transform is applied and given by,

$$T(\omega) = \frac{|E_{Sample}(\omega)|^2}{|E_{Reference}(\omega)|^2} \tag{3.28}$$

where $E_{Sample}(\omega)$ is the electric field spectrum of the measured sample and $E_{Reference}(\omega)$ is the electric field spectrum of a reference measurement, typically air or a substrate. In the case of this particular measurement, the sample field is the FFT result of the glucose scan and the reference is the FFT result of the reference scan. The transmission is plotted in figure 3.13. In the transmission plot, the resonance and subsequent THz absorption of

glucose at higher frequencies is now blatantly clear.

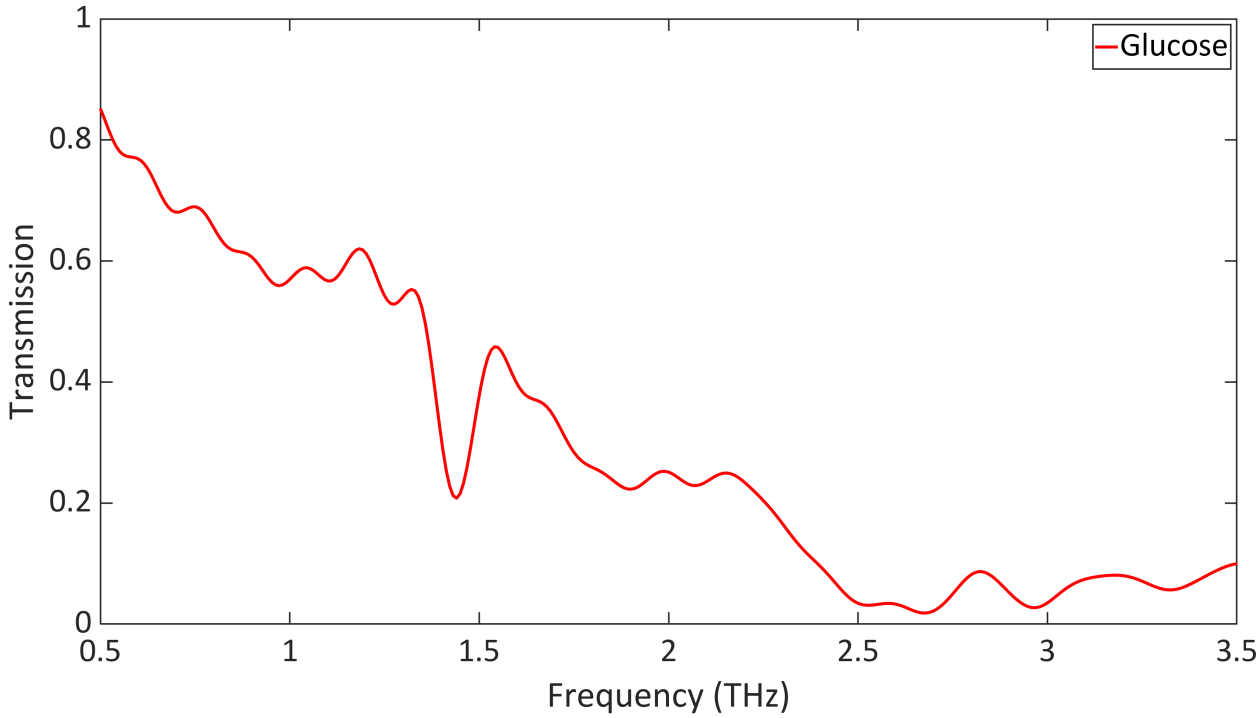

Figure 3.13: Plot of the THz intensity transmission of glucose

Finally, in the experimental results that are presented in this work, resonances will be analyzed utilizing curve fitting software and the assumption of Lorentzian-like line shapes. The curve fitting function utilized is given by,

$$f(\omega) = \frac{1}{\pi} \frac{\frac{1}{2}\Gamma}{(\omega - \omega_0)^2 + (\frac{1}{2}\Gamma)^2} \tag{3.29}$$

where Γ is the full width at half maximum (FWHM) of the resonance and ω_0 is the center frequency of the resonance.

3.2 Sample fabrication

The process of creating viable samples for THz metasurface characterization requires the fabrication of modelled/simulated plasmonic arrays onto characterized substrates with well known properties.

3.2.1 Metasurface fabrication

All plasmonic metasurface structures utilized in this work are fabricated using photolithography in combination with electron-beam evaporation. Once the plasmonic array is designed using a single element periodic FDTD simulation, in the process described in chapter 2, a corresponding photomask is created. The photomask defines the geometrical design of the entire array region, which is typically a 2.5 cm^2 area in this work. The photomask is then utilized with a photolithography process on a positive-tone resist to create the plasmonic array and structures. Finally, a metal, gold or silver, fills the array through electron-beam evaporation.

3.2.2 Role of the substrate

The selected substrate is critical to the performance of the metasurface. In many cases, complete material data is not readily available in the THz region. Therefore, THz-TDS is utilized in this thesis to first characterize the THz transmission of substrates, as will be shown in chapter 4. Once potential substrates are confirmed to have a high THz transmission and a low absorption in the bandwidth of interest, they are simulated with a plasmonic array design on a surface. The real part of the refractive index of a substrate directly determines the resonance frequency and resonance quality of a plasmonic structure. The interaction between the substrate and metasurface additionally causes a performance dependence on the imaginary part of the substrate index. Strong absorption loss in a substrate will rapidly

decay the plasmonic modes in the metasurface, limiting the peak performance of the design. The ideal substrate for a THz metasurface has a high THz transmission, a low refractive index/ Fresnel reflection coefficient, a low absorption, a high optical damage threshold, and a large heat resistance.

Chapter 4

Results and discussion

4.1 THz substrate and material characterization

4.1.1 Zeonor

Here we provide an example of an experimental substrate characterization in the THz. Zeonor (Also known as Zeonex) is a commercially available cyclo-olefin polymer that is known for having excellent mechanical properties, high transmittance in the visible and THz spectral regions, and a very frequency stable refractive index of 1.531 at THz frequencies [74]. Utilizing the spectroscopy techniques described in the previous chapter, the time-domain response of a 188 µm thick layer of zeonor is collected.

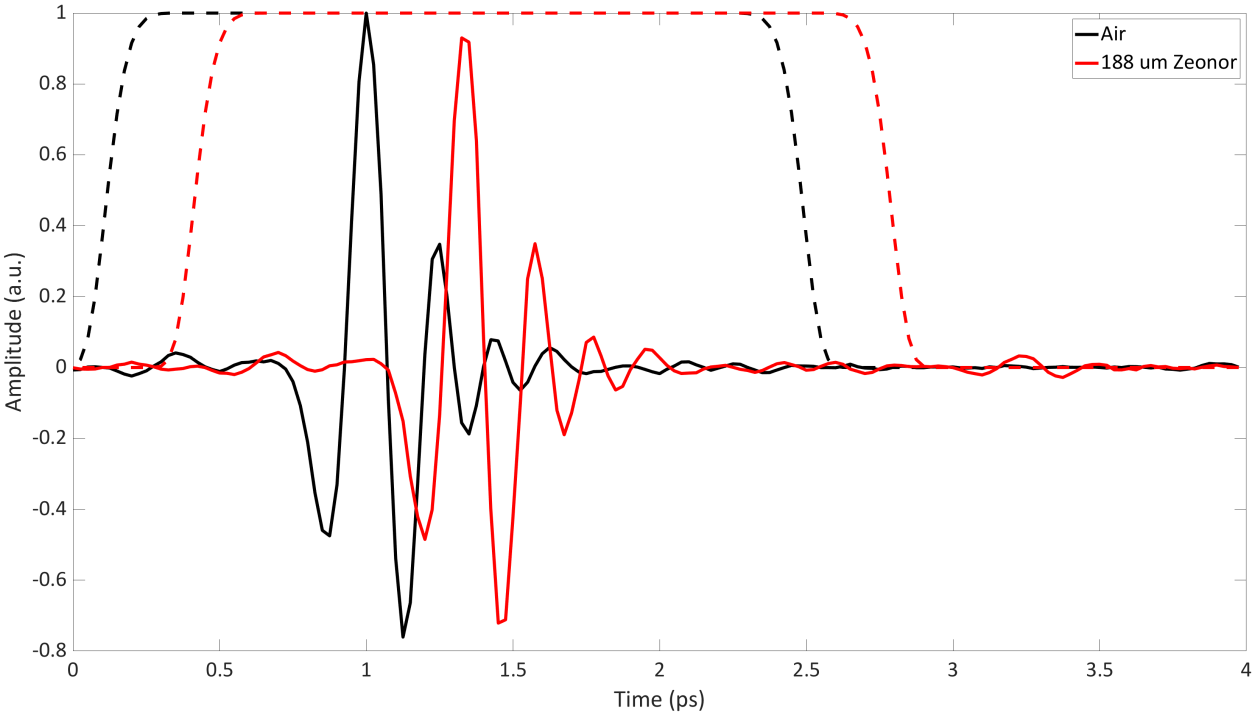

Figure 4.1: Time-domain THz transients of air (black) and a 188 µm thick zeonor sample (red) are shown with an amplitude normalization to air. The applied time-windowing functions, before zero-padding, are shown with dashed lines.

In figure 4.1, a plot of THz transients through air (no sample) and the zeonor sample are shown. The air transient is taken as a reference to this data and used for amplitude normalization. The total time duration of these transients is decided by the time it takes back reflections in the THz setup to arrive at the detection crystal. Furthermore, an equal time window is applied to both transients in order to cut out a back reflection from the zeonor sample itself. The first round trip travel time of THz in 188 µm zeonor can be calculated to occur after 1.92 ps, and can be seen in the plot arriving after the zeonor time window (red dashed line). After the zero-padding defined by the time-windowing functions is applied, the FFT of the transients can be taken in order to calculate the air referenced intensity transmission of zeonor.

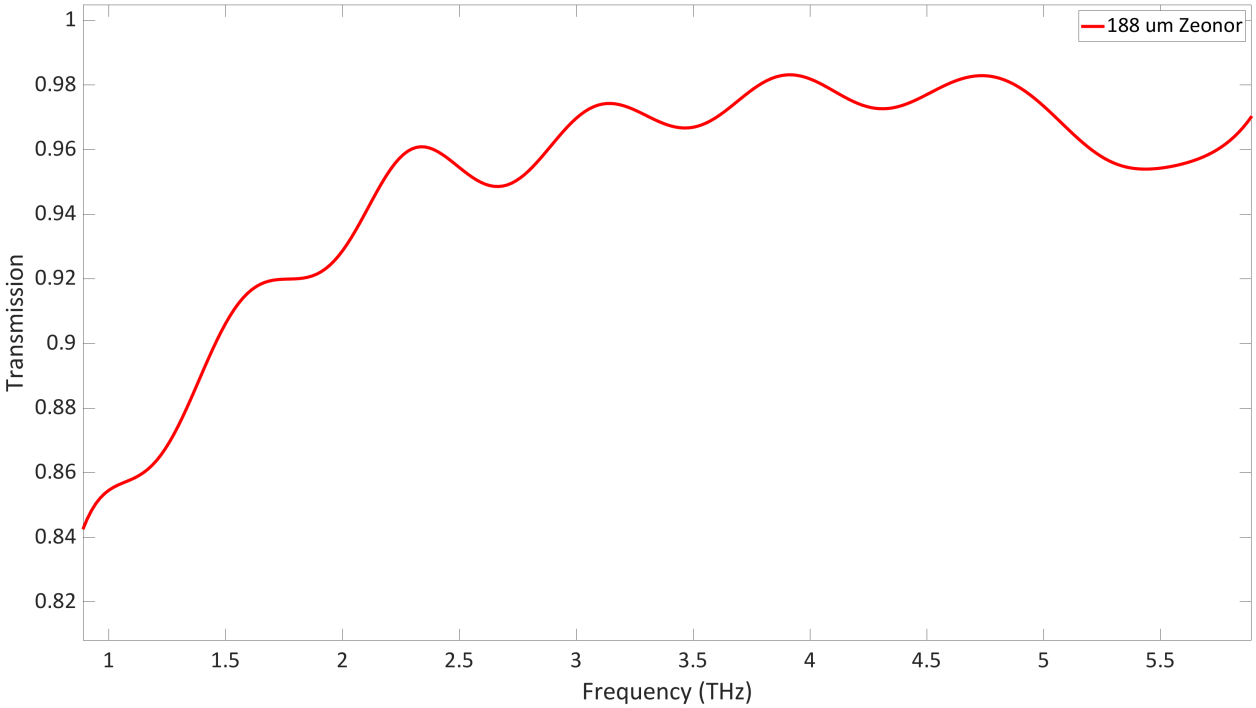

Figure 4.2: An air referenced intensity transmission of zeonor characterized in a broadband THz range

Figure 4.2 shows a plot of the broadband THz transmission through zeonor. Similar to commercial characterization in [74], transmission ramps from the lower THz frequencies to values of T $>$ 90%. The large THz transmission of zeonor, in combination with its versatile material properties, and tolerance of most clean-room solvents allows us to use it as a general substrate for many THz characterization applications.

4.1.2 Silicon

Silicon is an interesting material for many active THz devices. In the THz spectral region, silicon has a refractive index around 3.4 [54] and a transmission of around 60%, limited by the corresponding Fresnel reflection coefficient. Since silicon is a known indirect bandgap semiconductor material, typically used in photovoltaics, substrate thicknesses in the millimeter ranges are typically needed to obtain significant visible light absorption to photogenerate

carriers. A thick silicon substrate is very interesting to investigate using THz time-domain spectroscopy for two reasons: The large refractive index and thickness of silicon will result in a significant delay before the first back reflection of the probing THz pulse arrives at the detector; this makes isolating the probe to a single cycle pulse and windowing the time-domain data much simpler. Additionally, Silicon is opaque to visible wavelengths and has, for example, a 1/e absorption within 1 µm at 515 nm [75]. Using a 0.9 mm sample of float-zone silicon, we have explored the THz response in the time-domain.

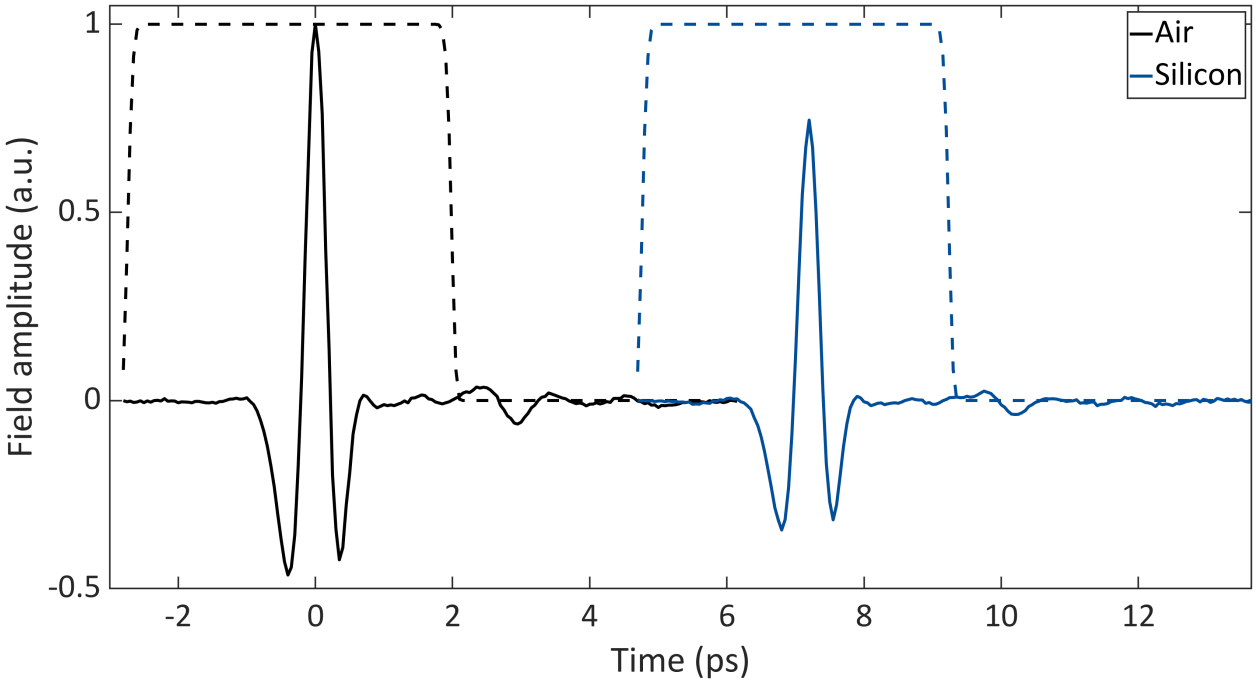

Figure 4.3: Time-domain transients through both silicon (blue) and air (black). The amplitudes are normalized to that of air. Windowing functions that are used on the transients are shown in dashed lines of the corresponding plot colour.

Figure 4.3 shows two THz transients, one through the silicon sample and one through air. The amplitude is normalized to the air reference peak and the windowing functions are again shown with dashed lines. Due to the aforementioned benefits of using silicon, we can immediately observe three stark differences between the previous zeonor sample and silicon. First, the silicon transient has a substantial 7.2 ps time delay from the reference

transient. Second, the silicon transient does not have any substrate back reflection in the full measurement range. There is an artifact that does appear outside of the defined windowing function, but this feature is present after the reference transient as well and indicates that it arises from a reflection in the setup. Finally, we can also see from the time-domain that THz transmitted through silicon experiences a significant decrease in amplitude.

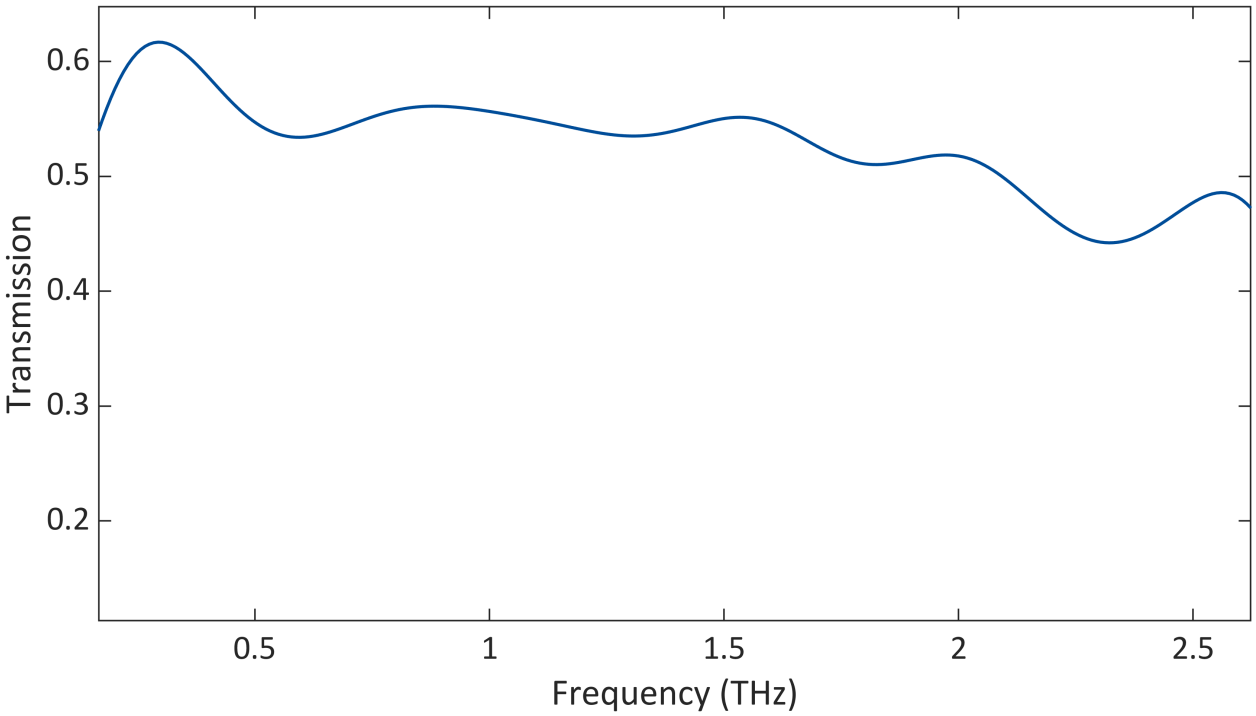

Figure 4.4: An air referenced intensity transmission of silicon

We can then look at the Fourier transformed intensity transmission in figure 4.4 to see a value within 50-60%, in agreement with commercial high resistivity float-zone silicon measurements [76]. The general takeaway from this characterization is that using silicon simplifies time-domain analysis. The substantial transmission delay through the sample results in the THz back reflections in silicon to arrive much after the useful measurement range in time and can effectively isolate a single-cycle response, at a cost of a lower transmission than zeonor.

4.2 Pump-probe measurements

We utilize two methods of pump-probe THz spectroscopy in which the ultrafast laser source used to generate THz which impinges on the sample. Since we are using an ultrafast pump source, we require careful spatial and temporal alignment. A modification to the previously shown THz setup is made to include a split-off ultrafast pump source, shown in figure 4.5.

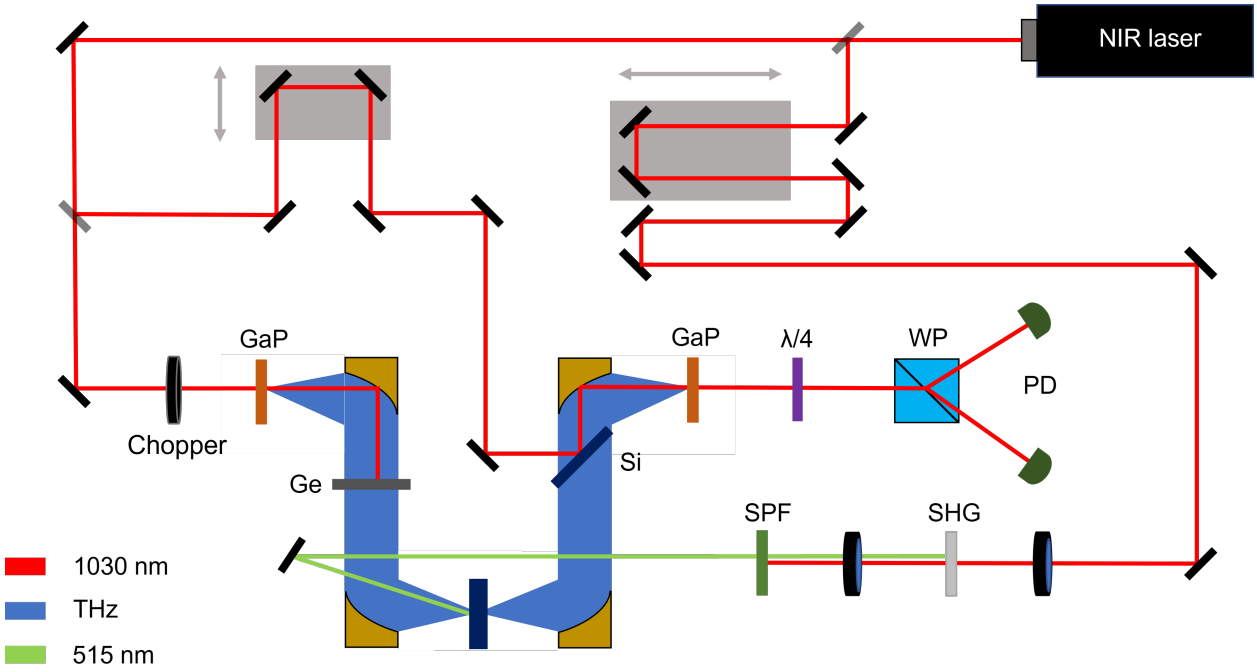

Figure 4.5: A modification to the THz setup schematic that allows for a 515 nm ultrafast pump that spatially and temporally overlaps with generated THz. A delay stage in addition to a second harmonic generating (SHG) crystal, and shortpass filter (SPF) enables this temporally overlapped split-off from the 1030 nm femtosecond source.

The 1030 nm ultrafast source used to generate THz is split-off into a pump-line. A delay stage and a series of mirrors are used to extend the pathlength of the pump line so that it falls within a similar pathlength to the THz generation line. A delay stage also allows us to achieve precise temporal control and time-domain pump monitoring around the region of optical pump - THz probe overlap. This specific setup modification is made to show the typical pump configuration we use for metasurface samples, converting the source wavelength

to 515 nm. A telescope is used to inject the ultrafast pump into a second harmonic generation (SHG) crystal and a shortpass filter (SPF) blocks any 1030 nm light from entering the THz setup. The ultrafast pump is focused onto the sample, typically at the THz focus. Spatial overlap is initially achieved using a pinhole at the THz focus and further optimized along with temporal overlap by using a silicon sample for calibration.

4.2.1 Optically-pumped plasmonic resonators on Si

In an investigation of ultrafast device tunability, there are three aspects to focus on. The function of an optically tunable THz device requires a response to a photoinjected carrier density that affects the device transmission in the THz. We first demonstrate optical tunability in silicon, as mentioned before, this is a material that has a clear response in the THz and is known to have a strong near-surface absorption of visible wavelengths. Using silicon as a substrate, we then pattern a metasurface plasmonic array with a notch filter response in the THz. Figure 4.6 a) shows a schematic of this structure and a visualization of incident THz and visible wavelength pulses.

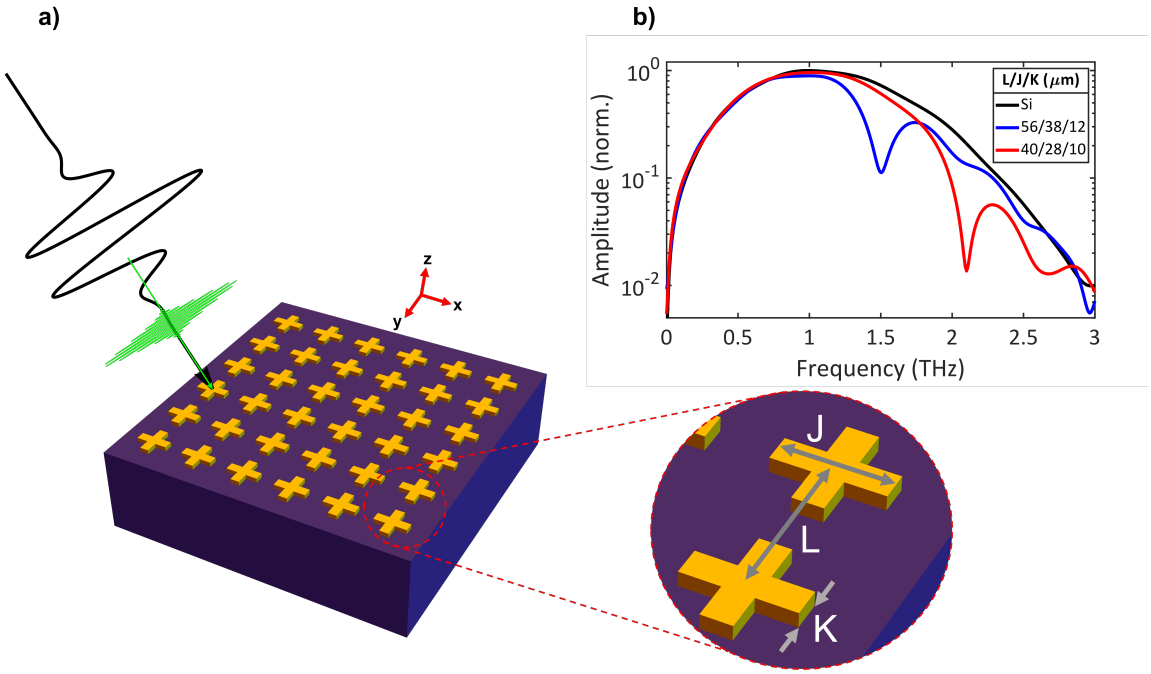

Figure 4.6: a) A schematic of a THz plasmonic resonator array on a silicon substrate. THz and visible wavelength pulses are incident on the device to depict the process of optical pump tunability. The geometry and periodicity of the cross array determines the THz resonance response b) A plot of the Fourier transformed time-domain response of a silicon reference and two filter arrays with different geometrical parameters [1].

The device consists of a float-zone silicon substrate of 0.9 mm thickness. The patterned array of gold crosses has a thickness of 200 nm with planar geometries of micron sizes. The gold crosses individually have a dipole-like response, with the main benefit of the cross geometry to achieve a symmetrical response to incident light. Depending on the array periodicity, cross arm length, and width, the THz resonance frequency, full width at half maximum (FWHM), and notch transmission can be precisely designed. Figure 4.6 b) is a plot of the Fourier transformed time-domain responses of a bare silicon reference and two filter devices with different geometries. The plots are normalized to the bare silicon reference. A microscope image of a cross array sample is presented in figure 4.7. Since the geometrical dimensions of these arrays are in the micron range to facilitate a THz response, we very clearly see how defect-free a fabrication can be compared to nanoscale dimension

metasurfaces for optical wavelengths.

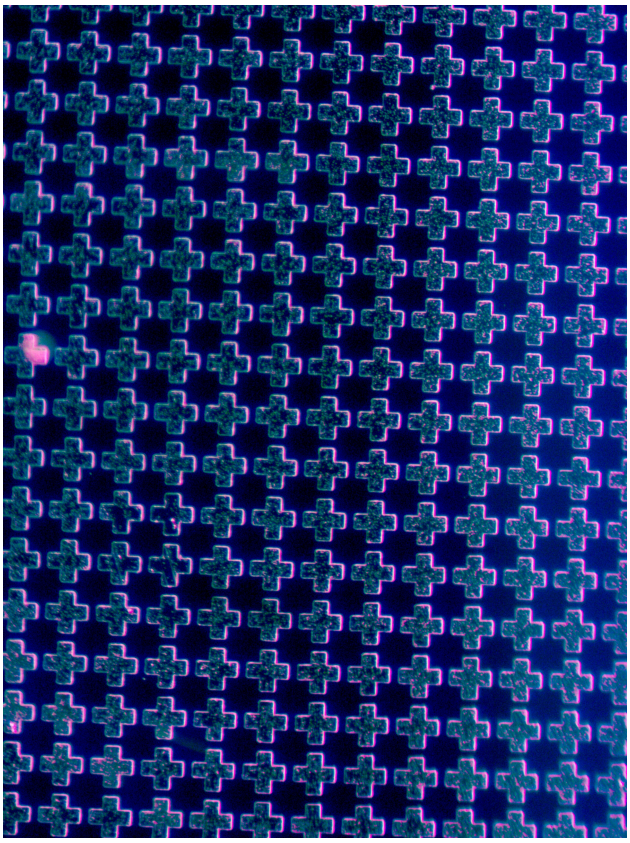

Figure 4.7: Microscope image of a gold cross plasmonic resonator on a silicon substrate

Optically-excited Si probed with THz

The goal of using silicon as a material for optical tunability on ultrafast timescales is to take advantage of the aforementioned long carrier recombination time. We can demonstrate the effect of these carrier dynamics by doing optical pump - THz probe on a bare silicon sample with the setup configuration in figure 4.5. By doing a time-domain spectroscopy on the carrier dynamics of a material, we are referring to observing the pump induced change of the THz response as a function of time. In chapter 3, the process of THz-TDS can be summarized in terms of monitoring different points of a picosecond THz electric field in femtosecond step sizes. To observe the pump induced change of a THz response, we are

instead monitoring a fixed point of the THz electric field, in this case the peak field value, while temporally moving the optical pump to and away from its overlap with the THz probe. This is accomplished by moving the pump delay stage in the THz setup while keeping the gating delay stage at the position of the peak THz field. A time-domain scan of the silicon carrier dynamics is plotted in figure 4.8.

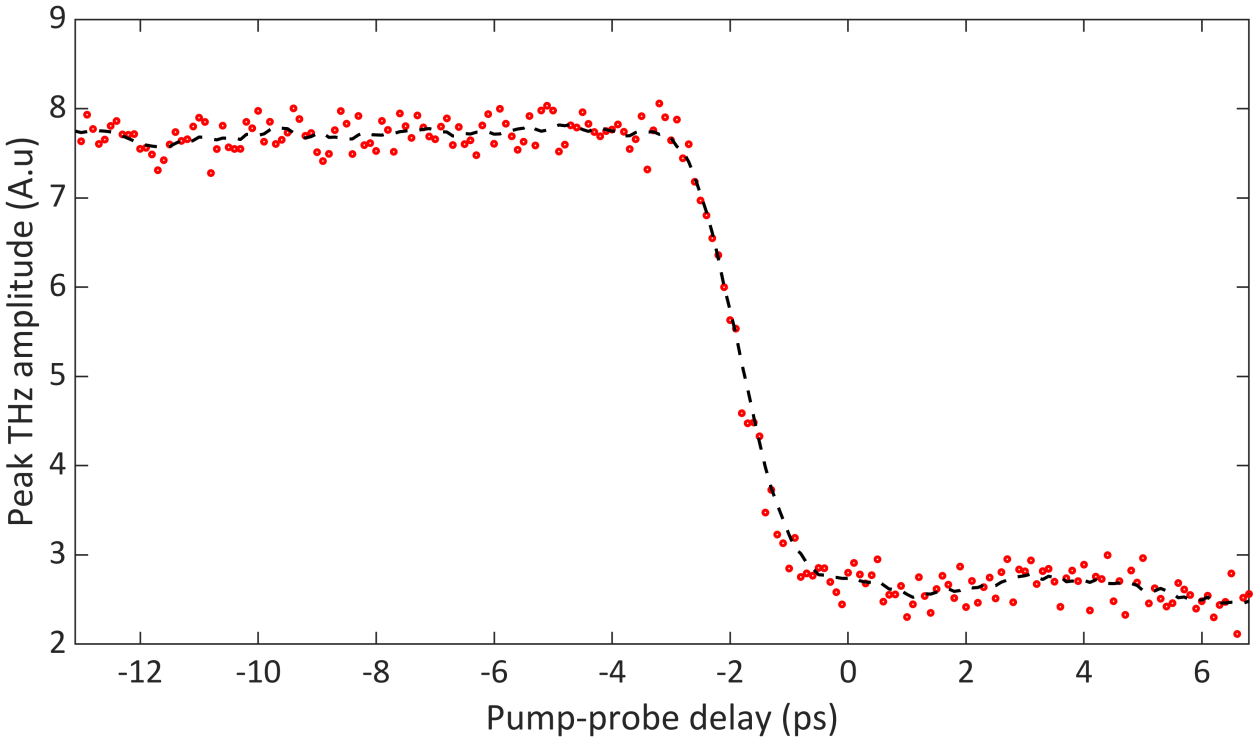

Figure 4.8: A time-domain scan of the carrier dynamics of silicon. The temporal delay between an optical pump and the fixed peak field (red dots) of a THz probe is varied over a range of 20 ps. Negative pump-probe delays are defined as the THz probe arriving before the pump and 0 ps is defined as the pump-probe overlap. A moving mean of 1 ps (black dashed lines) is plotted for visual clarity.

In this plot, the peak THz amplitude is shown to change in the presence of a 515 nm 180 femtosecond pulse with an intensity of 1.4 GW/cm^2. A pump-probe delay of 0 ps is defined as the temporal overlap between the optical pump and THz probe. Negative delays are defined as the THz probe arriving before the pump and positive delays are defined as the pump impinging upon the sample before the THz probe arrives. The pump delay stage

is scanned over a range of 20 ps with a step size of 100 fs; the corresponding data points are shown as red dots in the plot. The black dashed line is a plotted 1 ps moving mean of this data for visual clarity. In this case, the moving mean is defined by taking the mean value of a sliding window in a dataset [77]. Where the mean of a sliding window subvector within the larger dataset vector is defined as,

$$\mu = \frac{1}{N} \sum_{i=1}^{N} A_i \tag{4.1}$$

where A_i is the sliding window subvector and N is the length of the sliding window. Looking at the plot with this insight reveals the nature of the long carrier recombination time in silicon. Once the pump begins to temporally overlap with the THz probe and is in the regime of arrival before the probe, the peak THz field experiences a sharp exponential decay due to free carrier absorption. In terms of a single cycle picosecond THz pulse, the response of silicon to an optical pump effectively behaves in a step-like manner and the entire THz probe will experience a uniform absorption when transmitting through pumped silicon.

When measuring the carrier dynamics of silicon, a strong intensity pump is used to induce a large free carrier absorption in silicon and saturate the response. This is done to highlight the sharp exponential decay of the peak THz field at the pump-probe overlap. For practical applications in tunability, it is useful to characterize a gradually increasing pump intensity in silicon that does not saturate the THz transmission. To do so, we take standard THz-TDS scans of optically pumped silicon with various pump intensities, plotted in figure 4.9.

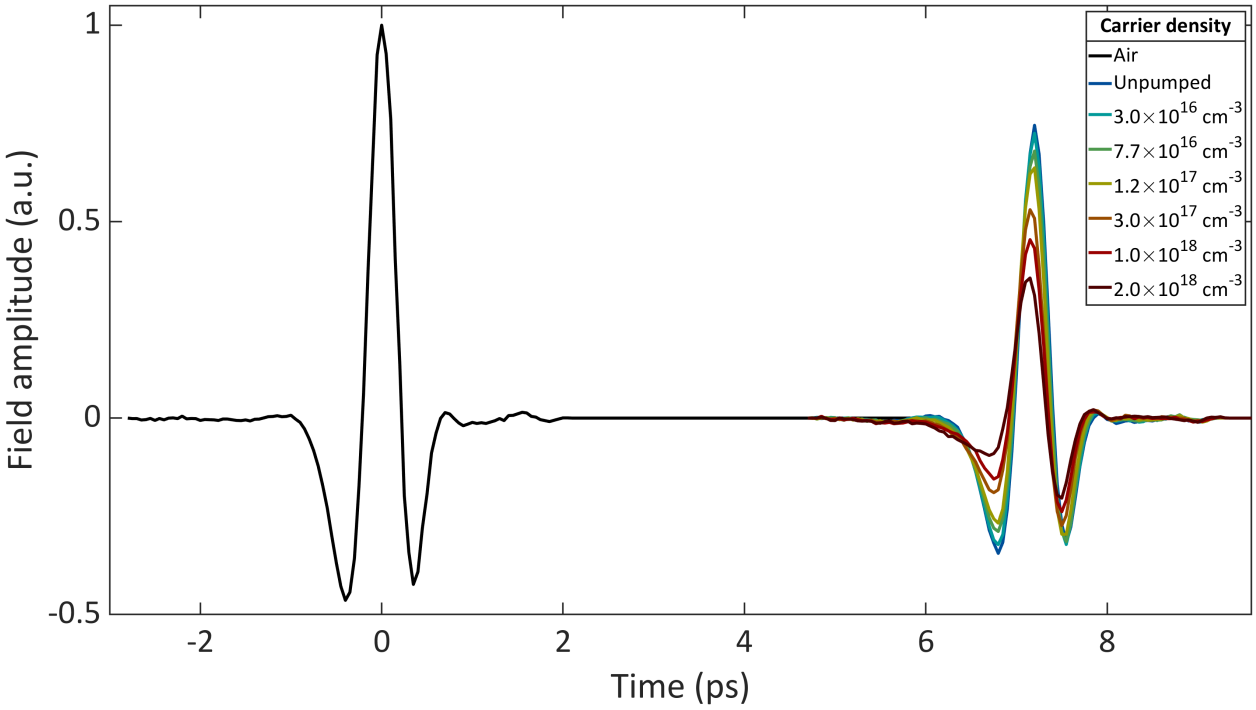

Figure 4.9: THz transients of air and silicon with different photoinjected carrier densities. A 515 nm ultrfast pump impinges on a silicon sample with different intensities. A carrier density value is extracted from FDTD simulations of a Drude silicon model.

Here we have time-domain scans of an air reference, unpumped silicon, and optically doped silicon. The optical doping of silicon is given in terms of a carrier density value; this value is determined through FDTD simulations of optically doped silicon using a drude model. The "unpumped" value can similarly be simulated by matching an intrinsic carrier density (n=1×10^{13} cm^{-3}) drude model to experimental results. The simulations are matched with experimental results for a pumped resonator on silicon device. In the next section, we will highlight why this approach makes for an easy modelling tool and why these particular optical doping concentrations are chosen for this experiment. In this experiment, the only parameter being changed in the experimental setup is the ultrafast pump attenuation achieved with ND filters. The generated THz intensity remains unchanged. From the silicon transients it can be seen how the first three doping concentrations gradually lower the THz field amplitude, while the n=3×10^{17} cm^{-3} transient and those that follow experience

a much stronger attenuation. This is even more obvious when looking at the corresponding transmissions in figure 4.10.

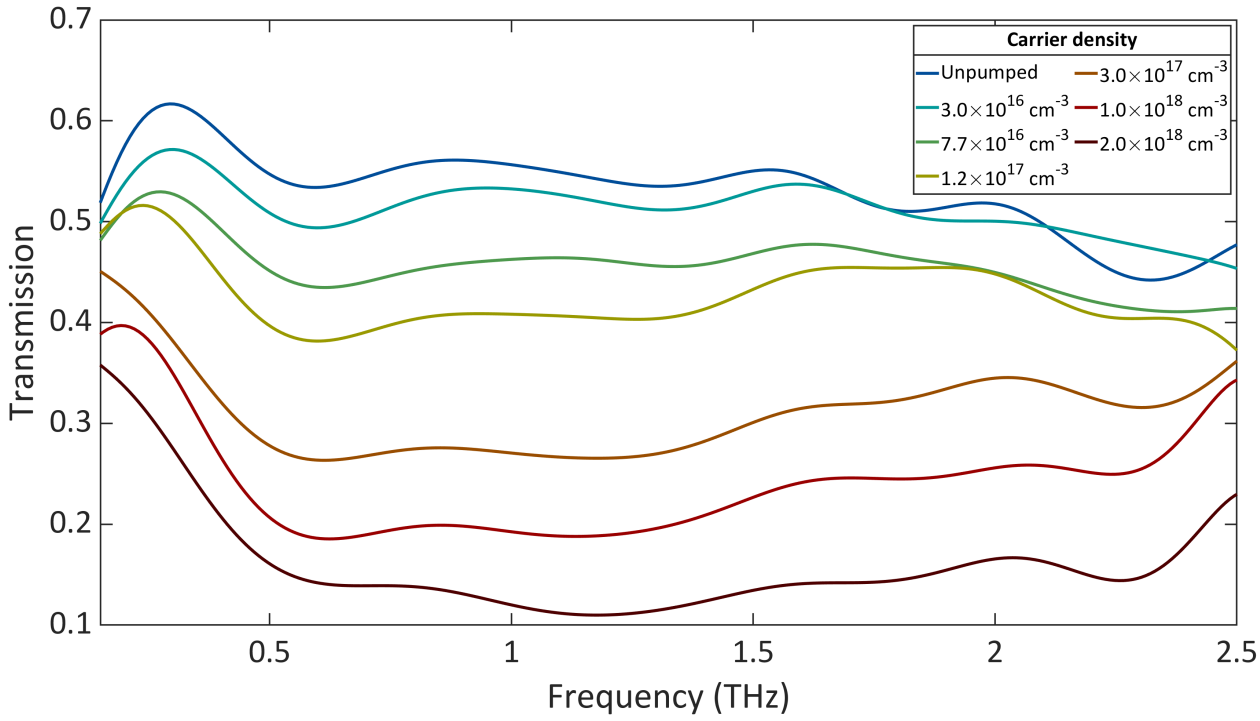

Figure 4.10: A plot of air referenced intensity transmission of optically doped silicon.

In the air referenced intensity transmissions of the pump silicon transients we can see the difference between the gradual and drastic attenuation. In the case of resonator optical tunability, we note that any photoinduced carrier density above n=3×10^{17} cm^{-3} put our silicon resonators in a regime of complete saturation. It is important to note that these optical doping concentrations were established by the pump pulse impinging on the silicon sample 100 ps before the THz probe arrived. Therefore, there is no significant carrier recombination at the time of the THz probe arrival.

Optically-excited THz plasmonic resonator on Si probed

A plasmonic resonantor with a notch spectral filter response is extremely useful for measuring pump-induced change in a sample. Resonances can be engineered to reach strong modulation

depths and Q factors, allowing them to become very sensitive to any losses, in our case, due to free-carrier absorption in the pumped substrate. Two methods of optical pumping are investigated, one regime, static pump-probe spectroscopy, is done by injecting an optical pump pulse well before the THz probe arrives. This static case is exactly what was presented in the previous silicon pump-probe measurements.

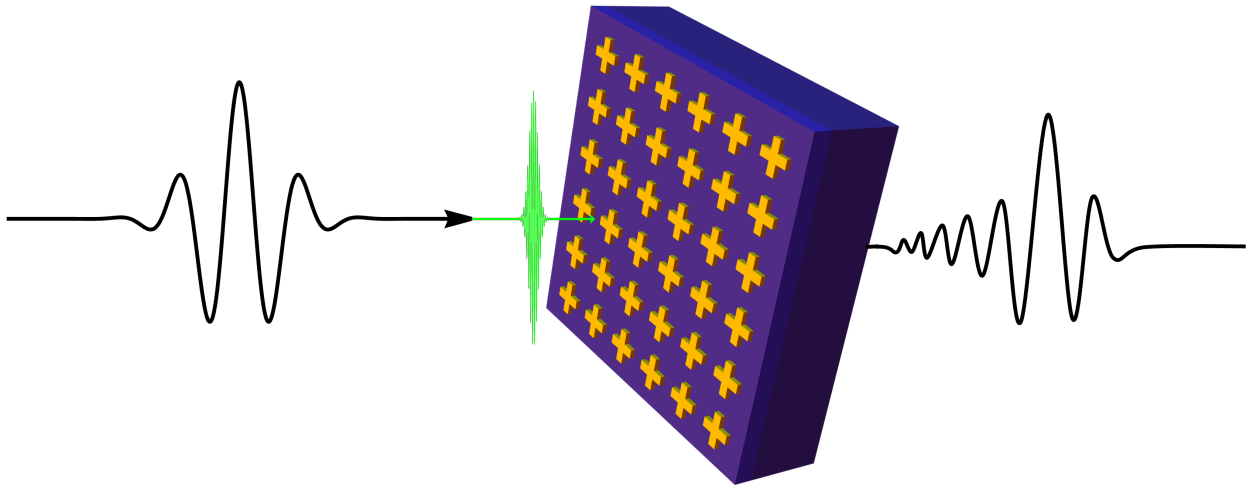

Figure 4.11: A schematic depicting a static pump-probe regime. An optical pump photoinduces carriers near the surface of a plasmonic filter 100 ps before the arrival of a THz probe pulse. The THz probe experiences a pump intensity dependent attenuation when transmitted through the resonator. The free carrier absorption loss is very easily monitored by observing the amount of dampening experienced by the spectral resonance of the filter.

A schematic of the static pump-probe regime is shown in figure 4.11. Here we depict a 515 nm 180 fs pump photoinjecting carriers near the surface of a silicon substrate with a patterned gold cross plasmonic array atop. A THz pulse arrives 100 ps after the pump and transmits through the notch filter device. The interaction of the pulse with the resonator is shown with a residual ringing tail upon transmission. The entire THz transient experiences a free-carrier absorption during transmission, dependent on the pump intensity. In which case, the plasmonic resonance of the filter can be shown to incur a loss of effectiveness.

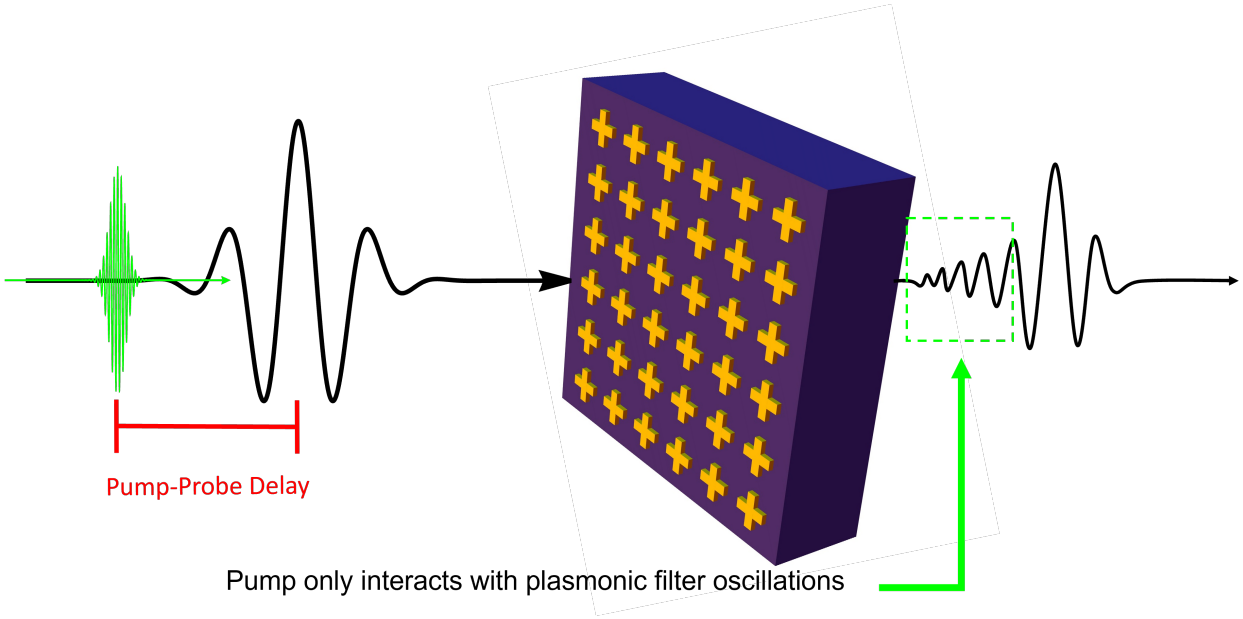

Figure 4.12: A schematic depicting an alternate dynamic pump-probe regime. In this case, the pump pulse arrives within picoseconds after the THz probe. The goal is to allow the off-resonant spectral components of the probe to pass through the device. The pump arrives during the residual plasmonic oscillations of the THz filter resonance and induces a dampening as a function of pump-probe delay.

It is also possible to take advantage of having an ultrafast pump and long substrate carrier recombination time by using a dynamic pump-probe spectroscopy, shown in figure 4.12. In this case, the pump pulse arrives after the THz probe but at a pump-probe delay time that falls within the range of the resonant oscillations of the filter. The goal here is to allow the off-resonant THz spectral components of the transient to pass through the device with minimal absorption loss. The pump intensity is kept constant while the pump-probe delay time is varied within the picosecond range of the filter oscillations. Since the carrier dynamics of silicon allow an ultrafast pump to effectively switch its response in terms of transmission, the pump can be used to bleach any remaining time-domain resonance oscillations upon arrival. Therefore, the spectral resonance of the filter will experience a dampening as a function of pump-probe delay time, dependent on how much of the residual oscillations the pump attenuates.

4.2.2 Static pump-probe tuning

Beginning with the static case, a pump-probe experiment is done on a 1.5 THz plasmonic resonator with the geometric configuration shown in figure 4.6 b) with an array periodicity of 56 µm, a cross arm length of 38 µm, and a cross width of 12 µm. THz transients are measured after passing through the filter, which been optically doped with carriers 100 ps prior to the arrival of the THz probe.

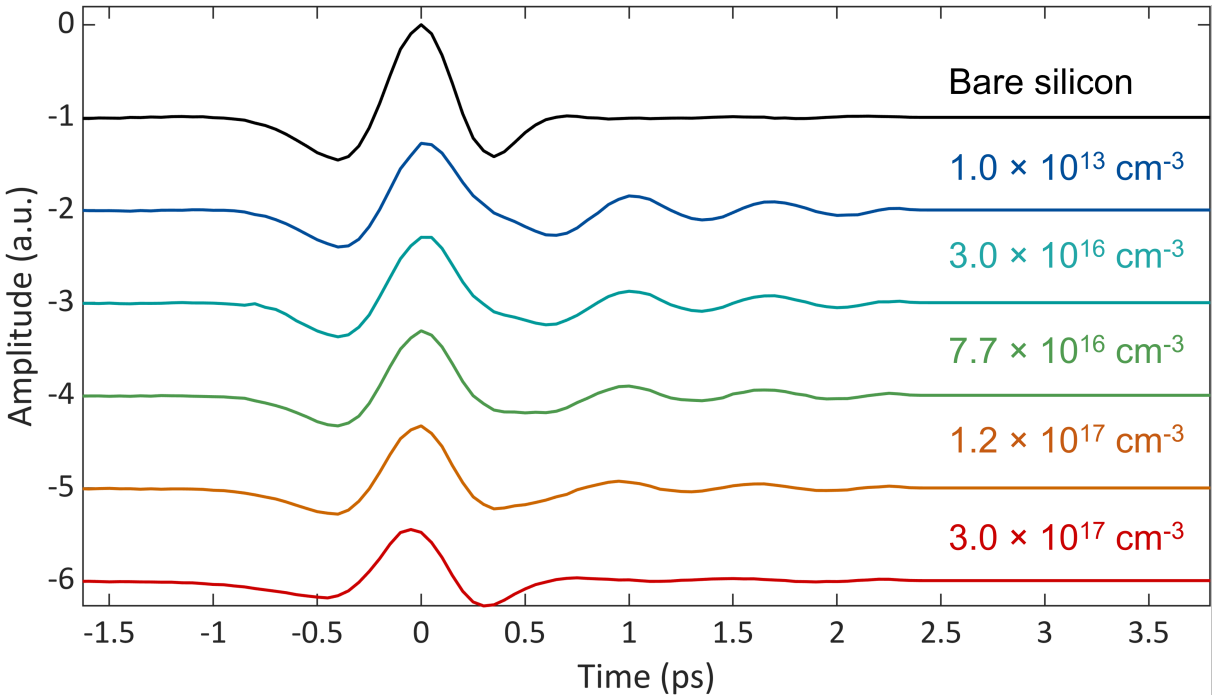

Figure 4.13: Time-domain plot of a static pump-probe tuning experiment on a silicon substrate metasurface resonator. The device is pumped with a 515 nm pump that will photoinduce an intensity dependent carrier density near the resonator array. 100 ps after the arrival of the pump, the device is probed with a THz-TDS scheme. THz transients passing through a variably doped resonator are plotted along with their color coordinated doping concentrations. A gradual bleaching of the residual plasmonic oscillations is observed, up until a complete saturation effect.

In figure 4.13, the transmitted THz probe pulses are plotted together along with their respective optical doping carrier densities. As discussed in the previous section, the carrier densities being shown are a subset of the measurements, carefully selected to show the gradual

attenuation of the filter resonance to a saturation. The presence of filter oscillations without the effect of the pump can be seen in the n=1×10^{13} cm^{-3} transient; the carrier density here represents the intrinsic carrier density of the silicon substrate. As the silicon is pumped, the carrier density present near the surface of the device interacts with the filter response and free carrier absorption causes an attenuation of the entire transient. Looking at the plotted transients in descending order, the residual plasmonic oscillations are shown to gradually decay and bleach away. Interestingly, while there is some amount of attenuation, the off-resonant component of the THz pulses do not experience much of a decay until the n=3×10^{17} cm^{-3} transient. It is only once the plasmonic oscillations have been fully bleached that a strong attenuation is experienced by the off-resonant component of the THz probe. This bleaching-to-saturation effect can also be presented in the spectral domain, upon Fourier transforming these transients.

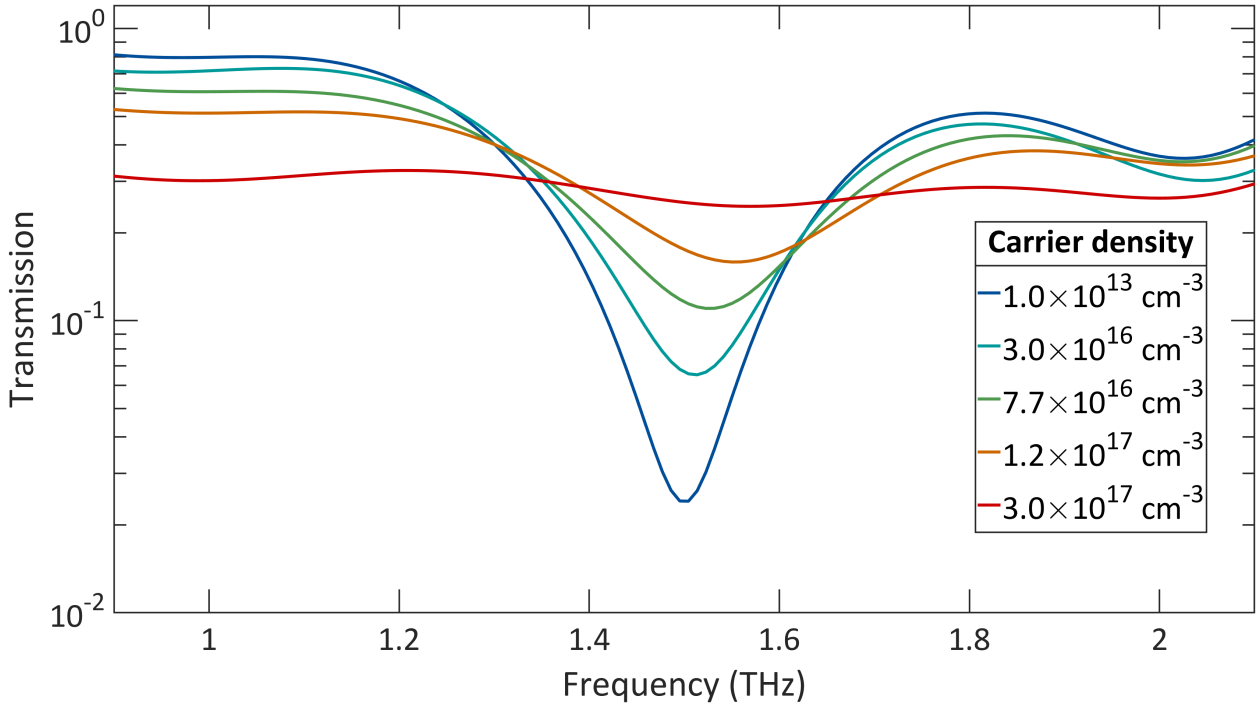

Figure 4.14: Silicon-referenced intensity transmissions of the static pump-probe tuning experiment. The plot is centered on the resonance feature but also visualizes the off-resonant spectral components. The resonance is shown to increase in transmission, blueshift in frequency, and broaden in linewidth as a function of increasing carrier density. After the resonance bleaches out, a saturation occurs and results in a flat attenuated transmission.

Figure 4.14 shows the plotted intensity transmissions of the measured transients. The plots are referenced to the bare silicon transient shown in figure 4.13. The plot is centered on the plasmonic resonance but also highlights how the off-resonant spectral components change with increased carrier density. The resonance is shown to broaden in linewidth, blueshift in frequency, and increase in transmission by an order of magnitude. The bleaching of the resonance is analogous to an increasingly damped harmonic oscillator, up until a complete saturation of the resonance (red curve) and a strong attenuation of the off-resonant spectral components.

Simulations and resonance analysis of static tuning

The experimentally observed resonance changes in the static tuned experiments require a more in-depth analysis and modelling that can be achieved using a series FDTD simulations. These simulations are reliable for a silicon substrate resonator because of the long carrier recombination time of silicon. Since we are simulating a THz source impinging on these devices, the presence of an optical pump must be modelled by changing the material properties of the silicon substrate in simulation to account for the induced free charge carriers. Given the previously discussed large absorption coefficient of 515 nm light in crystalline silicon, we can model the photoinduced carrier density as an exponentially decaying density multilayer stack of silicon within the first micron of the resonator array. Figure **??** shows the simulated electric field distributions of various static tuning simulations.

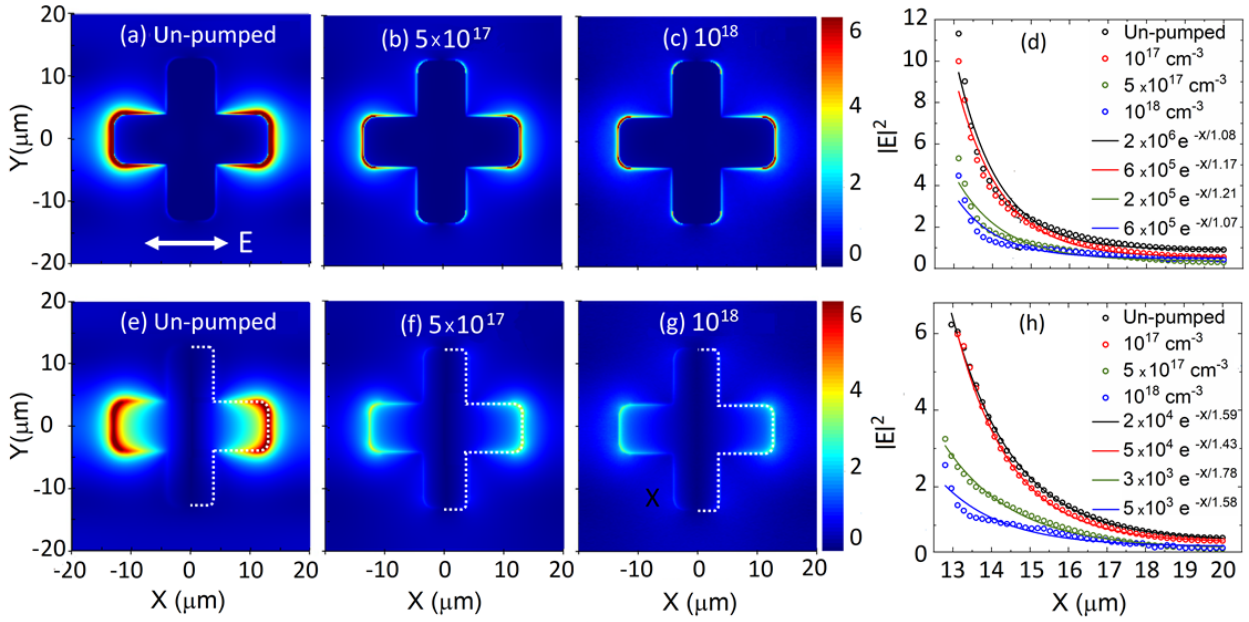

These simulations are done by placing a single gold cross structure on a silicon substrate and then computing a 3D simulation with periodic boundary conditions imposed in the XY plane. The multilayer stack is simulated with silicon slabs of exponentially increasing

thickness, and decreasing carrier density, beneath the cross. The gold material is defined using a 3D conductivity model [78] while the silicon is taken as a Drude material with a relative known permittivity [55] and a frequency dependent scattering time [57]. Figures **??** a), b), and c) show the spatial electric field distribution on a cross monitored 100 nm above the gold-silicon interface, at the center of the 200 nm thick cross. Figures **??** e), f), and g) show the field distribution on a cross monitored 500 nm below the gold-silicon interface, within the photoinduced carrier density region. The unpumped simulation represents a silicon substrate with an intrinsic carrier density of n=1×10^{13} cm^{-3}. In both cases, an increasingly attenuated dipole-like response is observed in the field distributions. Of course, this dipole like feature corresponds to the polarization of the incident THz source field in the simulation. As explained before, the use of a cross design is solely for the purpose of having symmetry in the THz response of the device in experiment. It is clear from the field distributions that any cross talk from the horizontal cross arm to the vertical cross arm is not significant. Below the gold-silicon interface, the field notably overlaps into the area of the cross. More importantly, Figures **??** d) and h) show the magnitude of the electric field in the area immediately outside of the cross arms. With all carrier densities, the field is shown to decay exponentially away from the cross arms. The field magnitudes at different carrier densities are fit with exponential curves; interestingly, while there is a decrease in the field enhancement factor at higher carrier densities, the exponential decay rate of the field does not change significantly. This provides evidence that the observed bleaching of the resonance feature is not the result of a complete delocalization of the field, but rather a carrier absorption effect on the THz response.

The resonance features of the plasmonic filters are fit to Lorentzian lineshapes to quantify the transmission at resonance, the observed blueshift in center frequency, and the broadening of linewidth. This assumption is reasonable when the photoinduced carrier densities have not fully bleached the filter response. Simulations are again useful to fill in the experimental

data, especially in the regions of saturation where uncertainty dominates. Experimental and simulated resonance transmissions are imported into MATLAB and the curve fitting toolbox is used to to fit resonances at different carrier densities with Lorentzians [79]. The notch transmission at resonance, center frequency, and linewidth are then extracted and plotted as functions of carrier density in figure 4.15.

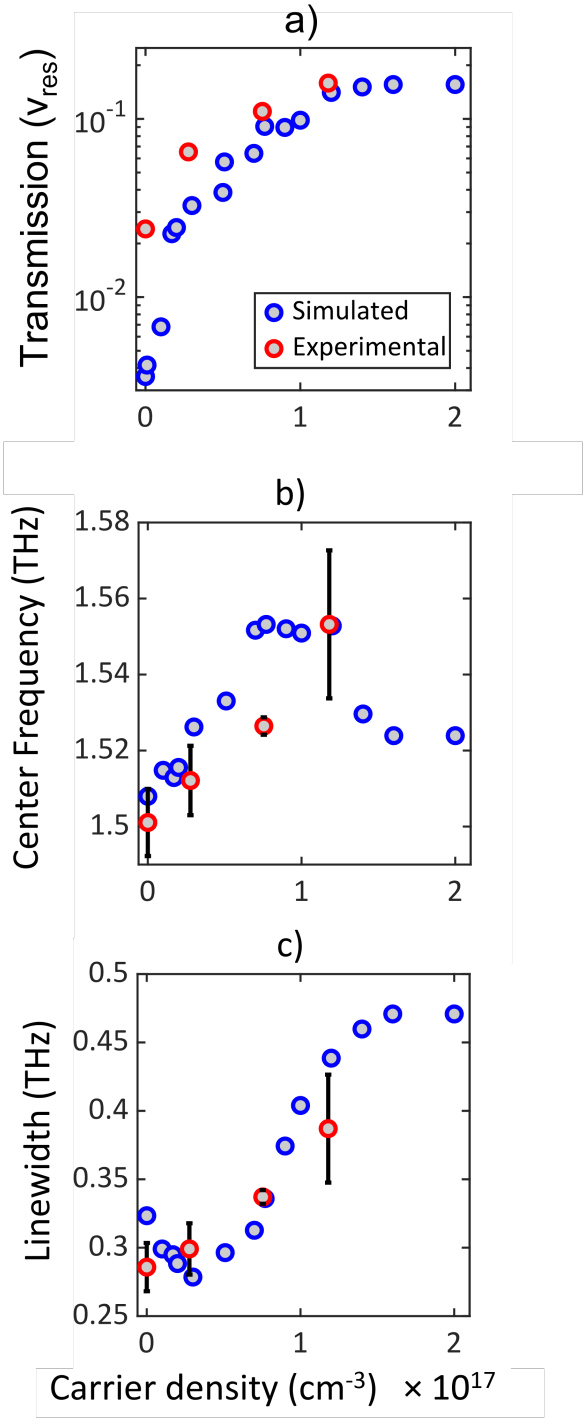

Figure 4.15: Lorentzian fit extractions of the notch filter transmissions at various carrier densities. a) A plot of notch resonance transmission as a function of experimental (red) and simulated (blue) carrier densities. b) A plot of resonance center frequency as a function of experimental (red) and simulated (blue) carrier densities. c) A plot of resonance linewidth as a function of experimental (red) and simulated (blue) carrier densities.

From the selected experimental data points (red), at a carrier density of n=1.2×10^{17} cm^{-3}, these plots show an order of magnitude increase in resonance transmission, a blueshift of 50 GHz in center frequency, and a linewidth broadening of 110 GHz. In figures 4.15 a)-c) it is clear from the simulations (blue) that there is a saturation effect that occurs with higher photoinduced carrier densities. This is attributed to the increased Drude absorption in silicon reducing the lifetime of the plasmonic resonance; the transmission spectra in a saturated regime are shown to have an increasingly flat response as the carrier density is increased. The blueshift of the center frequency is attributed to a change in the effective geometrical parameters of the resonator array [80]. Photoinduced carriers lower the real part of the refractive index of silicon in the region of the plasmonic array, causing the optical pathlength between the gold crosses of the array to decrease. The lattice pitch selected for a design target of a 1.5 THz resonance effectively becomes offset to a pitch more suitable for a short wavelength resonance, thereby, blueshifting the center frequency. Although soley varying the lattice pitch of a resonator does change the center frequency, the complete resonant response of an array resonator heavily depends on the geometry of the array elements. It is clear from 4.15 b) that the blueshift effect is not monotonically increasing and this is the result of the gold cross geometry remaining unchanged; large changes in lattice pitch require a reoptimization of the geometrical parameters of the crosses to match.

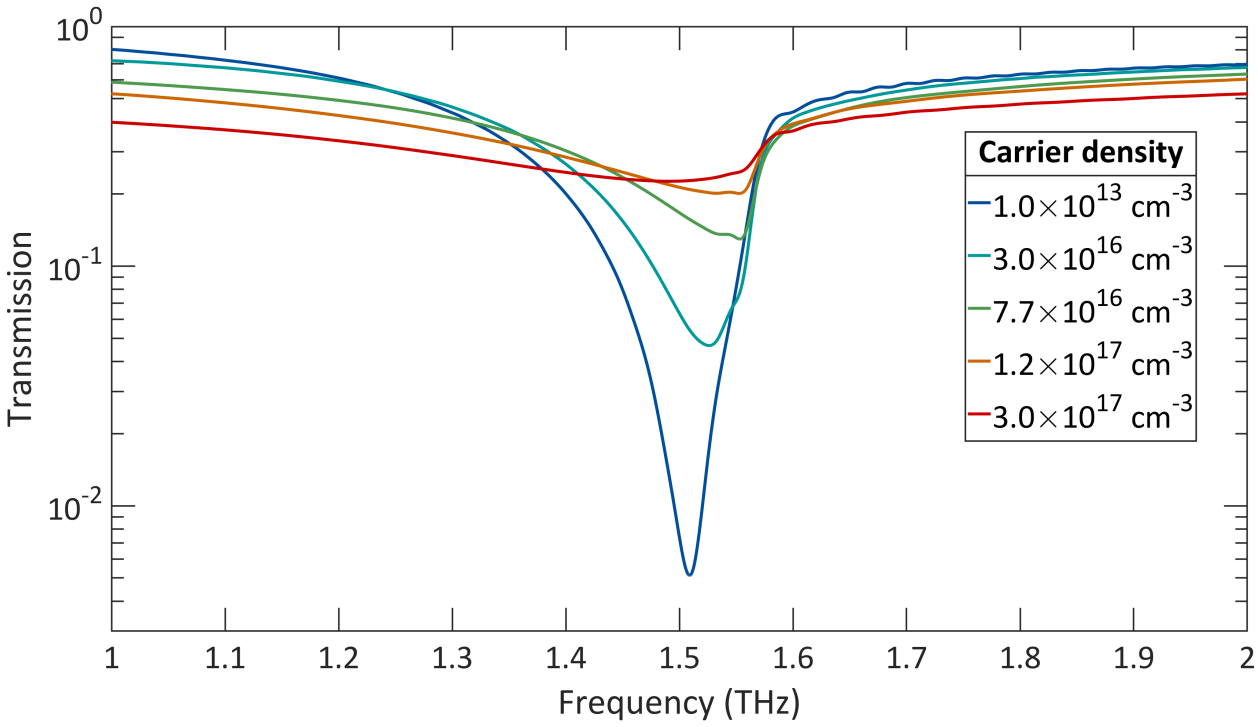

Figure 4.16: Simulated THz transmission of a gold cross resonator on silicon substrate. Plotted carrier densities are selected to match experimentally measured transmission spectra at pump intensities below the complete resonance bleaching threshold.

Finally, figure 4.16 is a transmission plot of the simulated photoinduced carrier densities that most closely matched with the experimental transmissions of the notch filter device pumped with various optical pump intensities shown in figure 4.14. The resonance transmission is again clearly shown to bleach and blueshift with increasing photoinduced carrier densities and is in very reasonable agreement with experimental observations.

4.2.3 Dynamic pump-probe tuning

While static pump-probe tuning is clearly an effective technique to control the frequency corresponding to the minimum in transmission and the quality factor of a plasmonic filter, there are still significant losses in the off-resonant transmission spectra. In figure 4.14, the saturated photoinduced carrier density results in a flat transmission of $T = 0.25$. This of

course is due to the THz probe transmitting through silicon with an optically induced carrier density before its arrival. We can instead take advantage of having an ultrafast pump and apply the scheme shown in figure 4.12 to interact a very intense pump soley with the time-domain oscillations corresponding to the notch filter resonance. We do this by configuring the pump strength to be fixed at the previously measured saturation threshold of the static pump-probe scheme, applying a photoinduced carrier density of n=3×10^{17} cm^{-3}. The pump is additionally configured to arrive after the THz probe arrives, to ensure the interaction with the residual plasmonic oscillations of the resonator. Figure 4.17 is a plot of time-domain measurements made using this dynamic pump-probe tuning scheme. The plasmonic array used for this demonstration is designed for a resonance frequency at 2.1 THz.

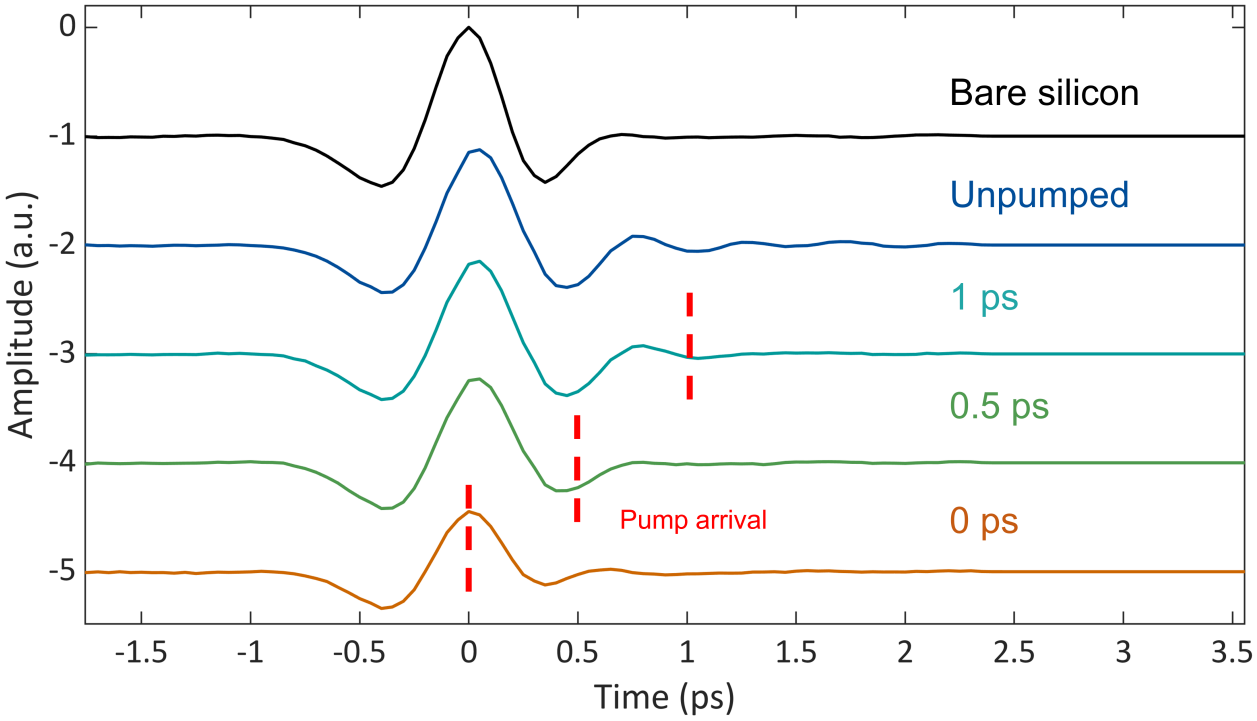

Figure 4.17: Dynamic pump-probe time-domain transients. A bare silicon THz transient is compared to THz transients passing through a notch filter designed for a 2.1 THz resonance component. A static intensity optical pump interacts with the residual plasmonic oscillations of the notch filter at a delay after the THz probe arrival. The pump intensity is selected as to completely bleach the resonance feature of the notch filter, determined by static pump-probe experiments on this filter design. The pump arrival time (red dashed lines) indicates the position of the transient after which the filter oscillations will be bleached away.

Here, a bare silicon THz transient (black) is first plotted along with an unpumped notch filter resonant response (blue). The target of the pump are the trailing oscillations of the filter transient. By adjusting the temporal delay between the static intensity pump and THz probe, the plasmonic oscillations can be shown experiencing a complete attenuation after the pump arrival time (red dashes). In terms of intensity transmission in THz, shown in figure 4.18, the benefits to the off-resonance spectral components are very significant. Unlike the static tuning experiment, achieving a complete bleach of the resonance is possible while maintaining an off-resonant transmission within 20% of the unpumped transmission.

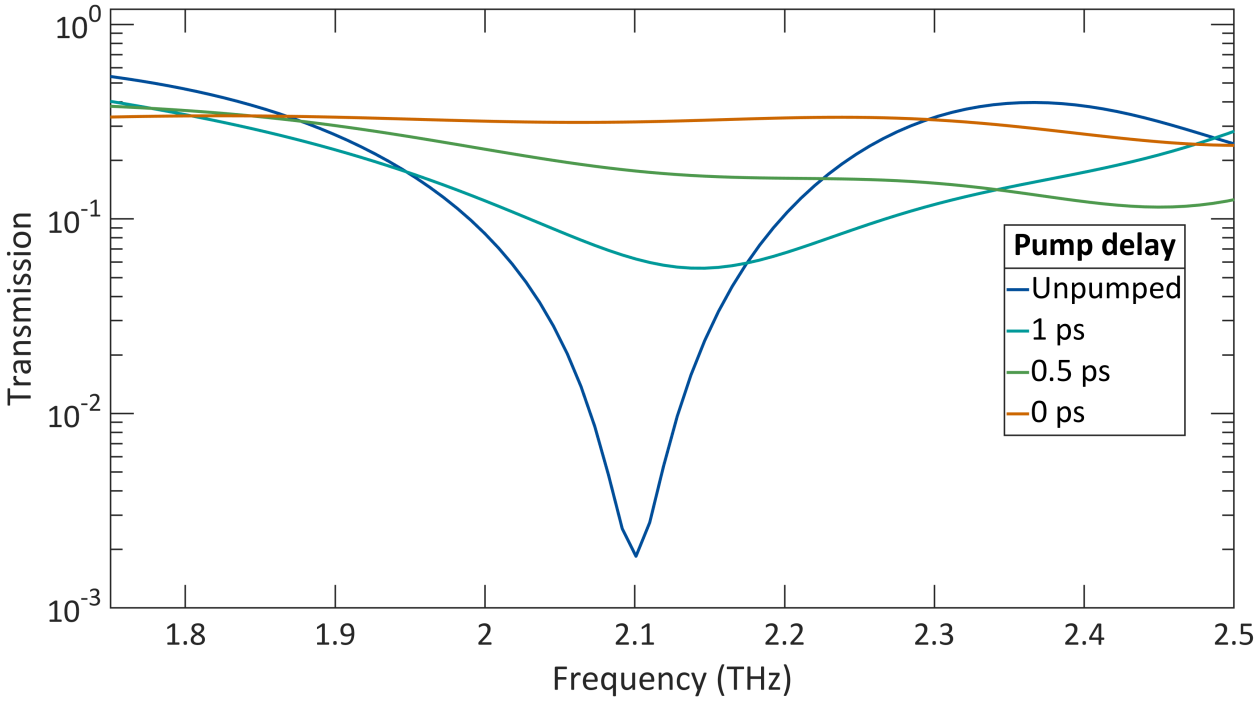

Figure 4.18: Dynamic pump-probe transmission spectra corresponding to Fourier transformed THz transients through a plasmonic resonator. Pump delay refers to the time of the optical pump arriving after the THz probe. Earlier delays correspond to more interaction with the resonance component of the notch filter. A few pump-delays are depicted to show the complete delay dependent saturation of the resonance.

A more in depth resonance analysis through Lorentzian fitting can again be applied, and is shown in figure 4.19. Plots of notch transmission, center frequency, and linewidth are plotted as functions of pump-probe delay. The previous two plots of THz transients and their Fourier transform utilize a subset of these data points. Looking at figure 4.17, provides a clear context that the pump arriving 3 ps after the probe effectively has no effect on the plasmonic resonance of the notch filter. The shortest pump-probe delay time plotted, 0.5 ps, corresponds to the pump effectively bleaching the entire resonant feature of the device. A resonance transmission change of more than an order of magnitude is observed over these delay times in figure 4.19 a). Figure 4.19 b) shows a total blueshift of 90 GHz in center frequency as the pump increasingly bleaches the duration of the filter oscillations. This

blueshift is again attributed to a carrier induced change in the real part of the refractive index, lowering the effective lattice array pitch. Finally, figure 4.19 c) shows a total linewidth change of 190 GHz over the measured pump-probe delays. The change in linewidth is again attributed to an increased Drude absorption from the greater concentration of carriers in the substrate. This is further exaggerated by the use of a saturating pump intensity for this experiment, to ensure the complete cutting of the plasmonic oscillations as a function of pump-probe delay.

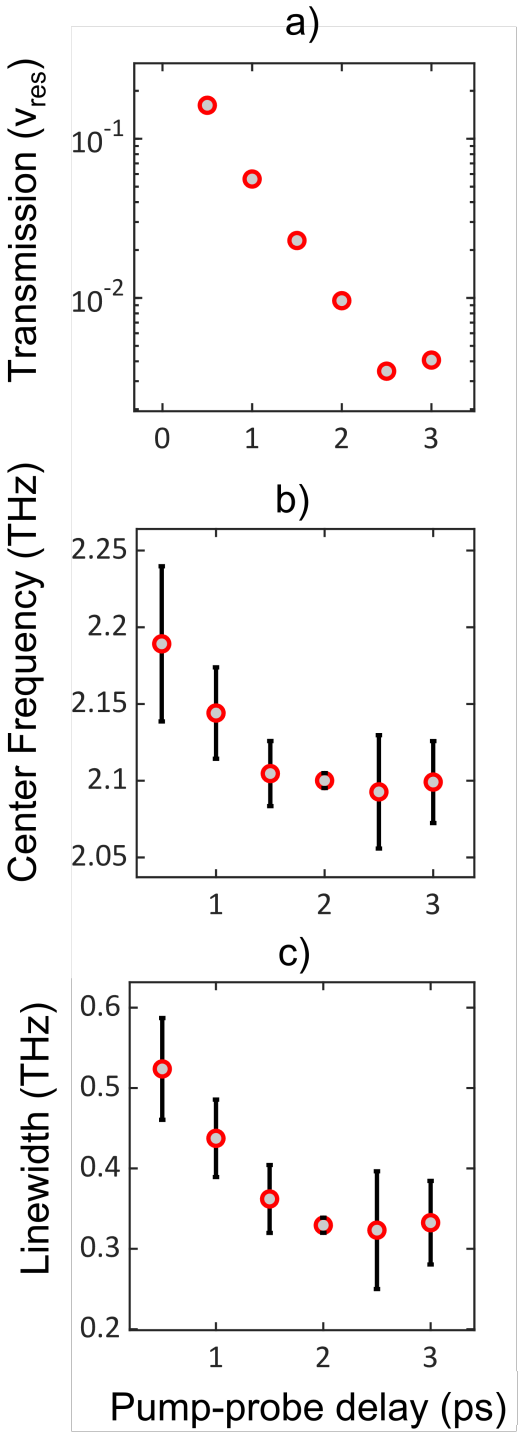

Figure 4.19: Lorentzian fit extractions of dynamic pump-probe resonance transmission as a function of pump-probe delay. a) Resonance transmission as a function of pump-probe delay. b) Resonance center frequency as a function of pump-probe delay. c) Resonance linewidth as a function of pump-probe delay.

4.2.4 Optically pumped graphene on plasmonic resonators

The first method of investigating optically tunable metasurfaces in the THz spectrum was through the use of a tunable substrate. While we have demonstrated that this is indeed possible and can be readily applied by designing a metasurface resonator to function atop a semiconductive substrate, the design has an intrinsic transmission inefficiency. An optically active semiconductor is tuned by photoexciting carriers and relying on Drude absorption to induce controllable decay in a plasmonic mode. The photoconductivity increase, required substrate thicknesses for significant optical absorption, and Fresnel reflection effects cause a large transmission loss in the THz. For these reasons, alternatives to tunable substrates are of great interest. One alternative is to deposit a two-dimensional (2D) nanomaterial like graphene on a plasmonic metasurface and investigate tunability by solely photoexciting carriers in the same plane as the metasurface. A schematic of the interaction is visualized in figure 4.20. Here, a femtosecond optical pump at 515 nm is depicted to interact with a layer of graphene in the plane of the plasmonic cross array. In this scheme, the pump is meant to arrive before or during the arrival of the THz probe pulse. Unlike the static pump-probe case discussed for a silicon substrate, the recombination time of graphene will be shown to be orders of magnitude faster than silicon. Therefore, the THz probe must arrive very soon after or during the arrival of the pump in order to probe the strongest photoinduced interaction with the metasurface.

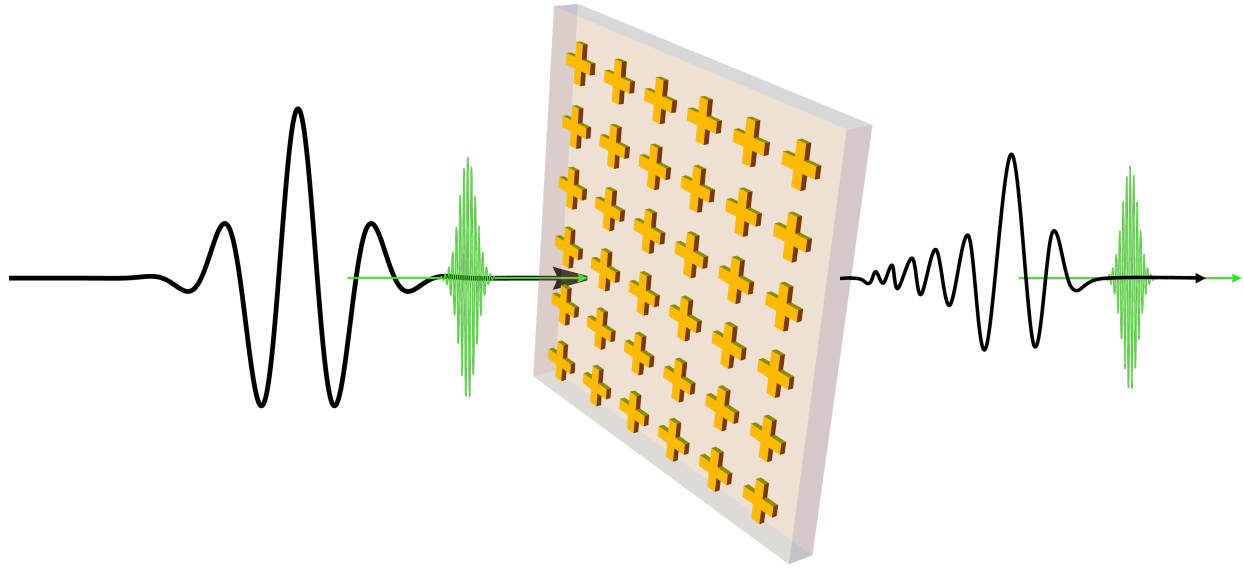

Figure 4.20: An alternative medium for optical tunability is proposed. A plasmonic metasurface is designed on a THz transparent substrate and CVD graphene is deposited in the plane of the metasurface. A pump-probe tuning scheme resembling a static pump is utilized, where the pump arrives onto graphene before or simultaneously with the THz probe.

Returning to the previously introduced cyclo-olefin polymer material, zeonor, here we make use of its THz transparent properties as substrate. Another design of cross-shaped metal structures in an array are deposited atop a 188 µm thick zeonor substrate. The design parameters of the plasmonic array are for a 1 THz Lorentzian-like resonance with a similar notch transmission and Q factor to the silicon substrate cross designs. The metallic crosses are fabricated using aluminium with an arm length of 110 µm, an arm width of 8 µm, an array periodicity of 130 µm, and a 200 nm thickness. Aluminium is chosen instead of gold for the purpose of availability and cost. In the THz, most metal conductivity's, particularly thin films, can be very accurately represented with a Drude model [81].

Figure 4.21 shows a simulated metasurface of this design. A field distribution of a single cross element is monitored in the XY plane at the aluminium-zeonor interface. Like the

crosses on silicon, we see a dipole-like response in the direction of the source input polarization. The field again appears confined on the edges of the cross arms, and additionally, there is no obvious cross talk between the vertical and horizontal cross arms.

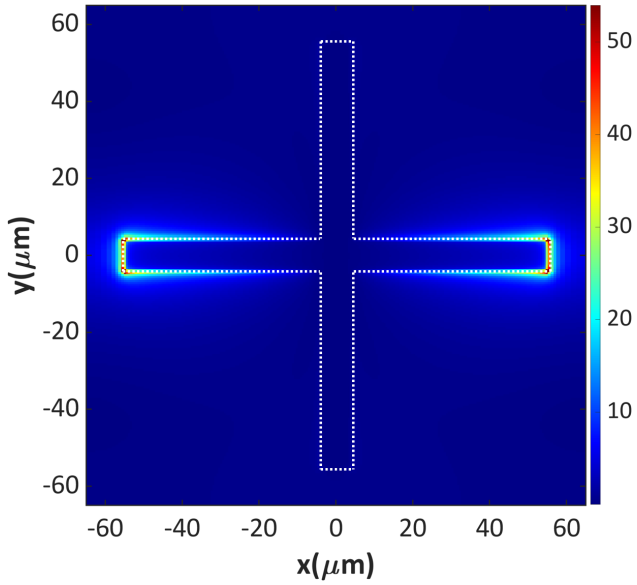

Figure 4.21: An FDTD spatial field simulation of a zeonor cross array metasurface. The field magnitude spatial distribution of a single cross element is depicted with a colour bar of electric field magnitude.

The corresponding power transmission monitored by the zeonor cross array simulation is depicted in figure 4.22. As mentioned, one of the constraints of the updated metasurface design is to maintain a similar Q factor to the silicon metasurface design, this is why cross elements were again utilized. Of course, having a larger Q factor and lower resonance transmission at the notch frequency allows any pump induced change in the plasmonic mode efficiency to be more significant when monitored. But, from chapter 3, in a THz time-domain experiment, the temporal duration of a THz scan is limited by the eventual appearance of back reflections from optics in the setup. A resonator with a large Q factor resonance in the frequency-domain, will appear to have a very long ringing oscillation in the time-domain, interfering with back reflections in the setup. Furthermore, the energy of the incident THz pulse to the resonator, will be distributed in a broad range, temporally, and require a very

large detection signal-to-noise ratio to be monitored. For these reasons, we limit the designed Q factor of resonators to <10 to enable a clear monitoring of photoinduced carriers near the metasurfaces.

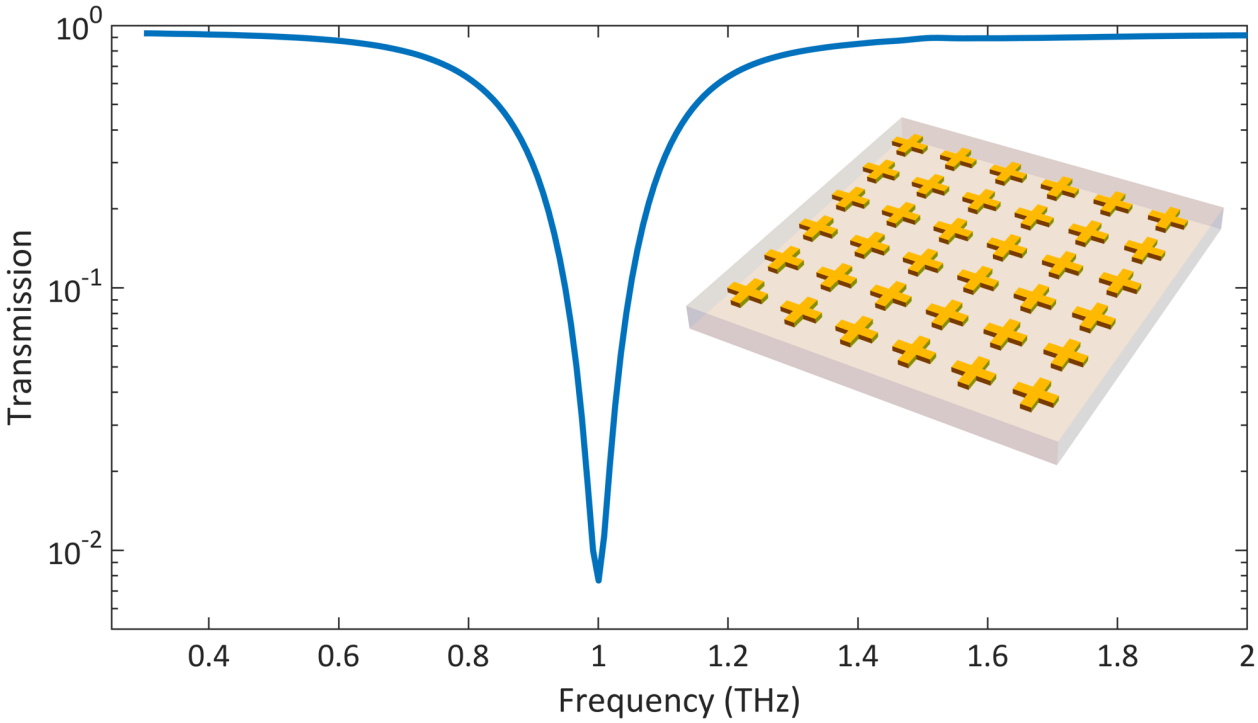

Figure 4.22: FDTD power transmission simulation of a 1 THz zeonor cross array metasurface. The metasurface parameters are given by a cross arm length of 110 µm, an arm width of 8 µm, an array periodicity of 130 µm, and a 200 nm metal thickness.

Optically-excited graphene probed with THz

To select a proper optical pump - THz probe delay range to attempt a tunability experiment of graphene on a metasurface, it is paramount to first characterize the carrier dynamics of graphene in THz. To do this, a layer of CVD graphene is transferred onto a bare 188 µm zeonor substrate. The particular fabrication method and resultant CVD graphene used in these experiments is standardized and has been previously characterized in the same THz-TDS setup [82]. These measured properties of CVD graphene are verified using an

FDTD simulation with the previously discussed Drude-like intraband 2D conductivity model [60]. A measured carrier density of n=1×10^{12} cm^{-2} and scattering time of 40 fs are used for verification. The experiment-simulation match is outlined further on, in the complete simulation of graphene on a cross array.

The important property of the CVD graphene utilized in these experiments is the large intrinsic carrier density. As mentioned in chapter 2, one of the goals of investigating graphene as a metasurface tunability alternative is to exploit the hot-carrier generation effect of negative THz photoconductivities [65]. Just as how the silicon carrier dynamics were measured, an optical pump can be temporally scanned through a graphene sample using a delay stage while the fixed peak THz field through the sample is measured as a function of pump-probe delay, shown in figure 4.23. For these measurements, a 4.7 GW/cm^2, 180 fs, 515 nm pump pulse is spatially overlapped with the THz probe and temporally scanned. A high intensity ultrafast pump is required to photoinduce sufficient carriers in graphene, being a single layer nanomaterial, and because the hot carrier multiplication effect scales linearly with pump fluence.

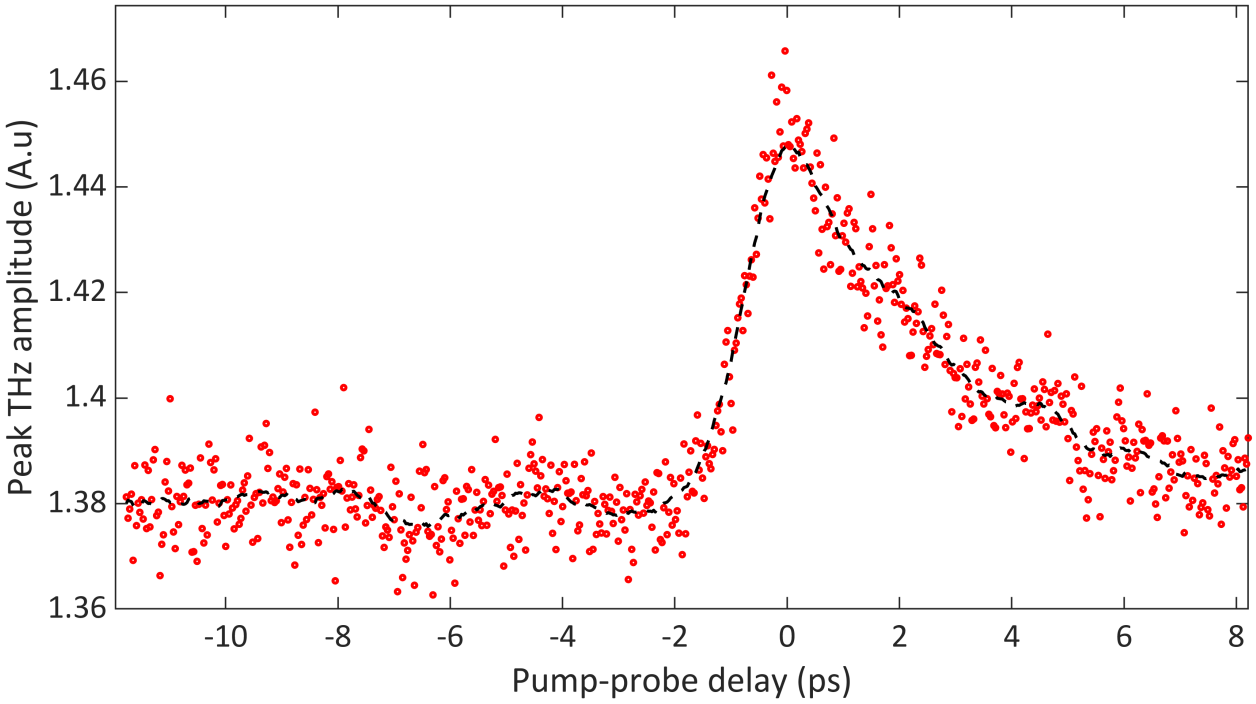

Figure 4.23: Peak THz amplitude in graphene as a function of pump-probe delay. A 515 nm pump pulse is spatially overlapped with a THz probe passing through a sample of graphene on Zeonor. The THz temporal position is then fixed while the pump pulse is temporally scanned. The black dashed curve is a moving average with a sliding window of 1 ps to visualize the trend of the data.

The delay stage controlling the temporal position of the pump is scanned with a step size of 30 fs over a total range of 20 ps, covering the pump-probe overlap. The measured peak THz amplitudes at every pump-probe delay are shown as red dots, while a moving mean with a sliding window of 1 ps is shown for clarity in black dashed lines. Negative pump-probe delays correspond to the pump arriving in graphene after the THz probe and positive pump-probe delays correspond to the probe arriving after the pump. It becomes very obvious from this plot that the intrinsic carrier density of graphene used in this experiment is sufficient to observe a hot carrier multiplication effect in graphene. A distinct increase in the peak THz amplitude occurs around the pump-probe overlap with a rise time that occurs within 1 ps and a slower, $>$ 5 ps decay towards the unpumped THz amplitude ensues thereafter. These

dynamics illustrate the fast establishment of a hot carrier distribution in the conduction band, followed by a slow electron-lattice cooling [64]. Therefore, the best region for studying pump-probe effects in graphene on a metasurface is at the pump-probe overlap.

We then inspect the effect of the optical pump on the full THz transient through the graphene sample, in figure 4.24. In this time-domain plot, a THz transient through air is shown alongside 4 THz transients through the sample of CVD graphene on zeonor. The transients through the sample are optically pumped with the aforementioned 515 nm pump pulse, where unpumped refers to the pump into the setup being blocked. The reduced pump intensities are obtained using ND filters and all transients are normalized to air. Since the pump induced change is very small, as one might expect from a single layer of graphene, an inset is included to magnify the region of the peak electric field values. Looking at the inset, it is clear that as the pump intensity is increased, the field strength of THz through the sample increases as well.

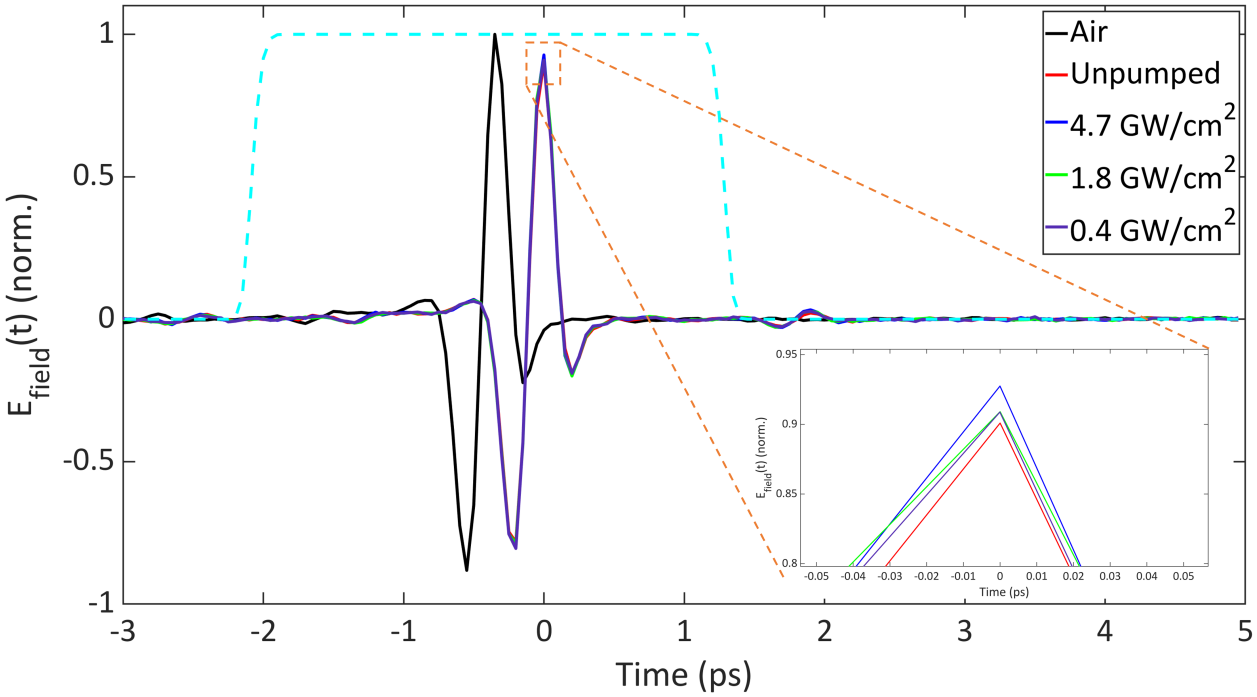

Figure 4.24: Plotted time-domain scans of optically pumped graphene on a zeonor substrate. An air reference scan is included with these measurements, of which all other transients are normalized to. Here, the graphene sample is externally pumped with a 515 nm ultrafast pulse that is overlapped with the peak of the THz probe. Three optical pump intensity scans are taken alongside an unpumped scan in which the pump is blocked. An inset is included for visual clarity of the pump induced change at the peak THz field.

The time-domain transients are then Fourier transformed and plotted in terms of intensity transmission with the air measurement taken as the reference. In figure 4.25, the transmissions of THz through the pumped and unpumped graphene sample are plotted. It remains clear that optically pumping graphene is increasing the measured THz transmission through the sample. But it is important to notice how the transmission through the graphene sample with a zeonor substrate does not increase consistently to a value of T>90%. At the start of this chapter, the transmission through a bare zeonor substrate was discussed and it was noted that zeonor is a very low loss substrate with the main mechanism of power transmission loss in THz being due to an 8% Fresnel reflection. The hot carrier multiplication effect in graphene is explicitly not an amplification effect. The transmission through

graphene is increased soley because the THz photoconductivity in graphene is reduced by the presence of the optical pump. At the fundamental limit of this effect, the THz probe can only transmit through a graphene layer without loss. In this case, the total transmission through a sample will be soley determined by the THz transmission through the substrate. The maximum optical pump intensity shown in these measurements is selected based on the damage threshold of zeonor. By empirically testing the 188 µm zeonor substrates in the presence of an optical pump, it was determined that laser damage in the sample at 515 nm occurs at intensities exceeding 5 GW/cm^2. While it would be of interest to investigate hot carrier multiplication in graphene with stronger pump intensities through the use of a stronger substrate, observing a noticeable pump induced change in these samples is sufficient to test the effect on a resonator sample.

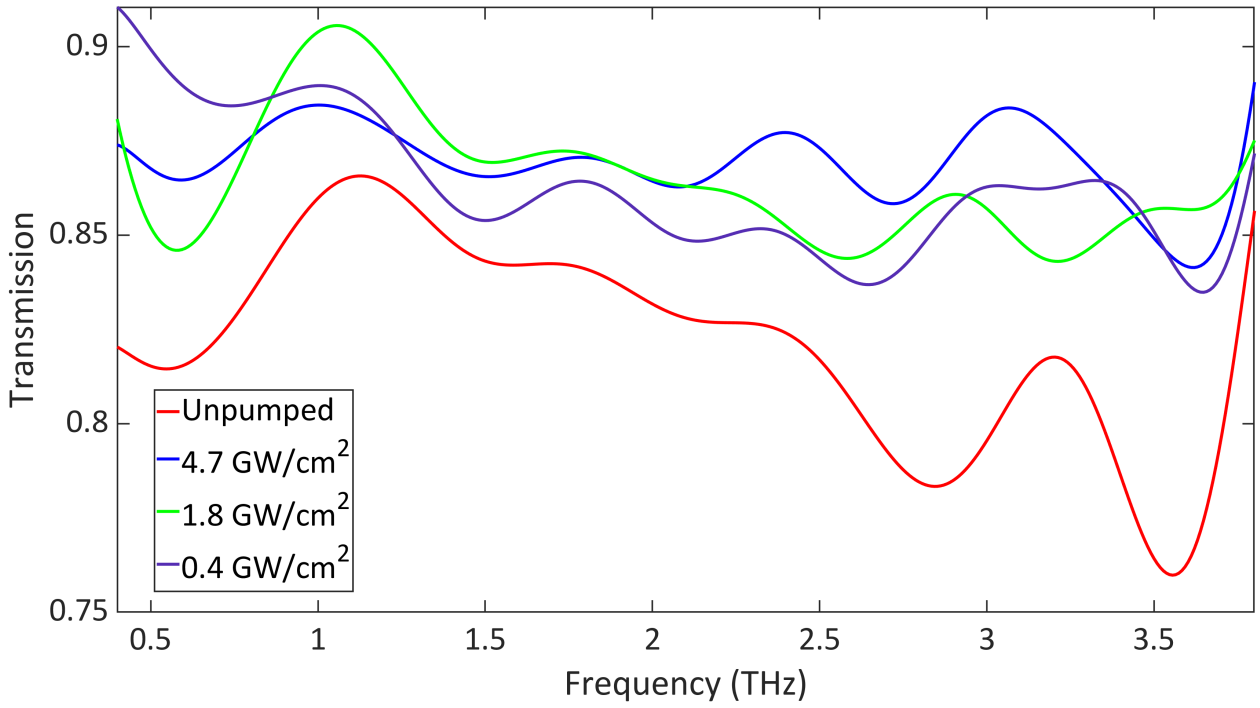

Figure 4.25: Intensity transmissions of optically pumped graphene on a zeonor substrate corresponding to the Fourier transformed time-domain scans referenced to air.

Optically-excited graphene on plasmonic resonators

With the quantification of how much an optical pump can increase THz transmission in graphene through the hot carrier multiplication effect, we can investigate the effect of pumped graphene on a metasurface. First we must understand how the presence of graphene on a metasurface resonator will change the resonance properties. From the start of this section, knowing that the CVD graphene used in these experiments has been previously characterized in terms of a carrier density and scattering time, we can then incorporate an FDTD simulation of graphene on a 1 THz resonator utilizing the aforementioned 2D conductivity Drude-like model. Figure 4.26 shows plots of experimental and simulated graphene on a 1 THz zeonor substrate metasurface.

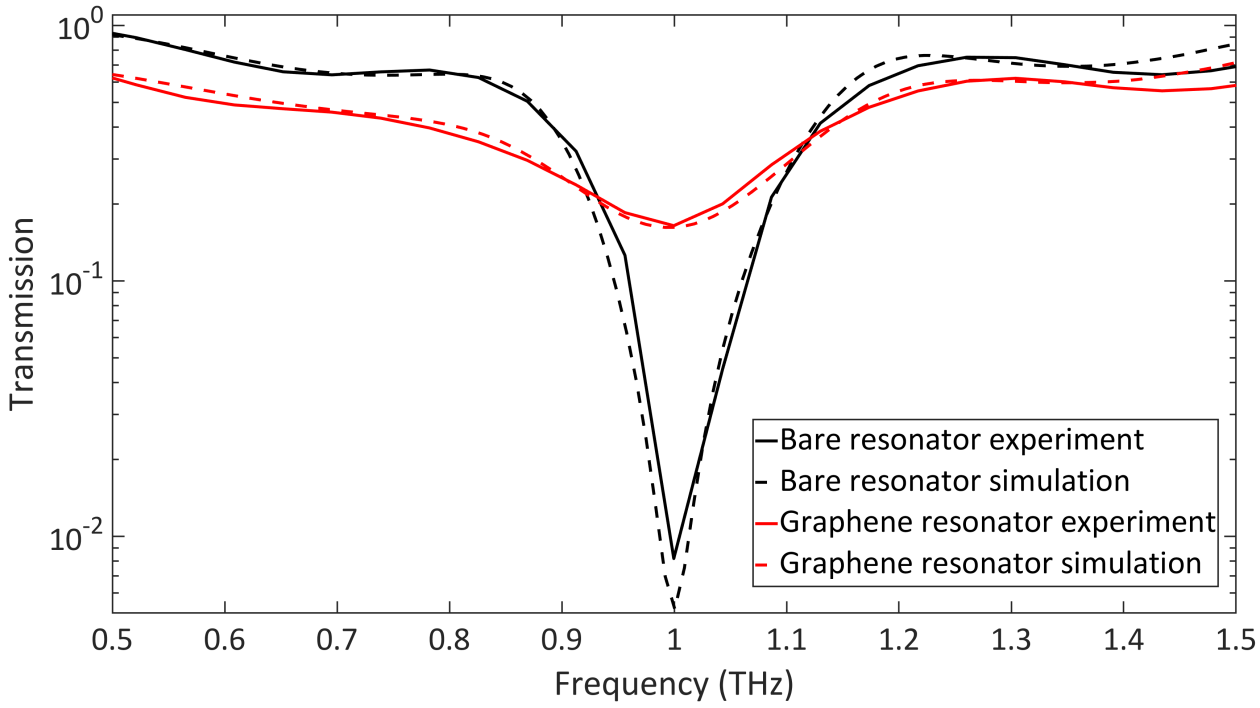

Figure 4.26: Simulated and experimental transmissions of graphene on a resonator. The FDTD simulations are plotted with dashed lines of the corresponding experimental transmissions.

Here, experimental measurements of the 1 THz resonator on zeonor (black) are compared

to measurements of the resonator with a layer of transferred CVD graphene (red). Dashed lines indicate the corresponding FDTD simulations of the bare resonator and the resonator with a graphene model interacting at the air-metasurface interface. In general the agreement between experiment and simulation is excellent. This indicates that the Drude parameters extracted from the previous experimental characterization of CVD graphene are applicable to a graphene-resonator structure. In the bare resonator results, we see a discrepancy between experiment and simulated transmission at the notch. The difference in transmission is 0.3% and likely due to a simulation assumption of no loss in the zeonor substrate, with the imaginary part of the refractive index set to zero at all frequencies. The reason the bare resonator sample transmission is shown along with the graphene-on-resonator transmission is to highlight the amount of loss caused by the presence of graphene. When graphene is present, the resonance transmission increases by over an order of magnitude at the notch, there is a linewidth broadening, and the off-resonant spectral components suffer a noticeable loss in transmission. Although, there is interestingly no shift in the resonance frequency, indicating that the presence of graphene in the plane of the metasurface is not inducing a change in the effective real part of the refractive index. The measured and simulated loss is the direct result of the intraband transitions in graphene, which dominate the optical conductivity of graphene in the THz region. Unlike shorter wavelengths where the absorption of graphene is soley determined by the fine structure constant and known to have a value of 2.3% [83]. The absorption of graphene in the THz region is dependent on the Fermi energy, which is proportional to its carrier density. Being that the CVD graphene used for this experiment is intrinsically doped, it is expected that significant absorption will occur in the sample. For the purpose of investigating optical tunability, a strong absorption in graphene, particularly at the resonance, is very useful. Even small pump induced changes in the layer of graphene will be detectable at the resonance transmission because the decrease of photoconductivity in graphene is expected to reduce the resonator loss.

The measurement of optical tunability for graphene on the 1 THz metasurface resonator will be done through a dynamic pump-probe scheme. Since we know from the carrier dynamics of graphene that the largest increase in THz amplitude occurs within 1 ps of the pump-probe overlap, it is not possible to monitor a resonator THz transient undergoing a uniform pump induced change. The time-domain response of the 1 THz resonator with graphene is shown in figure 4.27. Here, transients through a resonator are compared and normalized to an air reference. We can see how the transmission through the resonator results in residual oscillations that last at least 3 ps in duration. Therefore, the 1 ps main excitation observed in graphene cannot be experienced during the entire oscillations of the resonator. The dynamic approach to measuring tunability in the resonator will be done by allowing the pump to spatially overlap with the THz probe at different times during the resonance. The pump-probe delays are marked with dotted vertical lines in the plot with the corresponding times shown in the legend. Here, 0 ps refers to a temporal overlap between the optical pump and THz probe. Conceptually, since the 4.7 GW/cm^2 515 nm pump is expected to increase the THz amplitude, interacting the pump with different regions on the THz transient should exhibit a different emphasis in the transmission characteristics. Primarily, interacting the pump with the region of the resonance transient that does not have oscillations should increase the off-resonant transmission and interacting the pump with the residual oscillations should improve the resonance quality. Converting to intensity transmission, in figure 4.28, we can observe the temporal movement of the pump along the THz probe transient.

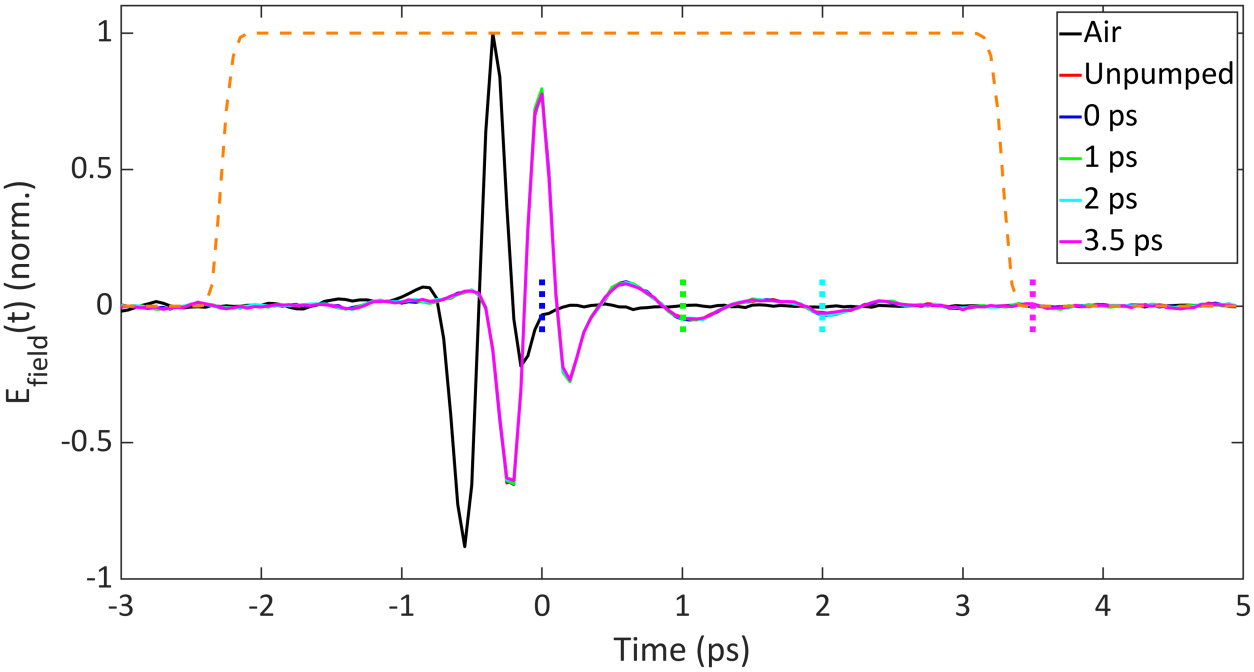

Figure 4.27: Time-domain plots of optically excited graphene on a plasmonic resonator. The various times correspond to the time of pump arrival relative to the THz temporal peak. Vertical dashed lines of the corresponding colours are plotted to further illustrate this. The windowing function is shown with yellow dashed lines.

In this plot, the resonant and off-resonant intensity transmissions of graphene on a metasurface resonator are shown in the presence of a temporally delayed optical pump. The transmissions are normalized to the air reference scan of the previous plot. While the pump induced change in graphene is indeed small ($\Delta T<5\%$), a clear trend does appear. When the graphene metasurface sample is first pumped with a pump-probe time delay of 0 ps (blue), the off-resonant transmission experiences the largest increase compared to the unpumped transmission. At the resonance, magnified in the figure inset, the 0 ps transmission decreases, which signifies that the quality of the resonator has improved. The improvement of the resonance quality occurs because the optical excitation in graphene lasts long enough to improve the THz amplitude of the first resonance oscillation in the time-domain, occurring within 1 ps after the optical pump arrives. When the pump arrives 1 ps after the THz probe peak (green), the pump is expected to greatly interact with the first resonance time-domain

oscillations and less-so with the off-resonant spectral components of the transient. We can see this from the reduction in the off-resonant transmission improvement but an increase in the quality of the resonance. Now, as the pump is arriving further after the THz probe at delay of 2 ps (cyan) and 3.5 ps (magenta), the off-resonant spectral components of the resonator response are no longer under excitation and only the final time-domain oscillations of the resonance are experiencing a pump induced improvement in THz amplitude. Since these final oscillations are already small in amplitude, the improvement in the quality of the resonance transmission diminishes and the response of the device returns to the unpumped state. In conclusion, the hot carrier multiplication effect in graphene, in combination with a notch filter metasurface, and an ultrafast optical pump, enables the use of a dynamic pump-probe tuning mechanism to tune the response of a metasurface through improving the resonance transmission quality. This optical tunability technique, accomplished through improvement rather than loss, is encouraging to further investigate for viability if the effect is scalable through the use of multiple layers of graphene.

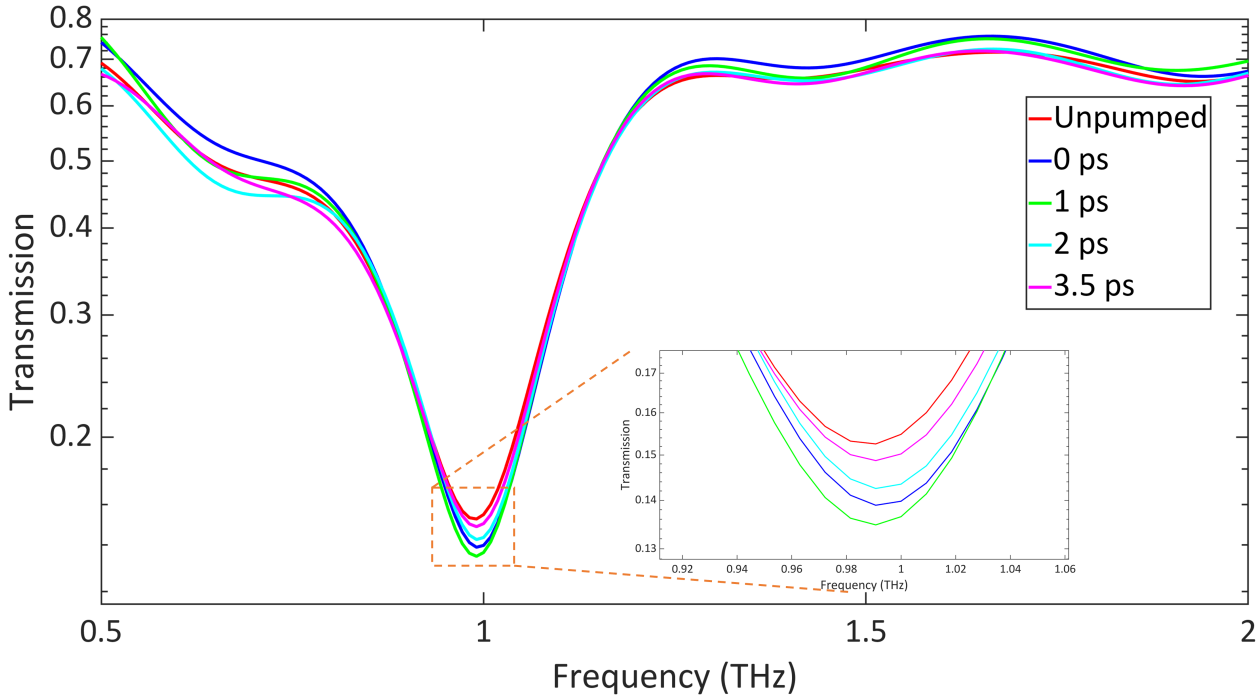

Figure 4.28: Corresponding transmission plots of optically excited graphene on a resonator. The resonant and off-resonant spectral components are shown to experience varying transmission improvement dependent on the temporal interaction of the pump with the residual plasmonic filter oscillations. An inset is shown to further visualize the transmission change at resonance.

Chapter 5

Conclusions

5.1 Summary

In this work, THz plasmonic metasurfaces are explored in the context of optical tunability in the substrate and in the plane of the metasurface. We first describe the working framework behind the concept and design of plasmonic resonators. We describe a procedure of creating a THz plasmonic array, or metasurface, to exploit localized surface plasmon resonances and the geometrical factors that determine its response. The materials used for optical tunability applications, silicon and graphene, are described in terms of Drude and Drude-Boltzmann optical conductivity models. We then review the technique of time-resolved THz spectroscopy, in which we discuss the generation, detection, and optimization techniques that enable us to monitor a single-cycle THz pulse in the time-domain. Following this, we detail the experimental setup utilized for the generation of THz, interaction with a sample, and the near-infrared probe scanning detection process. A tutorial of analyzing THz sample transients to optimize and extract frequency-domain information is given in the context of analyzing resonant features. We then present the detailed experimental characterization of bulk silicon THz transmission and its THz response to an optical pump and carrier dy-

namics. We additionally analyze the THz response of Zeonor, a transparent dielectric with excellent THz transmission and low loss. Silicon is then utilized as a substrate for a resonant metasurface array of cross-dipoles. We show two techniques of optically tuning this device: a static tuning method, in which the silicon substrate is optically excited well before the arrival of a THz probe, and a dynamic tuning method, in which the silicon substrate is optically pumped during the residual time-domain oscillations of the THz probe interacting with the metasurface. Both methods demonstrate the tunable control of a resonance and the ability to effectively bleach out the filter response with increased optical intensity and temporal interaction. The static tuning method is further investigated using FDTD simulations to provide a working explanation of the changing resonant properties of the device. Additionally, monolayer CVD graphene is investigated in an optical pump - THz probe regime. The reported negative THz photoconductivity of highly doped graphene is investigated in terms of the THz transmission response and carrier dynamics. Graphene is then deposited on a tailored Zeonor-substrate metasurface design and investigated using an experimental and simulation transmission comparison for verification. Finally, the optically pumped THz response of graphene in the plane of a metasurface is experimentally probed and shown to relatively improve the quality of a resonator.

5.2 Future work

Several avenues of future directions are underway or planned for this project. First, We are investigating the THz response of our graphene-coated metasurfaces under a UV pump. Unlike the work shown in this thesis, in which an ultrafast optical pump induces a large enough photon density for the hot carrier multiplication effect, we find that a 450 nm low power 25 mW continuous wave (CW) laser also seems to decrease the THz photoconductivity of graphene. Figure 5.1 shows the UV-enabled improvement of the resonator quality and

off-resonance transmission.

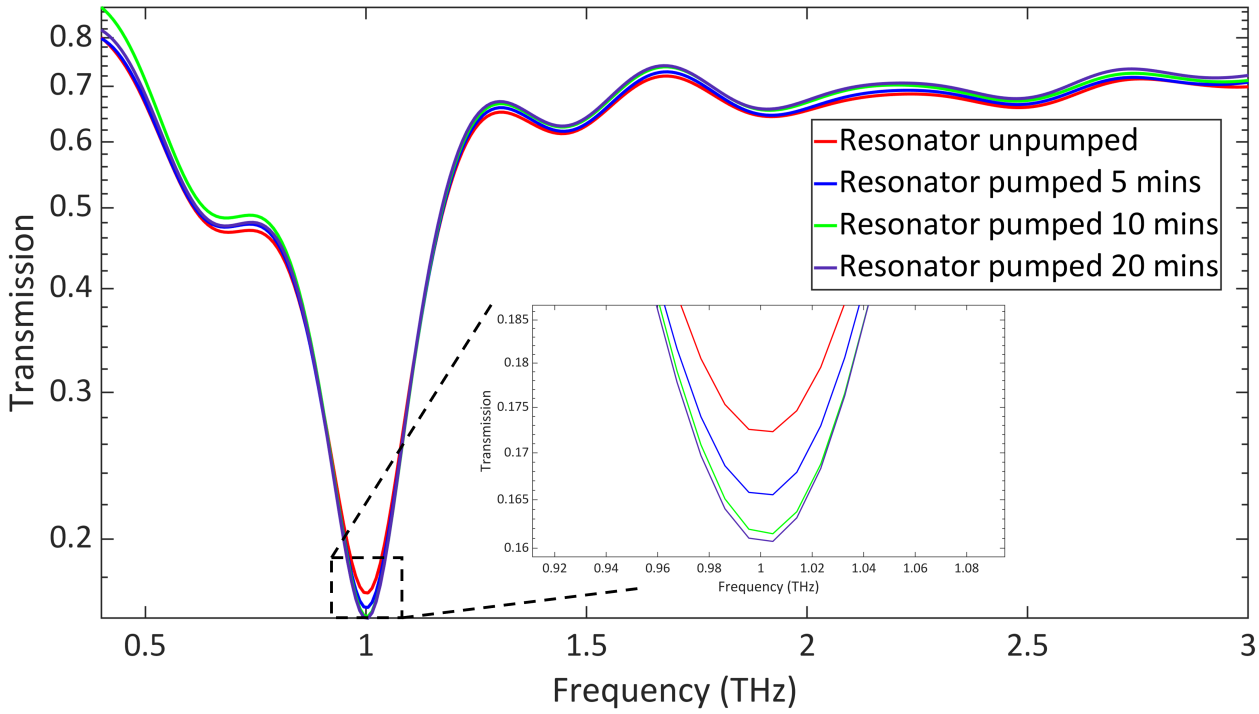

Figure 5.1: Intensity transmission around resonance of a 1 THz metasurface illuminated with a 25 mW, 450 nm CW laser. As the THz response of the metasurface is probed over a 20 minute duration, the resonance quality and off-resonant spectral components of the metasurface improves. A saturation in this improvement seemingly occurs within 10 minutes. An inset zooms on the UV-induced resonance improvement.

Here, the UV CW laser is left incident on the graphene metasurface sample for a period of 20 minutes during which the sample is periodically probed by THz pulses. The transmission quality of the sample gradually improves over a duration up until a saturation that begins after 10 minutes of illumination. The inset shows how the resonance quality improves in a similar fashion and magnitude to the hot carrier multiplication effect. Further investigation on the nature of this improvement must be undertaken.

Throughout this work, it is clearly evident that the pump induced THz response of CVD graphene is very small in magnitude, below a 5% change in intensity transmission. We have seen a similar experimental transmission response in CVD molybdenum disulfide.

While monolayer nanomaterials are excellent for plasmonic tunability because they can be transferred in the plane of a metasurface, the small pump-induced change is a drawback for realistic applications. We have been investigating spray coated liquid-phase exfoliated (LPE) graphene on a plasmonic metasurface. Instead of an atom-thick layer, LPE graphene is composed of stacked flakes of monolayer, bilayer, and few-layer graphene [84, 85, 86]. LPE graphene has the potential of having a stronger optical absorption due to the increased concentration of graphene while maintaining the strong interaction in the plane of the metasurface, due to still having a nanoscale thickness. One challenge of using LPE graphene and other nanomaterials in the THz region is to characterize the THz conductivity within a single flake and determine the corresponding electron mobility.

Finally, we are looking into the application of THz plasmonic resonators in the field of cavity quantum electrodynamics. Typically, optical cavities are put in the presence of atomic or molecular systems to investigate strong coupling regimes in which hybrid-light matter states can be formed [87, 88, 89]. In our future research direction, plasmonic THz resonators will be used to confine light, analogously to mirror cavities, and interacted with molecular systems. The goal of this work will be to investigate the potential for strong-coupling between molecular vibrational and THz plasmonic modes and the generation of hybrid-light matter states.

Bibliography

[1] L. Gingras, A. Jaber, A. Maleki, O. Reshef, K. Dolgaleva, R. W. Boyd, and J.-M. Ménard, Opt. Express **28**, 20296 (2020).

[2] H. Guerboukha, K. Nallappan, and M. Skorobogatiy, Adv. Opt. Photon. **10**, 843 (2018).

[3] M. Tonouchi, Nature Photonics **1**, 97 (2007).

[4] C. Sirtori, Nature **417**, 132 (2002).

[5] S. S. Dhillon, M. S. Vitiello, E. H. Linfield, A. G. Davies, M. C. Hoffmann, J. Booske, C. Paoloni, M. Gensch, P. Weightman, G. P. Williams, et al., Journal of Physics D: Applied Physics **50**, 043001 (2017).

[6] Nature Photonics **7**, 665 (2013).

[7] N. Horiuchi, Nature Photonics **7**, 670 (2013).

[8] P. Smith, D. Auston, and M. Nuss, IEEE Journal of Quantum Electronics **24**, 255 (1988).

[9] M. Hangyo, M. Tani, and T. Nagashima, International Journal of Infrared and Millimeter Waves **26**, 1661 (2005).

[10] J. B. Baxter and G. W. Guglietta, Analytical Chemistry **83**, 4342 (2011).

[11] B. Fischer, M. Hoffmann, H. Helm, G. Modjesch, and P. U. Jepsen, Semiconductor Science and Technology **20**, S246 (2005).

[12] L. Yang, T. Guo, X. Zhang, S. Cao, and X. Ding, Reviews in Analytical Chemistry **37**, 20170021 (2018).

[13] H. Cheon, H.-j. Yang, S.-H. Lee, Y. A. Kim, and J.-H. Son, Scientific Reports **6**, 37103 (2016).

[14] T. Bowman, T. Chavez, K. Khan, J. Wu, A. Chakraborty, N. Rajaram, K. Bailey, and M. O. El-Shenawee, Journal of Biomedical Optics **23**, 1 (2018).

[15] T. Kleine-Ostmann and T. Nagatsuma, Journal of Infrared, Millimeter, and Terahertz Waves **32**, 143 (2011).

[16] M. Jacob, S. Priebe, T. Kurner, C. Jastrow, T. Kleine-Ostmann, and T. Schrader, in *2009 IEEE Globecom Workshops* (2009), pp. 1–6.

[17] B. Aqlan, M. Himdi, H. Vettikalladi, and L. Le-Coq, Scientific Reports **11**, 7703 (2021).

[18] K. Kawase, Y. Ogawa, Y. Watanabe, and H. Inoue, Opt. Express **11**, 2549 (2003).

[19] D. Suzuki, S. Oda, and Y. Kawano, Nature Photonics **10**, 809 (2016).

[20] H.-T. Chen, A. J. Taylor, and N. Yu, Reports on Progress in Physics **79**, 076401 (2016).

[21] R. A. Shelby, D. R. Smith, and S. Schultz, Science **292**, 77 (2001).

[22] V. M. Shalaev, Nature Photonics **1**, 41 (2007).

[23] J. B. Pendry, Phys. Rev. Lett. **85**, 3966 (2000).

[24] N. Yu and F. Capasso, Nature Materials **13**, 139 (2014).

[25] M. Khorasaninejad and F. Capasso, Science **358**, eaam8100 (2017).

[26] I. V. Shadrivov, A. B. Kozyrev, D. W. van der Weide, and Y. S. Kivshar, Applied Physics Letters **93**, 161903 (2008).

[27] A. Rose, D. Huang, and D. R. Smith, Phys. Rev. Lett. **107**, 063902 (2011).

[28] W. Cai, U. K. Chettiar, A. V. Kildishev, and V. M. Shalaev, Nature Photonics **1**, 224 (2007).

[29] D. W. Porterfield, J. L. Hesler, R. Densing, E. R. Mueller, T. W. Crowe, and R. M. Weikle, Appl. Opt. **33**, 6046 (1994).

[30] A. M. Melo, M. A. Kornberg, P. Kaufmann, M. H. Piazzetta, E. C. Bortolucci, M. B. Zakia, O. H. Bauer, A. Poglitsch, and A. M. P. A. da Silva, Appl. Opt. **47**, 6064 (2008).

[31] V. Torres, N. Sánchez, D. Etayo, R. Ortuño, M. Navarro-Cía, A. Martínez, and M. Beruete, IEEE Photonics Technology Letters **26**, 1679 (2014).

[32] N. I. Landy, S. Sajuyigbe, J. J. Mock, D. R. Smith, and W. J. Padilla, Phys. Rev. Lett. **100**, 207402 (2008).

[33] H.-T. Chen, W. J. Padilla, M. J. Cich, A. K. Azad, R. D. Averitt, and A. J. Taylor, Nature Photonics **3**, 148 (2009).

[34] W. J. Padilla, A. J. Taylor, C. Highstrete, M. Lee, and R. D. Averitt, Phys. Rev. Lett. **96**, 107401 (2006).

[35] H.-T. Chen, W. J. Padilla, J. M. O. Zide, A. C. Gossard, A. J. Taylor, and R. D. Averitt, Nature **444**, 597 (2006).

[36] M. Rycenga, C. M. Cobley, J. Zeng, W. Li, C. H. Moran, Q. Zhang, D. Qin, and Y. Xia, Chemical Reviews **111**, 3669 (2011).

[37] R. Yan, D. Gargas, and P. Yang, Nature Photonics **3**, 569 (2009).

[38] W. L. Barnes, A. Dereux, and T. W. Ebbesen, Nature **424**, 824 (2003).

[39] H. Yu, Y. Peng, Y. Yang, and Z.-Y. Li, npj Computational Materials **5**, 45 (2019).

[40] P. Mulvaney, Langmuir **12**, 788 (1996).

[41] J. Lloyd-Hughes and T.-I. Jeon, Journal of Infrared, Millimeter, and Terahertz Waves **33**, 871 (2012).

[42] X. Zhang, Q. Xu, L. Xia, Y. Li, J. Gu, Z. Tian, C. Ouyang, J. Han, and W. Zhang, Advanced Photonics **2**, 1 (2020).

[43] T.-I. Jeon and D. Grischkowsky, Applied Physics Letters **88**, 061113 (2006).

[44] N. Meinzer, W. L. Barnes, and I. R. Hooper, Nature Photonics **8**, 889 (2014).

[45] T. W. Ebbesen, H. J. Lezec, H. F. Ghaemi, T. Thio, and P. A. Wolff, Nature **391**, 667 (1998).

[46] R. Ulrich, Infrared Physics **7**, 37 (1967), ISSN 0020-0891.

[47] K. D. Möller, O. Sternberg, H. Grebel, and P. Lalanne, Journal of Applied Physics **91**, 9461 (2002).

[48] M. Nakhla and J. Vlach, IEEE Transactions on Circuits and Systems **23**, 85 (1976).

[49] F. D. E. Simulator, *Finite difference time domain (fdtd) solver introduction.*

[50] K. Yee, IEEE Transactions on Antennas and Propagation **14**, 302 (1966).

[51] S. Nashima, O. Morikawa, K. Takata, and M. Hangyo, Applied Physics Letters **79**, 3923 (2001).

[52] J. Dai, J. Zhang, W. Zhang, and D. Grischkowsky, J. Opt. Soc. Am. B **21**, 1379 (2004).

[53] B. Pejcinovic, in *2014 37th International Convention on Information and Communication Technology, Electronics and Microelectronics (MIPRO)* (2014), pp. 22–26.

[54] D. Grischkowsky, S. Keiding, M. van Exter, and C. Fattinger, J. Opt. Soc. Am. B **7**, 2006 (1990).

[55] E. D. Palik, *Handbook of Optical Constants of Solids* (Academic Press, Upper Saddle River, NJ, 1997).

[56] M. D. N. Ashcroft, Neil, *Solid State Physics* (Brooks Cole, 1976).

[57] F. Meng, M. D. Thomson, B. E. Sernelius, M. Jörger, and H. G. Roskos, Phys. Rev. B **91**, 075201 (2015).

[58] A. K. Geim and K. S. Novoselov, Nature Materials **6**, 183 (2007).

[59] L. A. Falkovsky, Journal of Physics: Conference Series **129**, 012004 (2008).

[60] G. W. Hanson, Journal of Applied Physics **103**, 064302 (2008).

[61] B. Sensale-Rodriguez, R. Yan, M. M. Kelly, T. Fang, K. Tahy, W. S. Hwang, D. Jena, L. Liu, and H. G. Xing, Nature Communications **3**, 780 (2012).

[62] J. H. Strait, H. Wang, S. Shivaraman, V. Shields, M. Spencer, and F. Rana, Nano Letters **11**, 4902 (2011).

[63] P. A. George, J. Strait, J. Dawlaty, S. Shivaraman, M. Chandrashekhar, F. Rana, and M. G. Spencer, Nano Letters **8**, 4248 (2008).

[64] K. J. Tielrooij, J. C. W. Song, S. A. Jensen, A. Centeno, A. Pesquera, A. Zurutuza Elorza, M. Bonn, L. S. Levitov, and F. H. L. Koppens, Nature Physics **9**, 248 (2013).

[65] M. T. Mihnev, F. Kadi, C. J. Divin, T. Winzer, S. Lee, C.-H. Liu, Z. Zhong, C. Berger, W. A. de Heer, E. Malic, et al., Nature Communications **7**, 11617 (2016).

[66] S. S. Dhillon, M. S. Vitiello, E. H. Linfield, A. G. Davies, M. C. Hoffmann, J. Booske, C. Paoloni, M. Gensch, P. Weightman, G. P. Williams, et al., Journal of Physics D: Applied Physics **50**, 043001 (2017).

[67] R. A. Lewis, Journal of Physics D: Applied Physics **52**, 433001 (2019).

[68] R. W. Boyd, *Nonlinear Optics 3rd Ed.* (Academic Press, 2008).

[69] Y.-S. Lee, *Principles of Terahertz Science and Technology* (Springer US, 1979).

[70] A. I.F., B. M.S., and B. V., *The lorentz oscillator and its applications* (2011).

[71] K. Sakai, *Terahertz Optoelectronics* (Springer-Verlag Berlin Heidelberg, 2005).

[72] A. Nahata, A. S. Weling, and T. F. Heinz, Applied Physics Letters **69**, 2321 (1996).

[73] C. Song, W.-H. Fan, L. Ding, X. Chen, Z.-Y. Chen, and K. Wang, Scientific Reports **8**, 8964 (2018).

[74] Tydex, *Tydex thz materials*, URL `http://www.tydexoptics.com/products/thz_optics/thz_materials/`.

[75] C. Schinke, P. Christian Peest, J. Schmidt, R. Brendel, K. Bothe, M. R. Vogt, I. Kröger, S. Winter, A. Schirmacher, S. Lim, et al., AIP Advances **5**, 067168 (2015).

[76] Tydex, *Tydex silicon*, URL `http://http://www.tydexoptics.com/materials1/for_transmission_optics/silicon/`.

[77] MathWorks, *Documentation: movmean*, URL `https://www.mathworks.com/help/matlab/ref/movmean.html`.

[78] M. A. Ordal, R. J. Bell, R. W. Alexander, L. L. Long, and M. R. Querry, Appl. Opt. **26**, 744 (1987).

[79] MathWorks, *Curve fitting toolbox documentation*, URL `https://www.mathworks.com/help/curvefit/index.html?s_tid=CRUX_lftnav`.

[80] H. Fischer and O. J. F. Martin, Opt. Express **16**, 9144 (2008).

[81] N. Laman and D. Grischkowsky, Applied Physics Letters **93**, 051105 (2008).

[82] S. Scarfe, Master's thesis, University of Ottawa (2020).

[83] R. R. Nair, P. Blake, A. N. Grigorenko, K. S. Novoselov, T. J. Booth, T. Stauber, N. M. R. Peres, and A. K. Geim, SCIENCE **320**, 1308 (2008).

[84] V. Nicolosi, M. Chhowalla, M. G. Kanatzidis, M. S. Strano, and J. N. Coleman, Science **340**, 1226419 (2013).

[85] J. Shen, Y. He, J. Wu, C. Gao, K. Keyshar, X. Zhang, Y. Yang, M. Ye, R. Vajtai, J. Lou, et al., Nano Letters **15**, 5449 (2015).

[86] Z. Li, R. J. Young, C. Backes, W. Zhao, X. Zhang, A. A. Zhukov, E. Tillotson, A. P. Conlan, F. Ding, S. J. Haigh, et al., ACS Nano **14**, 10976 (2020).

[87] S. Haroche and D. Kleppner, Physics Today **42**, 24 (1989).

[88] T. W. Ebbesen, Accounts of Chemical Research **49**, 2403 (2016).

[89] M. Hertzog, M. Wang, J. Mony, and K. Börjesson, Chem. Soc. Rev. **48**, 937 (2019).